NTNU

Norwegian University of
Science and Technology

Rock physics inversion for CO2 characterization at Sleipner

Hong Yan

Petroleum Geosciences
Submission date: July 2017
Supervisor: Børge Arntsen, IGP
Co-supervisor: Bastien Dupuy, SINTEF
                            Mohamed Anouar Romdhane, SINTEF

Norwegian University of Science and Technology
Department of Geoscience and Petroleum

Abstract

We combine Full-Waveform Inversion (FWI) and rock physics inversion to provide quantitative estimates of CO_2 saturation at Sleipner. The rock physics tool is based on uniform saturation and patchy saturation rock physics models. The patchy saturation model takes into account the attenuation at the mesoscopic scale. The uniform saturation model uses an effective fluid phase plugged into the Biot theory. The latter model will be mainly used in the Sleipner case. The rock physics inversion is implemented using an oriented Monte Carlo method (neighbourhood algorithm). We generate P-wave velocity using the FWI technology and then invert selected rock physics parameters using the rock physics inversion tool. The methodology is applied to both synthetic and real datasets. We test the feasibility of the rock physics inversion on synthetic data. We propose a method to extract the baseline frame properties using P-wave velocity combined with S-wave velocity and density. We estimate the CO_2 saturation using P-wave velocity model derived from 2D FWI and evaluate the associated uncertainty. We show that the CO_2 saturation at Sleipner can reach 90% with an uncertainty of 0.1 to 0.2. For another inline, we have a lower CO_2 saturation estimation because we are located 533 m away from the injection point. We estimate a Brie exponent, which is describing the distribution type, ranging between around 5 and 25, which indicates that the mixture is between patchy and uniform saturation.

ii

Preface

This thesis is made as a completion of the master education in Petroleum Geophysics at Norwegian University of Science and Technology in Norway, 2017.

Acknowledgements

I.   Table of contents

II.   List of figures

the Nordland shale and the Utsira sandstone, respectively. The blue lines indicate the rock frame moduli (mean value with maximum misfit of 0.1) inverted using the combination input of P-wave velocity, S-wave velocity, and density. The dotted lines correspond to the mean value of estimation plus/minus uncertainty.

III. List of tables

1 INTRODUCTION

With the increasing energy demand and consumption, the environmental protection and the mitigation of greenhouse gases have been hot topics from the last decade. Carbon dioxide is one of the most important gases to control the atmosphere temperature. The excessive emissions of the CO_2 have a substantial contribution to the climate change. In 2016, various countries in United Nations signed the Paris agreement on mitigation of the global warming. In this context, CO_2 Capture and Storage (CCS) into the subsurface is proposed as a potential mean of reducing the CO_2 emissions into the atmosphere and mitigating global warming. The newest annual report of 2016 (Institute, 2016) by global CCS institute shows that more than 20 large-scale CCS projects are under operation and more than 10 CCS projects will be started in the next decade.

CO_2 Capture and Storage requires careful monitoring to ensure the storage process and early detection of potential leakage related to geological hazards. Various geophysical techniques (including seismic and non-seismic techniques) are used prior to and during the injection process to characterize the changes in the subsurface properties. Seismic data are often recorded and several methods (for example, imaging methods like seismic migration, Full-Waveform Inversion, Amplitude Versus Offset analysis) are used to quantify the effect of CO_2 injection on seismic properties. In this work, we propose to study the changes of rock physics properties and quantify them during the injection of CO_2 at the Sleipner storage site in the North Sea.

Many empirical relations have been proposed to clarify the relation between seismic velocities and the porous rocks with respect to different parameters (clay content, porosity, and others). For example, Castagna et al. (1985) determined empirical regressions relating velocities with porosity and clay content for shaly sands of the Frio formation. Han et al. (1986) also presented a similar relation between P- and S-wave velocities based on the ultrasonic laboratory data. However, most of the empirical relations are valid only for given lithology and fluid type.

4D time-lapse seismic methods are widely considered as an important method to characterize the subsurface property changes due to CO_2 injection and migration. These techniques use repeated surveys to estimate changes in the reservoir and saturating fluid properties (brine, CO_2, gas mixtures and others). Repeated seismic surveys can be used together with other geophysical methods, such as Controlled-Source Electro Magnetic (CSEM) method, Amplitude Versus Offset (AVO) analysis, and gravity surveys. For example, Landrø (2001) introduced a time-lapse

approach based on time-shifts and AVO attributes to discriminate between pressure and saturation changes. Arts et al. (2004) applied a similar technique for CO_2 storage monitoring. They found that the presence of CO_2 has caused significant changes both in reflection coefficients and in travel time through the CO_2 plume. Arts et al. (2008) combined seismic monitoring with seabed gravimetry to help constrain the simulation of CO_2 migration. Meadows (2008) proposed a model-based approach to predict and quantify the effects of CO_2 injection for multiple reservoir properties and analyzed tuning effect including uncertainties. Since time-lapse seismic is highly dependent on the repeatability of the seismic survey, the reliability of this approach for fluid saturation changes could be discussed. White (2013) suggested an approach using time-lapse travel time differences in conjunction with log data to map the upper bound of CO_2 distribution. In this work, the pressure effects are calibrated by adopting a proper rock physics model. Bergmann and Chadwick (2015) proposed a method for volumetric estimation using time-shift analysis. They concluded that the behavior of fluid mixing could be observed in synthetic and real data application. Norman et al. (2008) studied the CO_2 saturation using time-lapse marine CSEM surveys at Sleipner. In this study, resistivity is very high due to the present of gases. This high sensitivity of resistivity change is combined with seismic data to help the study in gas saturation. Landrø and Zumberge (2017) combined the time-lapse seismic data with gravity data to address the seismic shadow zone problem and study the CO_2 saturation changes at Sleipner.

Seismic reflection Amplitude Versus Offset or Angle technology (AVO/AVA) is also widely used to characterize lithology and fluids. AVO is supposed to be more sensitive to changes in reservoir fluid than 4D time-lapse technology with the help of extra V_S information, rather than only V_P (Castagna et al., 1985). For example, Brown et al. (2007) proposed a workflow using AVO attributes under arbitrary fluid saturation and pressure conditions. With the help of laboratory experiments to upscale effects of small-scale heterogeneities, they concluded that AVO not only can determine the presence of CO_2, but also can track the changes in CO_2 saturation over time. However, in many cases, the CO_2 injection is associated with high-porosity high-permeability rocks, where V_S may be difficult to obtain accurately.

During the last decades, FWI has been introduced as a powerful high-resolution method to map seismic properties of the subsurface. The method aims at searching for the best model that minimizes the misfit between observed and modelled waveforms. Tarantola (1984) first introduced

FWI and implemented in time domain. However, FWI requires solving a highly nonlinear inversion problem and important computational resources. Cycle skipping is an important issue in particular when high frequencies are considered (Virieux and Operto, 2009). The quality of the seismic data seismic data (and especially for the low frequency content of the data), and the accuracy of the starting model play a key role for avoiding convergence towards local minima. The FWI method can be formulated in the time-space or in the frequency-space domain (Virieux and Operto, 2009). Time-domain FWI always highly depend on the starting model (Mora, 1987). While frequency-domain FWI can utilize the inversion procedure from low to high frequencies to ensure converging to the global minima (Song et al., 1995). The frequency domain FWI is more flexible in data selection while the time domain method can be less expensive.

The goal of our study is to investigate how to estimate rock physics properties of the Sleipner CO_2 storage pilot. To overcome the limitations of previous studies and obtain reliable reservoir properties, Dupuy et al. (2016a) described a two-step workflow with generic dynamic rock physics models. An effective fluid theory is applied to brine mixture with oil and gas. Selected poroelastic properties (rock frame and fluids properties) are estimated using an improved semi-global optimization (Neighborhood Algorithm, NA) method. In this thesis, we use a similar two-step workflow. In the previous sensitivity study (Dupuy et al., 2017; Yan, 2016), we already implemented the first step into the rock physics tool. Hereafter, we will focus on the study of this rock physics tool to different synthetic and real datasets. Combinations of FWI and rock physics inversion are used to derive CO_2 saturations. We will use 2D FWI, geological knowledge, log data, and rock physics inversion to quantify CO_2 distribution and evaluate its associated uncertainty. Part of this work has been published in Yan et al. (2017b) and Yan et al. (2017a).

2 METHODS

In this section, the FWI and the rock physics inversion methods are described. We consider two rock physics theories to define the poroelastic media partially saturated with brine and CO_2. In uniform saturation theory, we describe an effective fluid phase and then apply the extended Biot theory (Pride, 2005) to the homogenized medium. In patchy saturation theory, to study the multiphase flow induced attenuation in the porous media, we consider an extended white (White, 1975) model and use the Pride's equations (Pride et al., 2004) to obtain the effective frequency dependent moduli.

2.1 Full-Waveform Inversion (FWI)

The objective of the method is to generate a high-resolution image of the subsurface.

The FWI is proposed and first implemented in the time domain by Tarantola (1984). Pratt and Worthington (1990) give the first try in frequency domain Full-Waveform Inversion. Virieux and Operto (2009) analyse the advantages and disadvantages between time domain and frequency domain implementation. We use a similar frequency domain inversion method based on a preconditioned gradient approach as given by Pratt et al. (1998) and Romdhane and Querendez (2014). Figure 2-1 shows a representation of the approximate Hessian matrix.
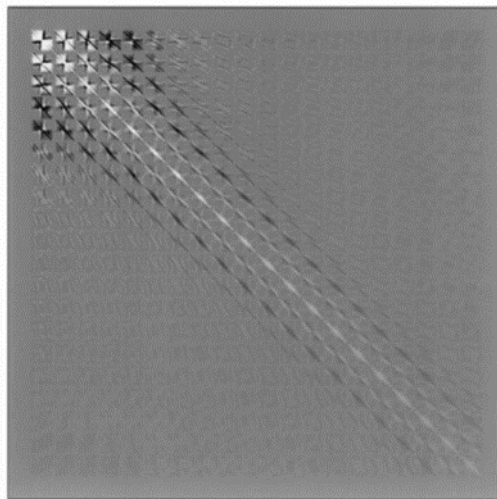
Figure 2-1. A representation of the approximate Hessian matrix $\Re e\left\{\mathbf{J}^T\mathbf{J}^*\right\}$ **by Pratt et al. (1998).**

An approximation of the Hessian operator with only the diagonal elements is used to save computation cost. The inversion process is developed following a misfit minimization procedure.

The misfit $\delta\mathbf{m}$ (perturbation model) and the gradient of the misfit at iteration n can be formulated as:

$$\delta\mathbf{m} = \frac{1}{2}\left\|\mathbf{d}_{\mathrm{mod}} - \mathbf{d}_{obs}\right\|^2,$$
$$\frac{\partial(\xi\mathbf{m}_n)}{\partial\mathbf{m}} = \Re e\left\{\mathbf{J}^T\delta\mathbf{d}^*\right\}. \tag{1}$$

Where $\dfrac{\partial(\xi\mathbf{m}_n)}{\partial\mathbf{m}}$ is the gradient of the misfit at iteration n. $\mathbf{d}_{\mathrm{mod}}$ and $\mathbf{d}_{obs}$ are the modelled and observed data, respectively. $\Re e$ is the real part of a complex number. $\mathbf{J}$ denotes the Jacobian matrix, thus $\mathbf{J}^T$ is the transpose of the Jacobian matrix. $\delta\mathbf{d}^*$ denotes the conjugate of the data residuals.

Therefore, the perturbation model can be defined as:

$$\delta\mathbf{m}_n = \mathbf{m}_{n+1} - \mathbf{m}_n. \tag{2}$$

The gradient method can be formulated as the link between the perturbation model and data residuals, and is given as:

$$\delta\mathbf{m}_n = -\alpha_n \frac{\partial(\xi\mathbf{m}_n)}{\partial\mathbf{m}}. \tag{3}$$

Where α_n is the step length at iteration n.

Proper scaling and regularization can be applied to ensure the computational stability. The approximated Hessian $\mathbf{H}_a$ is given by:

$$\mathbf{H}_a = \Re e\left\{\mathbf{J}^T\mathbf{J}^*\right\}. \tag{4}$$

If we only consider the diagonal term of the Hessian, the model that updates at iteration n can be estimated as:

$$\delta\mathbf{m}_n = -\alpha_n(diag\mathbf{H}_{a_n} + \lambda\mathbf{I})^{-1}\frac{\partial(\xi\mathbf{m}_n)}{\partial\mathbf{m}}. \tag{5}$$

Where λ denotes the damping parameter to ensure computational stability.

More details about this FWI method can see in Shin et al. (2001) and Pratt et al. (1998).

2.2 Rock Physics Inversion (RPI)

2.2.1 Forward formulation (rock physics models)

2.2.1.1 Uniform Saturation: effective fluid phase saturation

The widely used Gassmann equations (Gassmann, 1951) provide a way to link the saturated fluid to the bulk modulus of the rock at a low frequency. Biot (1956a) theory is combined with the Gassmann equation to account for dynamic poroelasticity. The Biot-Gassmann equations are valid under several assumptions. The Gassmann equations are valid within a low frequency limit and do not account for the chemical interaction between the grains and the fluid phases. The Biot theory is limited to homogeneous and isotropic media, which consists of only one type of grain. To be more realistic, Pride (2005) extended the Biot-Gassmann equations and involved a generalized dynamic permeability (Johnson et al., 1987). The extensive Biot-Gassmann theory can be applied to a multi-composite material saturated with a multi-fluid mixture. In addition, this approach is valid within a wide frequency range. More details on the assumptions and theory are given in Pride (2005).

The extensive Biot-Gassmann equations allow us to calculate the viscoelastic attributes for an effective fluid phase, which is referred as uniform saturation in our study. Biot (Biot, 1956a, b) demonstrate that there are three types of waves propagating in a porous fluid saturated media. They are compressional wave (P-wave), shear wave (S-wave), and an additional slow compressional wave (Biot wave or slow P-wave). The slownesses of these waves are formulated by Pride (2005) as:

$$S_S^2(\omega) = \frac{\rho - \rho_f^2 / \tilde{\rho}(\omega)}{G},$$

$$S_P^2(\omega) = \frac{\gamma(\omega)}{2} - \frac{1}{2}\sqrt{\gamma^2(\omega) - \frac{4(\rho\tilde{\rho}(\omega) - \rho_f^2)}{HM - C^2}},$$ (6)

$$S_{Biot}^2(\omega) = \frac{\gamma(\omega)}{2} + \frac{1}{2}\sqrt{\gamma^2(\omega) - \frac{4(\rho\tilde{\rho}(\omega) - \rho_f^2)}{HM - C^2}}.$$

Where ρ and ρ_f and $\tilde{\rho}(\omega)$ are bulk density, effective fluid density, and flow resistance density. The undrained bulk modulus K_U, the Biot modulus C, the shear modulus G and the fluid storage coefficient M are the mechanical moduli. The additional terms $\gamma(\omega)$ and H are defined by:

$$\gamma(\omega) = \frac{\rho M + \tilde{\rho}(\omega)H - 2\rho_f C}{HM - C^2},$$

$$H = K_U + \frac{4}{3}G.$$ (7)

The mechanical moduli are related to the homogenized porous solid. K_U, C, and M are formulated as:

$$K_U = \frac{\phi K_d + (1 - (1 + \phi)K_d / K_s)K_f}{\phi(1 + \Delta)},$$

$$C = \frac{(1 - K_d / K_s)K_f}{\phi(1 + \Delta)},$$ (8)

$$M = \frac{K_f}{\phi(1 + \Delta)}.$$

Where the term Δ is given by:

$$\Delta = \frac{1 - \phi}{\phi}\frac{K_f}{K_s}\left(1 - \frac{K_d}{(1 - \phi)K_s}\right).$$ (9)

Where porosity ϕ is defined as the ratio between void and total volume in the solid matrix. K_d, G_d, and K_f are the frame bulk modulus, frame shear modulus and the effective fluid bulk modulus, respectively.

Thus, we can deduce the effective wave velocities and quality factors, and formulated as:

7

$$V_{p,Biot,S}(\omega) = \frac{1}{\text{Re}\left(S_{p,Biot,S}(\omega)\right)},$$

$$Q_{p,Biot,S}(\omega) = \frac{\text{Im}\left(S^2_{p,Biot,S}(\omega)\right)}{\text{Re}\left(S^2_{p,Biot,S}(\omega)\right)}. \tag{10}$$

We consider the solid material consists of different compositions. We compute the grains bulk moduli K_S by averaging the bounds (Hashin and Shtrikman, 1963). The grain density ρ_S is computed with consideration of the compositional minerals in Utsira sandstone. Then, we use arithmetic average for the bulk density, which is given by:

$$\rho = (1-\phi)\rho_s + \phi\rho_f. \tag{11}$$

For the frame properties, Pride (2005) suggests two methods to obtained the drained frame moduli K_d and G_d. He introduces the consolidation parameter cs which allow linking the frame moduli to the solid grain moduli. This approach is valid for consolidated sandstone, which has a consolidation parameter in the range of $2 < cs < 20$. For unconsolidated sandstone, the Walton theory (Walton 1987) is more favourable. In the rock physics model, we considered the two approaches in the sensitivity analysis (Yan, 2016). In the application part in this paper, as the sandstone reservoir at Sleipner is unconsolidated, we do not use the cs term but rather the separated bulk and shear moduli.

Johnson et al. (1987) proposed a frequency dependent dynamic permeability $k(\omega)$, which correct the seismic permeability and differentiate the viscous and inertial predominant effects at low and high frequency domain (Dupuy et al., 2016). The dynamic permeability is expressed by Johnson et al. (1987):

$$k(\omega) = \frac{k_0}{\sqrt{1 - \frac{1}{2}i\frac{\omega}{\omega_c} - i\frac{\omega}{\omega_c}}}. \tag{12}$$

Where ω is the angular frequency. ω_c is the characteristic angular frequency which is associated with the maximum attenuation. k_0 is the hydraulic permeability. The characteristic angular frequency ω_c can be formulated with the cementation factor m, the effective fluid viscosity η and the fluid density ρ_f (Adler et al., 1992).

Biot (1956a) proposed another frequency depend property to extend the poroelasticity theory to the full frequency range. The frequency depend parameter is referred as the complex flow resistance $\tilde{\rho}(\omega)$, and is defined by:

$$\tilde{\rho}(\omega) = \frac{i\eta}{\omega k(\omega)} \ .$$ (13)

Where i denotes the complex number.

We define the effective fluid phase properties for the CO_2 and brine mixture using different averaging methods. First, we use the empirical law (Brie et al., 1995) for the effective fluid bulk modulus K_f. Brie et al. (1995) proposed an empirical exponent e which varies from 1 to 40 associated to different mixture trends. S_W is the water (brine) saturation. K_{CO2} and K_W is the CO_2 and brine bulk moduli. The effective fluid bulk modulus K_f is formulated as:

$$K_f = (K_{CO2} - K_W)S_W^e + K_{CO2}.$$ (14)

Carcione et al. (2006) suggest using a brie exponent equal to 5 for the brine and CO_2 mixture.

Teja and Rice (1981) propose an equation for the effective fluid viscosity η. Considering the CO_2 viscosity η_{CO2} and brine viscosity η_W, the effective fluid viscosity η can be formulated as:

$$\eta = \eta_{CO2}\left(\frac{\eta_W}{\eta_{CO2}}\right)^{S_W} \ .$$ (15)

The effective density ρ_f is given as the arithmetic average.

$$\rho_f = S_W\rho_W + (1-S_W)\rho_{CO2} \ .$$ (16)

Where ρ_W is the brine density. ρ_{CO2} is the CO_2 density. Hereafter, we will refer this model as the 'Brie rock physics model' and 'uniform saturation', which indicate the model using equations (14), (15) and (16). It can be uniform mixing or patchy mixing depending on the Brie exponent.

2.2.1.2 Patchy Saturation

White (1975) describes a patchy model for porous media saturated with multi-fluids. This model allows considering the pressure gradient generated by multi-fluids. Pride et al (2004)

reformulate and extend the White model using frequency dependent parameters. This allows taking into account wave induced fluid flows and associated attenuation and dispersion created by mesoscopic heterogeneities (fluid patches). In contrast to the uniform saturation, the fluids in the reservoir are not well mixed in the patchy saturation theory and the fluid-solid interactions are explicitly considered. The extended White model involves the spherical gas pocket and assumes the patch size should be much smaller than the detected wavelength. The assumptions of the extended White model are described by Pride (2005). Pride et al. (2004) point out that the extended patchy saturation has a limited range of validity for relative low and high brine saturations. Therefore, we consider the patchy model only for high brine saturation condition ($S_W \geq 80\%$ or similarly, $S_{CO2} \leq 20\%$) and low brine saturation ($S_W \leq 20\%$ or similarly, $S_{CO2} \geq 80\%$) in the sensitivity analysis (Yan, 2016). With the consideration of geology studies at Sleipner, the case of high brine saturation is more likely to happen at Sleipner. The fluid patch is assumed spherical and a is the radius for the patch sphere. L_l is a geometrical term indicating the distance with zero pressure in the brine. The contact surface S between the saturated fluids and the elemental volume V form another geometrical term V/S. Table 2-1 illustrates the parameters of the fluid properties corresponding to the high and low brine saturation conditions.

Table 2-1: The fluid parameters corresponding to the high and low brine saturations.

Saturation Condition	High Water Saturation ($S_{CO2} \leq 20\%$)	Low Water Saturation ($S_{CO2} \geq 80\%$)
L_1^2	$\dfrac{9a^2}{14S_{CO2}^{2/3}}\left(1+\dfrac{7S_{CO2}^{1/3}}{6}\right)$	$\dfrac{a^2}{15}$
V/S	$\left(\dfrac{aS_{CO2}^2}{3}\right)^2$	$\left(\dfrac{aS_W}{3}\right)^2$
ρ_f	ρ_W	ρ_{CO2}
$\tilde{\rho}(\omega)$	$\dfrac{i\eta_W}{\omega k_0}$	$\dfrac{i\eta_{CO2}}{\omega k_0}$

Pride et al. (2004) reformulate the Skempton modulus $B(\omega)$, the bulk undrained modulus $K_U(\omega)$, the Biot modulus $C(\omega)$, and the fluid storage coefficient $M(\omega)$, by using the stiffness coefficients a_{ij} ($i,j = 1, 2, 3$) and the Biot-Willis constant α:

$$
\begin{aligned}
B(\omega) &= \frac{-a_{12}\left(a_{33} - \gamma(\omega)\right) + a_{13}\left(a_{23} + \gamma(\omega)\right)}{\left(a_{22} - \gamma(\omega)\right)\left(a_{33} - \gamma(\omega)\right) - \left(a_{23} + \gamma(\omega)\right)^2}, \\
K_U(\omega) &= \left[\frac{1}{K_d(\omega)} + B(\omega)\left(a_{12} - \frac{a_{13}(a_{23} + \gamma(\omega))}{a_{33} - \gamma(\omega)}\right)\right]^{-1}, \\
C(\omega) &= B(\omega)K_U(\omega), \\
M(\omega) &= B(\omega)\frac{K_U(\omega)}{\alpha}.
\end{aligned}
\tag{17}
$$

Where $\gamma(\omega)$ is the inertial transport coefficient describing the mesoscopic flow, and is given as:

$$
\gamma(\omega) = \frac{S_W k_0}{\eta_W L_1^2}\sqrt{1 - \frac{i\omega}{\omega_p}}, \tag{18}
$$

where ω_p is the transition frequency associated with a high frequency mechanism.

Using the similar equations in uniform saturation (see equations (6), (7), and (10)), we can deduce the velocities, quality factors in the patchy saturation model. More details for the patchy saturation theory are given in Dupuy and Stovas (2014). Hereafter, we will refer this model as 'patchy saturation' or 'patchy model', which is different from patchy mixing of Brie rock physics model.

2.2.2 Inversion formulation

The rock physics inversion process estimates the poroelastic parameters from various combination of viscoelastic attributes (P- and S-wave velocities, P- and S-wave quality factors, and density).

We assume that $\vec{d}$, $\vec{m}$ and g represents the data vector, the model vector and the linking function for the data and model, respectively. Therefore, the forward modelling process can be described as:

$$\vec{\mathbf{d}} = g(\vec{\mathbf{m}}). \tag{19}$$

The relation function g is the rock physics model, for uniform and patchy saturation models in our study. The inverse of g cannot be computed and the system is solved by a semi-global optimization method.

We implement the inversion process by using the NA algorithom. Sambridge (1999) introduces the NA algorithm method, which is a Monte Carlo oriented method. The NA method is searching for the minimum discrepancy between the observed data $\vec{\mathbf{d}}_{obs}$ and the estimated data $g(\vec{\mathbf{m}})$ from the forward modelling. The scalar misfit function $C(m)$ can be given as a L_2 norm:

$$C(m) = \frac{1}{2}\left[(\vec{\mathbf{d}}_{obs} - g(\vec{\mathbf{m}}))^T(\vec{\mathbf{d}}_{obs} - g(\vec{\mathbf{m}}))\right]. \tag{20}$$

The implementation of NA algorithm method has only two control parameters: the number of new models at each iteration and the resampling size of Voronoï cells. The misfit of the previous iteration decides the new sampling of Voronoï cell for the next iteration. Dupuy et al. (2016) and Sambridge (1999) provide more details of the rock physics inversion and NA algorithom, respectively.

In our sensitivity study (see (Yan, 2016)), an iteration number of 1000 and a resampling factor of 10 has been shown to be sufficient to ensure the accuracy of the results. Whereas, the iteration number is reduced for synthetic and real data applications for the computational efficiency. For the estimation of the frame moduli (Yan, 2016), the iteration number is reduced to 500 to optimize the computational process. For the CO_2 saturation estimation, we reduce the iteration number to 400. This number is selected based on the misfit variation versus iteration number (see Appendix B).

2.3   Summary of the sensitivity

In the previous study on the sensitivity and well baseline application (Yan, 2016), we adopted a similar two-step workflow as described by Dupuy et al. (2016). We demonstrated the use of rock physics inversion for estimating CO_2 properties, saturations, and rock frame properties at Sleipner CO_2 storage site in the North Sea (Yan, 2016). We investigated the elastic wave velocities and quality factors for the Utsira unconsolidated sandstone containing CO_2 and brine

mixture and modeled the effect of various CO_2 saturations on viscoelastic properties. Figure 2-2 shows the P-wave velocity changes with different brine and CO_2 saturations for uniform saturation with different Brie exponents and for patchy saturation with a bubble size equal to 0.01 m.
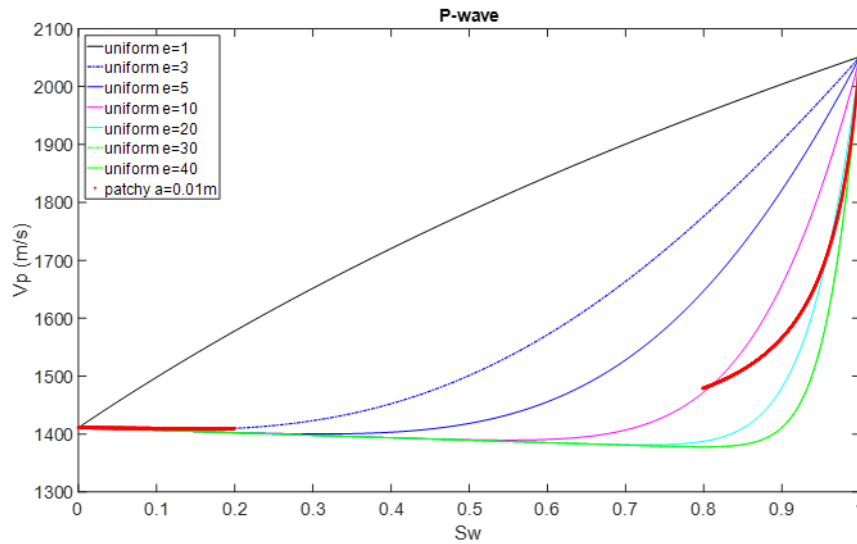
Figure 2-2. P-wave velocity variation with brine saturation for uniform saturation with various Brie exponent and patchy saturation with bubble size *a* of 0.01 m.

The sensitivity tests are conducted using the extracted viscoelastic properties for uniform and patchy saturation to invert selected poroelastic parameters from various input data parametrizations. By analysis the results of the sensitivity tests, we found the following conclusions:

1) The bubble size *a* in patchy saturation model cannot be well estimated.

2) The critical frequency of patchy saturation is more variable compared with the one for uniform saturation model.

3) Both patchy and uniform saturation models have better estimations of CO_2 properties and brine saturation when the brine saturation is high.

4) The brine saturation (thus CO_2 saturation) can be estimated from only V_P input with more or less uncertainty. CO_2 saturation can be well estimated for low CO_2 saturation condition.

5) The additional information (quality factor of P-wave, S-wave velocity, density information) can help the estimation of CO_2 bulk modulus and reduce the uncertainty on CO_2 saturation estimates.

In a second step, we applied the rock physics inversion to the log data before CO_2 injection to estimate the rock frame properties at Sleipner. With density and S-wave velocity computed

with an empirical relation, we can derive an estimation of the drained bulk and shear moduli of the reservoir which are similar to those derived by Lindeberg (2013).

2.4 Workflow outline

In this section, we outline the basic workflow that we used for all the applications. We will explain the workflow for the baseline and monitor CO_2 injected application applications.

2.4.1 Baseline application

The baseline information is essential for the later estimation of CO_2 saturation. Based on the sensitivity analysis, we know that better estimations of the rock frame properties can be achieved by involving additional proper empirical S-wave information and density. We apply a similar procedure to estimate the rock frame properties (K_d, G_d) for fully brine-saturated baseline. We modify the baseline inversion code to handle a 2D case. For baseline information, we propose different strategies adopted for different cases. For the true synthetic model and FWI synthetic model application, we extract the baseline information using one trace with less CO_2 impacts and extend laterally along the layer variation carefully to obtain the associated frame properties. For the real data of inline 1881, we apply the extracted baseline information from log data. For the real data of inline 1838, we use the FWI derived baseline information.

2.4.2 Monitor application

From a practical point of view, the information of the real data is normally limited to P-wave velocity. We use FWI to generate P-wave velocity models. The initial P-wave velocity data prior to FWI would be obtained by a generated synthetic model or real dataset from seismic. Data processing is applied before the application of FWI. We select an area of the P-wave velocity model obtained from FWI. From the sensitivity analysis (Yan, 2016), we know that providing a priori properties to reduce the unknowns in the inversion process can increase the stability of inversion. Therefore, we prepare the a priori rock properties for the rock physics inversion.

To start the application study, we also modify our rock physics inversion code to be adaptable for the 2D application with given grids design. The following cases are considered:

Case 1: Estimation of fluid saturation assuming a known Brie exponent e using uniform saturation model for partially saturated media.

Case 2: Estimation of fluid saturation and Brie exponent e using uniform saturation model for partially saturated media.

Case 3: Estimation of fluid saturation and fluid phase properties using uniform saturation model for partially saturated media.

Case 4: Estimation of fluid saturation using patchy saturation model for partially saturated media.

Based on the sensitivity studies (Dupuy et al., 2017; Yan et al., 2017b) of the rock physics inversion tool, we found that there are always many good models with low misfit. For example, the low misfit area (pink region in Figure 2-3 (a)) shows that the trade-off between Brie exponent e and brine saturation S_W. The best estimated model (blue cross, lowest misfit) is located at the upper part of the low misfit region (Figure 2-3 (a)). We also found that the best estimation with the minimum misfit of frame bulk modulus is located at the bound of the low misfit area (Figure 2-3 (b)). Therefore, we can expect to give a more realistic estimation when we consider average of all the low misfit models. In this sense, we select all the models with a misfit lower than a given maximum value of misfit. In addition of the mean value, we estimate the one standard deviation to give an idea of the uncertainty. It is worth noting that we also apply similar uncertainty analysis on the baseline inversion process for the estimation of reservoir frame moduli. The uncertainty in our study is an absolute value and not in percentage.
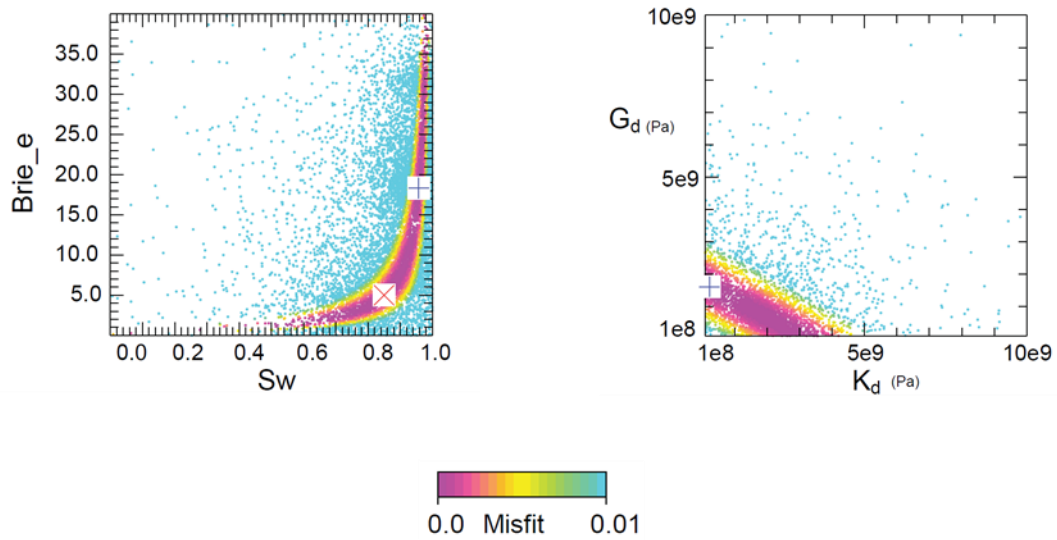
(a) Uniform saturation (Sw = 85%)

(b) Utsira sand at 930m (one sample in the Utsira sandstone from the well 15/9 - A16)

Figure 2-3. Panel (a) indicates the estimations of Brie exponent e and brine saturation S_W for uniform saturation from P-wave velocity input only. Panel (b) indicates the estimation of frame moduli for Utsira sandstone of log data from P-wave velocity only. The blue cross indicates the best model and the red cross indicates the true model.

3 SLEIPNER GEOLOGICAL SETTING AND ROCK PHYSICS PROPERTIES

Since 1996, the Sleipner site, known as the world's first industrial scale CO_2 storage operation (Chadwick et al., 2004), is operated in the North Sea. About 1 million tons per year of CO_2 is separated from production and injected into the underground saline aquifer at Sleipner (Carcione et al., 2006). The CO_2 is injected into the Utsira Formation at a depth of 1012 m below the sea level through a deviated well (Arts et al., 2008).

The reservoir sand comprises two big depositional basins, which are lying on the North Sea Basin at depths from 550 m and 1500 m (Chadwick et al., 2000). The CO_2 is being injected at the part in the southern Sleipner where the thickness of the Utsira sandstone is about 300 m (Figure 3-1). The reservoir extends about 400 km from south to north, which consists of late Miocene to early Pliocene dominantly sandy unit and some shaly intra-reservoir horizons (Chadwick et al., 2000).
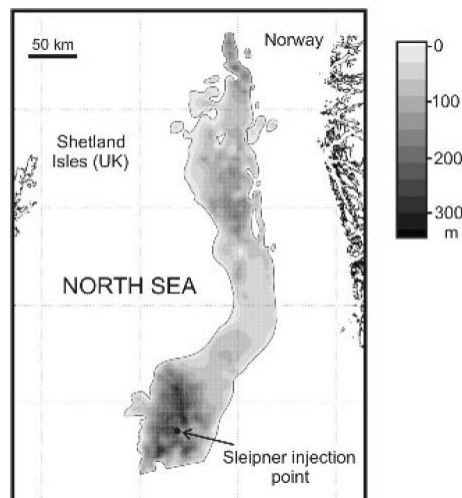
Figure 3-1. Map of the Utsira sand reservoir thickness (Arts et al., 2004).

Figure 3-2 shows the geological structure of the Utsira Sand, which is surrounded by the Nordland shale on the top and the Hordaland shale on the bottom. Shale layers are clearly visible on the gamma ray (GR) response with values higher than 80 API (Dupuy et al., 2017; Yan, 2016). The Utsira Formation is a highly porous, weakly consolidated, highly permeable sandstone which provides a good reservoir condition for high injection rate through only one single well (Michael et al., 2010). The intra-reservoir shale layers are very thin and can be less than 1 m

thick (Zweigel et al., 2000). The intra-reservoir shales are regarded as the low permeability barriers, which impact the CO_2 top wards migration (Chadwick et al., 2004).
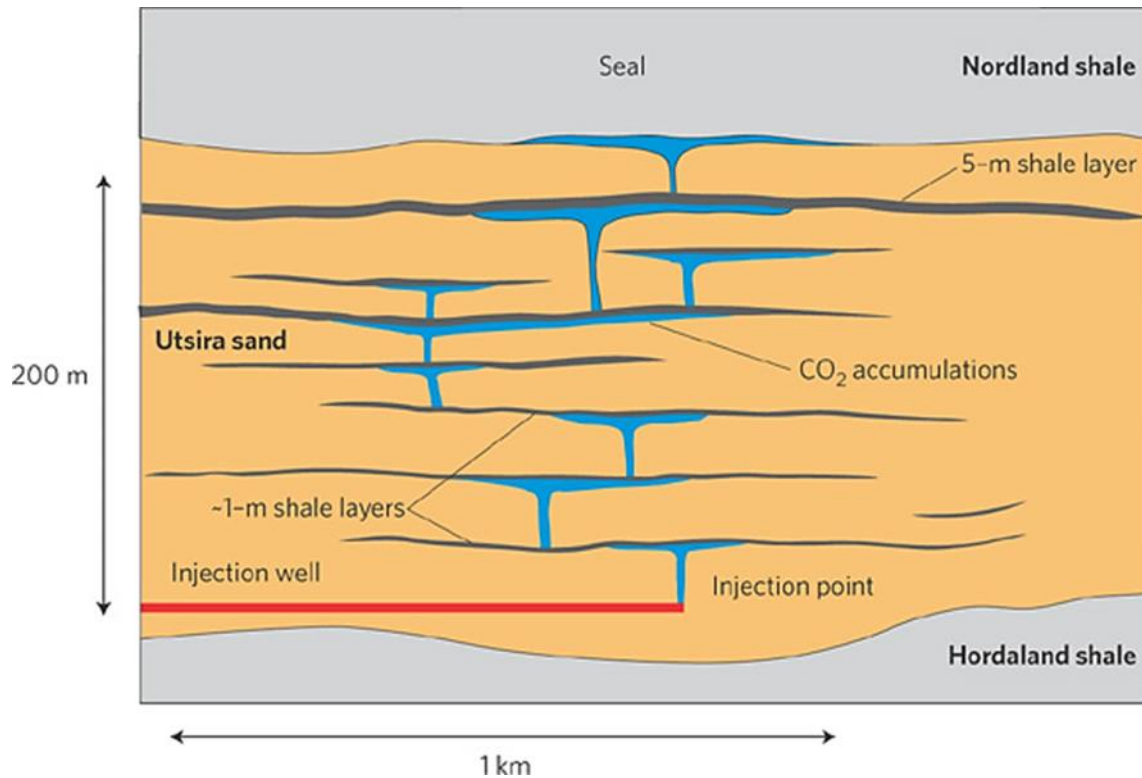
Figure 3-2: Sketch of geological model for CO_2 migrations (Bickle, 2009).

The caprock shale is known as the Nordland shale, which comprises dominantly kaolinite, illite, quartz, and smectite (Gaus et al., 2005). Based on the cutting analysis, that the caprock is assumed to be a good quality seal with a low probability of leakage (Chadwick et al., 2004).

For the application of rock physics inversion, we need to determine a set of realistic a priori poroelastic properties at Sleipner. The a priori parameters are extracted based on the existing geological studies on Sleipner field. Grain moduli of the Utsira sandstone and the Nordland shale are calculated by averaging Hashin-Shtrikman bounds (Hashin and Shtrikman, 1963; Mavko et al., 2009). Effective grain density for the Utsira sandstone and the Nordland shale are computed by using volume weighted averages, the specified calculation are clarified in the sensitivity tests (Yan, 2016). The cementation parameter m is assumed to be 1 for the weakly consolidated sandstone and mudstone. The permeability for the Utsira Formation is high and ranges from 1×10^{-12} m^2 to 3×10^{-12} m^2 (Boait et al., 2012). We use an average permeability of 2×10^{-12} m^2. Porosity of the Utsira sandstone ranges between 27% and 42% (Chadwick et al., 2004). The drained frame moduli (K_d and G_d) of the Utsira sandstone are taken from Lindeberg (2013),

while the drained frame moduli of the Nordland shale are obtained by rock physics inversion for the fully brine saturated baseline data. The a priori properties of the Utsira sandstone and the Nordland shale properties used in our application studies are summarized in Table 3-1. The shale grain properties are applied to all the interbedded shales. In previous log data application study (Yan, 2016; Yan et al., 2017b), we use baseline information from well 15/9 - A16 before the CO_2 injection started. More details for K_S and ρ_S are illustrated in Appendix D and Appendix E.

Table 3-1. The composite Utsira sandstone and Nordland shale properties.

Lithology	Solid Properties		Frame Properties	
	K_S	ρ_S	m	k_o
	GPa	kg/m^3		m^2
Utsira Sandstone	39.29	2663.5	1	2.00×10^{-12}
Nordland Shale	22.6	2390	1	1.47×10^{-17}

For the a priori properties of the saturating fluids, we consider a CO_2 and brine mixture after CO_2 injection and a fully brine saturated medium before CO_2 injection. At the pressure and temperature of the reservoir, the bulk modulus of brine is 2.3 GPa (Boait et al., 2012), and the density of brine is 1030 kg/m^3 (Mavko et al., 2009). Most of the CO_2 is stored in a supercritical state (Arts et al., 2008) and we use a relative high density of 700 kg/m^3 for the CO_2 phase. Since the initial hydrostatic pore pressure of 8 MPa is considered (Furre et al., 2015; Furre and Eiken, 2014), the range of K_{CO2} is estimated to be 0.02 GPa - 0.075 GPa (Ghaderi and Landrø, 2009; Span and Wagner, 1996). We use value of 0.075 GPa for bulk modulus of CO_2 (Lindeberg, 2013). The viscosity property of CO_2 is discussed in many papers and depends on the temperature and pressure (Gasda et al., 2012; Singh et al., 2010). However, the effective viscosity influence on seismic velocity is minor in low frequency (Dupuy et al., 2016), and we use $6 \times 10^{-}$

[5] Pa.s for the CO_2 viscosity. The saturating fluids properties used in our application studies are summarized in Table 3-2.

Table 3-2. Brine and CO₂ fluid properties.

Fluid phase	Fluid properties		
	η	ρ_f	K_f
	Pa.s	kg/m^3	GPa
Brine	6.90×10^{-4}	1030	2.30
CO_2	6.00×10^{-5}	700	0.075

4 SLEIPNER WELL 15/9-A16

In this section, we are going to apply the rock physics inversion to the baseline log data (i.e. before injection). The objective is to evaluate the uncertainty in the estimation of the rock frame moduli and to see if the estimations using the mean values are different from the model with the lowest misfit.

4.1 Data preparation

We use the same combination input data of (V_P, V_S and density) for the baseline application as described by Yan (2016). The combined S-wave velocity is derived by Vernik's relation (Vernik et al., 2002). The grain density is derived from Hashin-Shtrikman bounds, and thus we derived the density porosity. We use an iteration number of 500 and a resampling size of 10. Figure 4-1 shows input information of P- and S-wave velocities, density and the density-derived porosity. The thin interbedded shale layers within the Utsira sand formation can be discriminated from the log data.
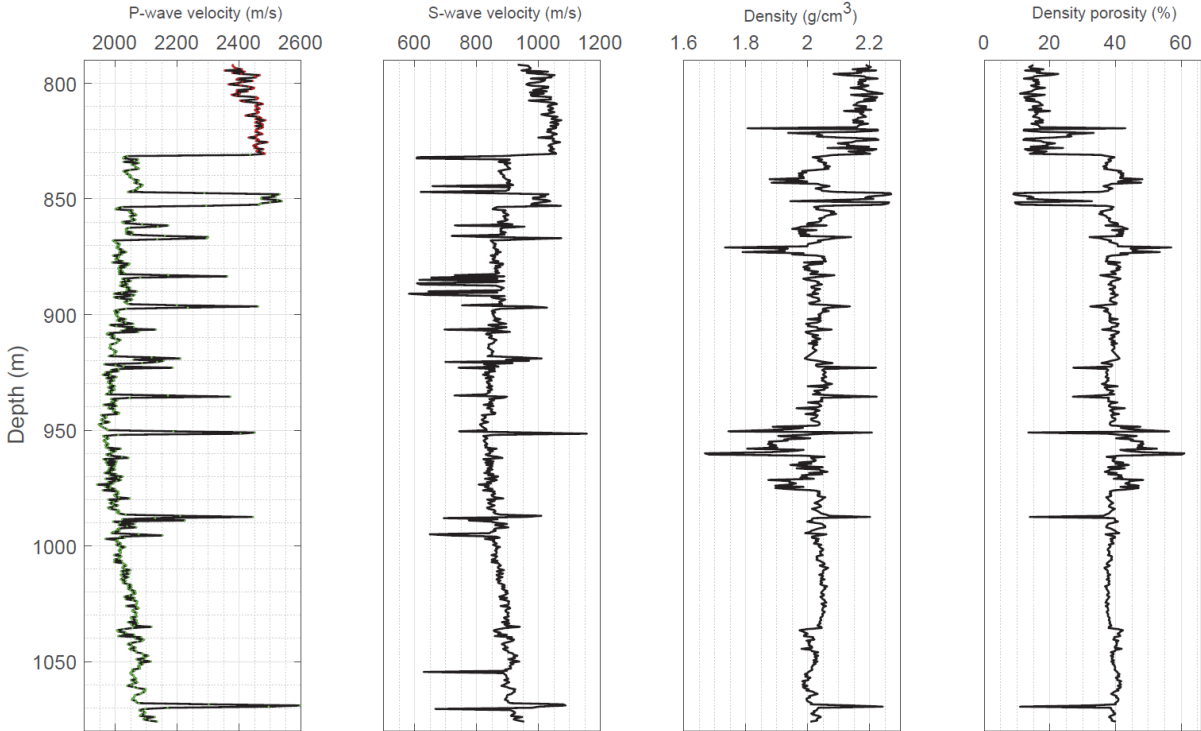
Figure 4-1. From left to right: P-wave velocity, S-wave velocity, bulk density and the density log derived porosity. P-wave velocity and density responses are log data from well 15/9-A16. S-wave velocity is derived using Vernik's relation. Density porosity log is derived from bulk density log and the grain density computed from Hashin-Shtrikman bounds. The red and green dots indicate the caprock of the Nordland shale and the Utsira sandstone, respectively.

4.2 Estimation of frame moduli

Figure 4-2 shows the estimations of frame bulk modulus K_d and frame shear modulus G_d. The mean values of the extracted frame moduli are estimated with a threshold misfit of 10%. The mean estimation of the frame moduli (K_d, G_d) are similar with the one corresponding to the lowest misfit result and give a similar slight increasing trend with the increasing of depositional depth. The deviations of the frame shear modulus are slightly higher than that for the frame bulk modulus. To conclude, the difference between the mean estimation of the frame moduli (K_d, G_d) and the one corresponding to the lowest misfit result is very small.
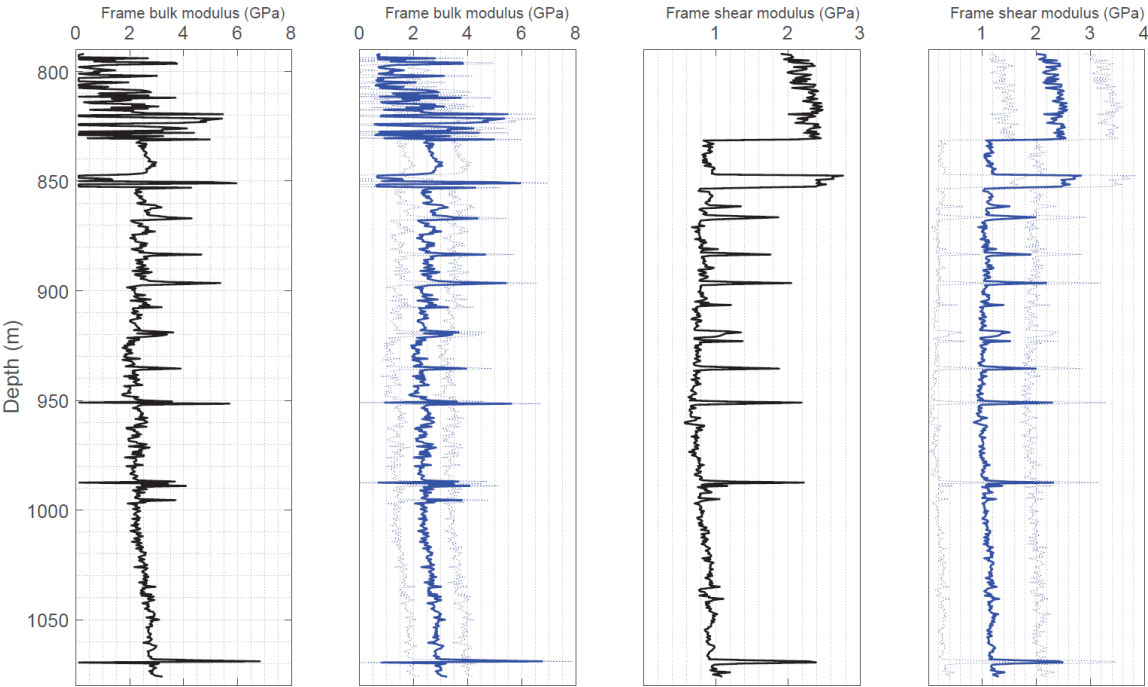
Figure 4-2. From left to right: frame bulk and shear moduli, which are derived from the combination input of P-wave velocity, S-wave velocity and density. The black lines indicate the best estimations with the lowest misfit models. The blue lines indicate values of a set of models have misfit lower than 0.1. The dotted lines correspond to the mean value of estimation plus/minus uncertainty.

We also try a different threshold (10 instead of 0.1). The conclusion is that the choice of the misfit threshold will not have a big impact on the mean estimation. The figures are given in Appendix A.

5 SYNTHETIC SLEIPNER MODEL

This chapter uses the synthetic Sleipner model from Traub (2008). The true synthetic model is shown in Figure 5-1. We conduct several tests to figure out various effects by different models on the estimation of CO_2 distribution.
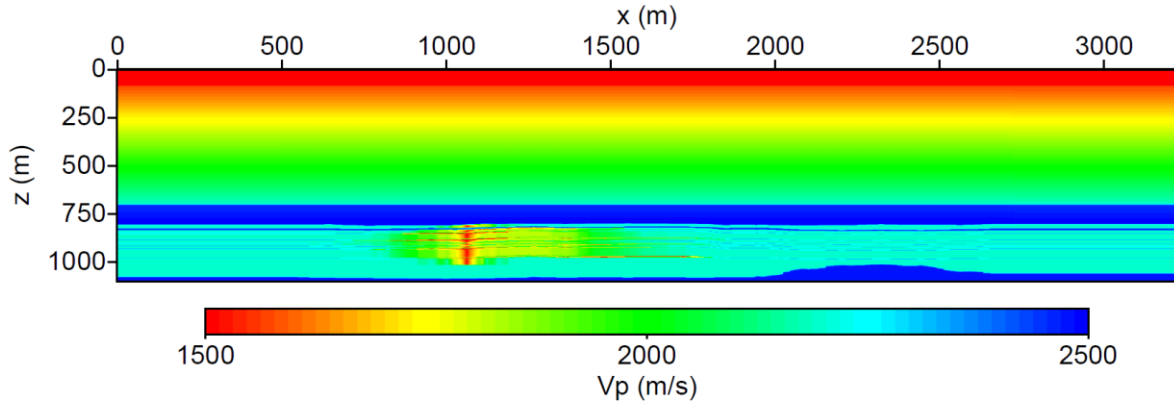
Figure 5-1. Initial 2D synthetic true model.

5.1 Data preparation and a priori rock properties

In this section, we show the results using rock physics inverted rock frame information and prepare the a priori rock properties for RPI. We select a region focus on CO_2 saturated layers from 765m (Figure 5-2). To extract a more reliable baseline reservoir properties, we select a trace as shown in Figure 5-2. Then, we extract the frame moduli from the baseline using inputs of P-wave velocity, S-wave velocity and density. S-wave velocity and the bulk density are derived using Vernik's and Gardner's relations (Mavko et al., 2009), respectively. The Vernik's relations for sand and shale are given by:

$$V_S = (-1.267 + 0.372V_P^2 + 0.00284V_P^4)^{0.5} \text{ (km/s) for sandstone,}$$
$$V_S = (-0.79 + 0.287V_P^2 + 0.00284V_P^4)^{0.5} \text{ (km/s) for shale.}$$

(21)

The Gardner relation is given by:

$$\rho = 1.66V_P^{0.261}.$$

(22)

Where the bulk density ρ is in unit of g/cm^3, the P-wave velocity V_P is in km/s. The corresponding porosity is derived using the Gardner relation derived density and grain density, and can be computed by volumetric average as:

$$\phi = \frac{(\rho_S - \rho)}{(\rho_S - \rho_W)}. \tag{23}$$

The deduced estimation of the frame moduli is derived using mean values of the models with misfit lower than 0.1 (Figure 5-3).
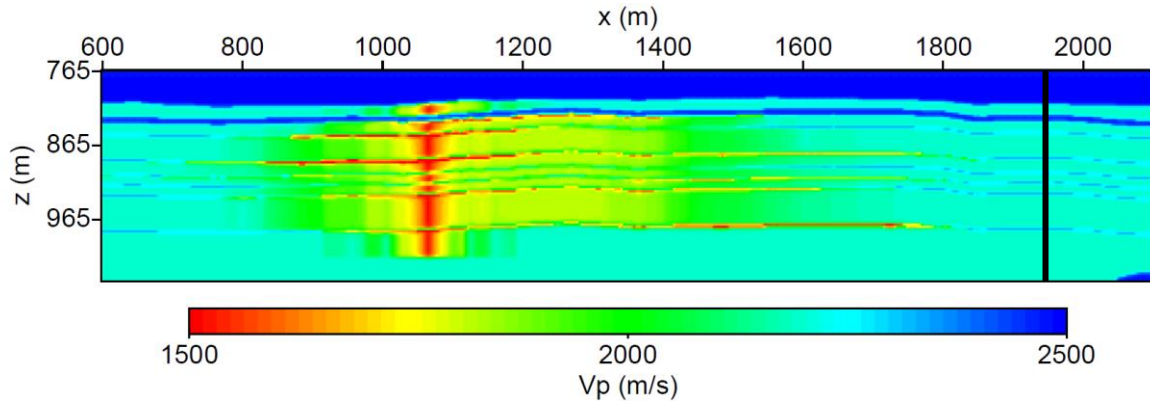
Figure 5-2. Synthetic P-wave velocity model for selected region. The black line indicates the extracted vertical profile (x = 1947 m).
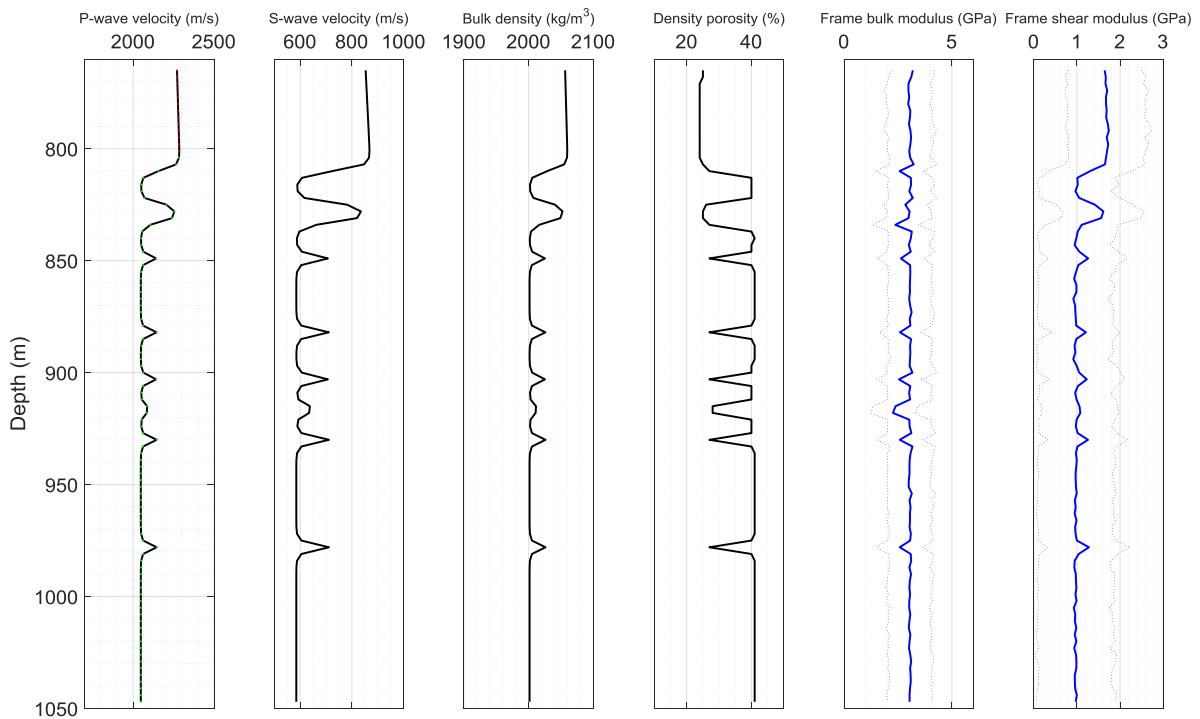
Figure 5-3. From left to right: P-wave velocity, S-wave velocity, bulk density, density porosity, frame bulk modulus and frame shear modulus. The red and green dots indicate the caprock of the Nordland shale and the Utsira sandstone, respectively. The blue lines indicate the rock frame moduli (mean value with maximum misfit of 0.1) inverted using the combination input of P-wave velocity, S-wave velocity, and density. The dotted lines correspond to the mean value of estimation plus/minus uncertainty.

From the P-wave velocity model shown in Figure 5-2, we estimate the P-wave vertical gradient in order to define the boundary between shale and sand. As shown in Figure 5-4, a distinctive positive value of the first derivative is expected to be related to a lithology change from sand to shale. While a distinctive negative value of the first derivative is expected to be related to a lithology change from shale to sand. Meanwhile, we should be careful in the region with CO_2 induced reduction in velocity. Thus, we generate the 16 layers numbered with constant number from 1 to 16 (as shown in Figure 5-4).
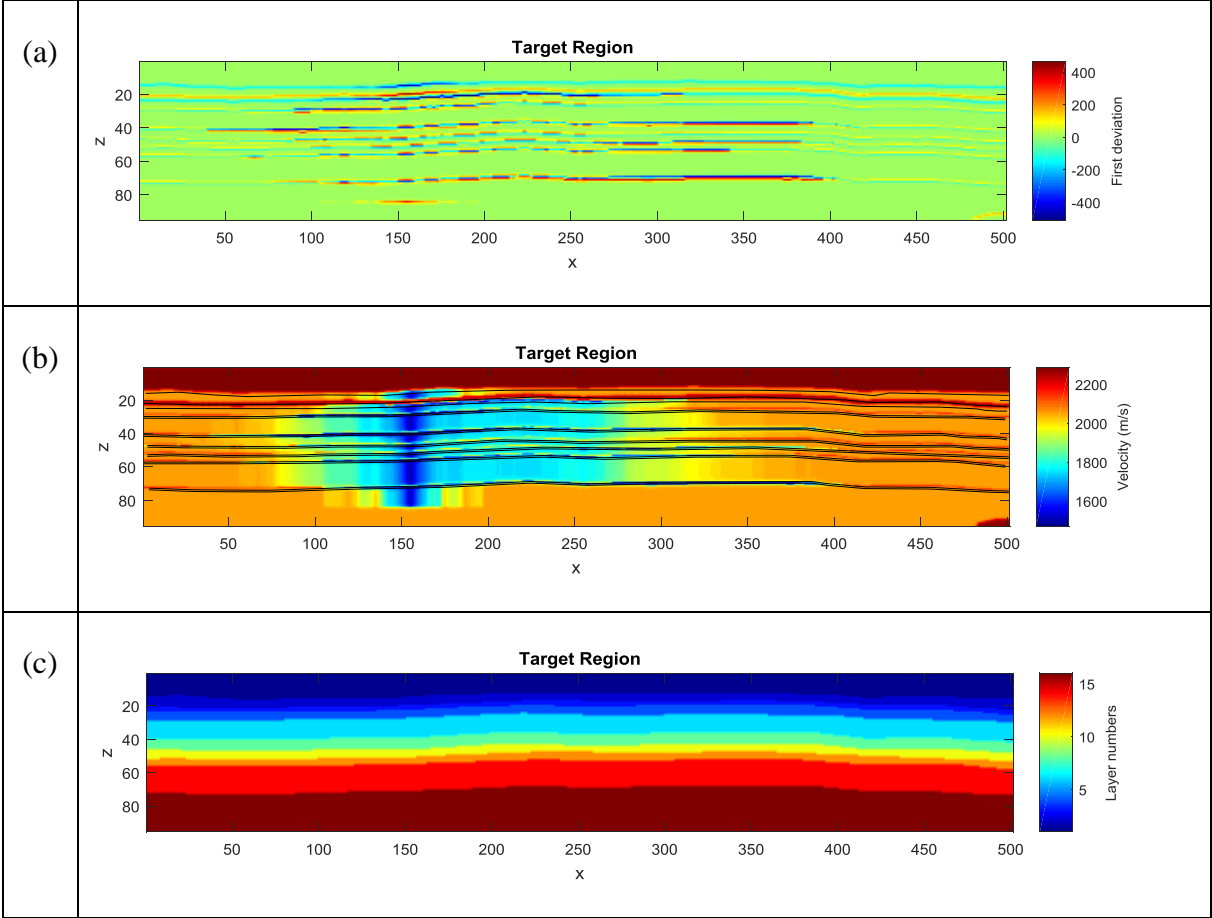
Figure 5-4. From top to bottom: (a) first derivative of P-wave velocity with respect to the depth, (b) velocity model with extracted boundaries, and (c) the generated 16 layers. The vertical axis is corresponding to the row number of the matrix, while the horizontal axis is the column number of the matrix.

Therefore, we construct the corresponding rock frame properties using the structural model and the estimated frame moduli. We interpolate linearly for each corresponding layer based on the extracted baseline information. The procedure is repeated for all the traces. Thus, we create the a priori information of the frame properties (Figure 5-5).
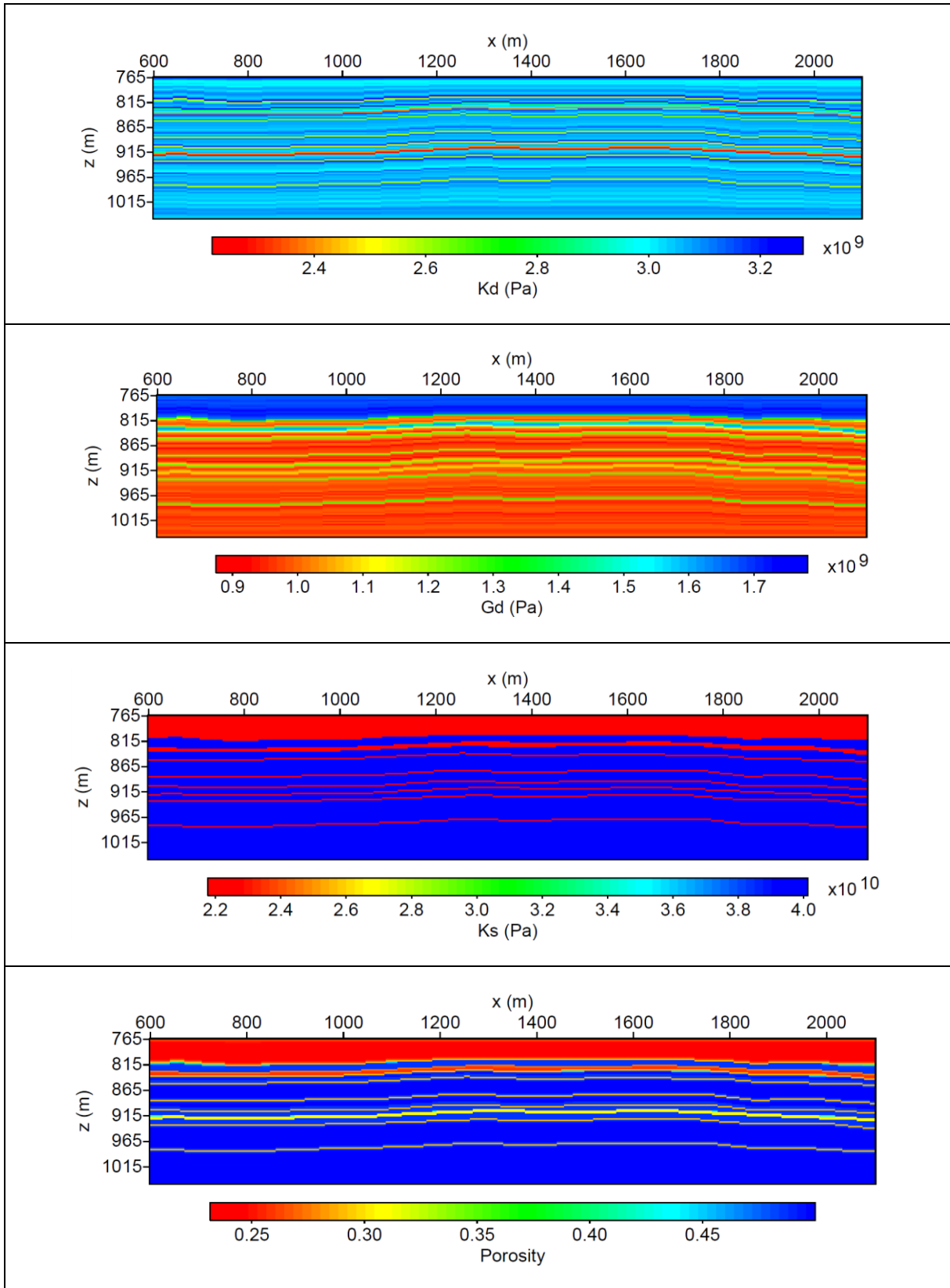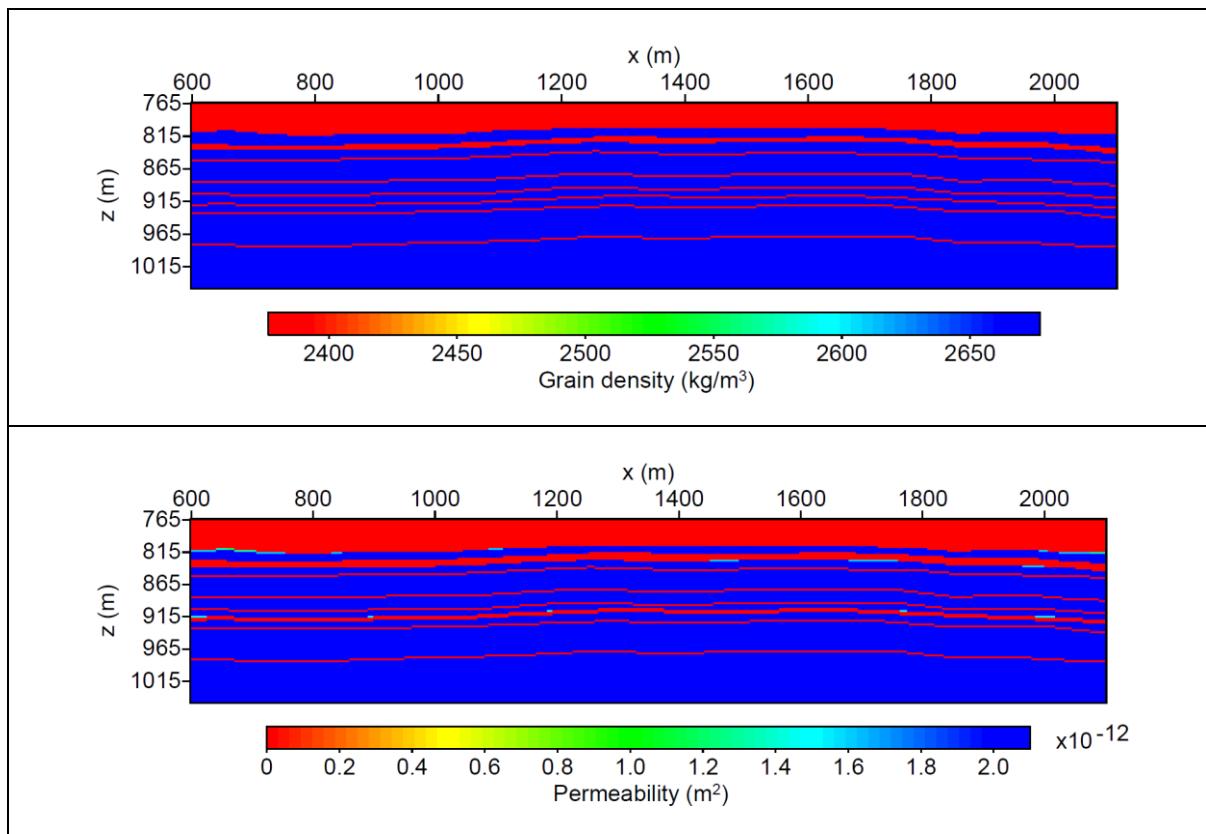
Figure 5-5. The derived new a priori rock properties. From top to bottom: frame bulk modulus, frame shear modulus, grain bulk modulus, porosity, grain density and permeability.

5.2 Estimation of CO₂ saturation

After deriving the a priori frame properties, we use the same P-wave velocity input for the rock physic inversion. We use a central frequency of 30 Hz and a NA iteration number of 400.

Figure 5-6 shows the estimation results when we use a Brie rock physics model with a Brie exponent e equal to 5 (Carcione and Picotti, 2006). The CO_2 saturation is high from 60% to 90% in central plume. CO_2 saturation is about 20% - 30% outside of the main plume. It is worth noting that the uncertainty in our estimation results is absolute value. The related uncertainty of CO_2 saturation is ranging from 0.15 to 0.25. This means that the saturation is known with $\pm$ 0.15 to 0.25 i.e. between 35 to 100% S_{CO2}.
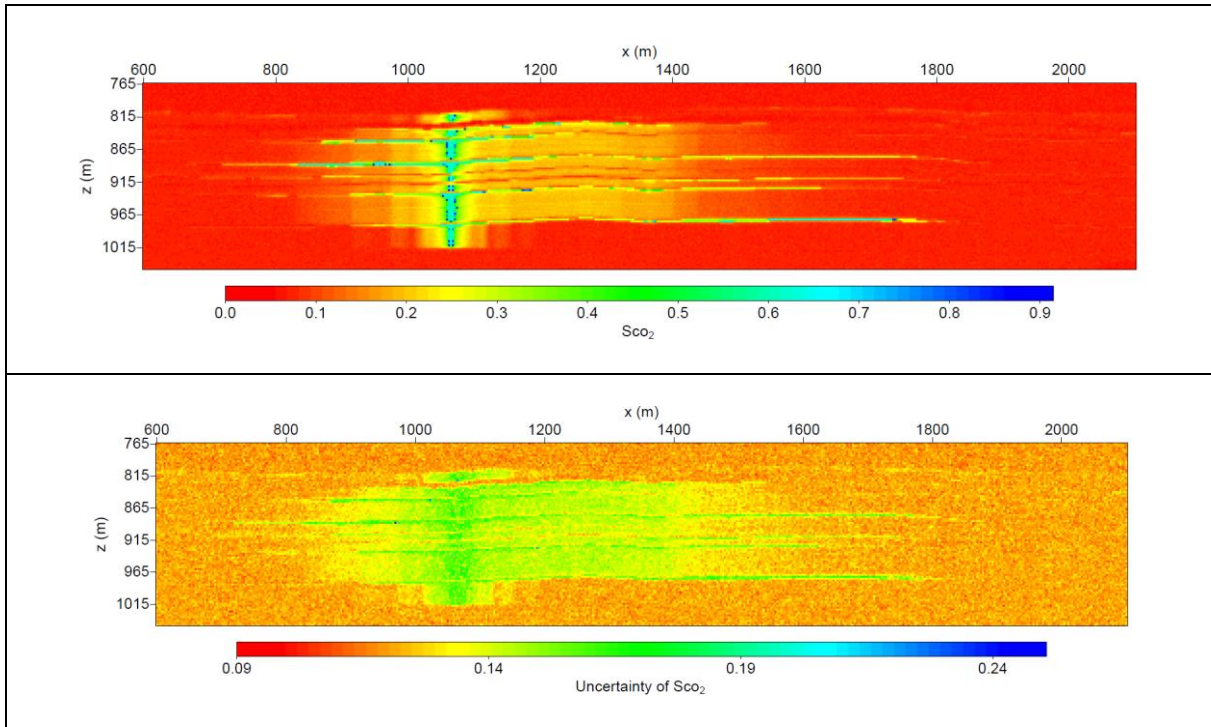
Figure 5-6. Estimation of CO₂ saturation (top panel) and uncertainty of CO₂ saturation (bottom panel) using Brie rock physics model with e = 5.

Figure 5-7 shows the estimation results when we use a Brie rock physics model to invert CO_2 saturation and Brie exponent e simultaneously. The estimated CO_2 saturation is higher and the related uncertainty of CO_2 saturation is also higher. The Brie exponent e varies from 6 to 16 for CO_2 saturated layers, while for the Brie exponent can be quite high to around 35 for the CO_2 plume, suggesting uniform saturation distribution. The uncertainty of Brie exponent is around 6 – 10.
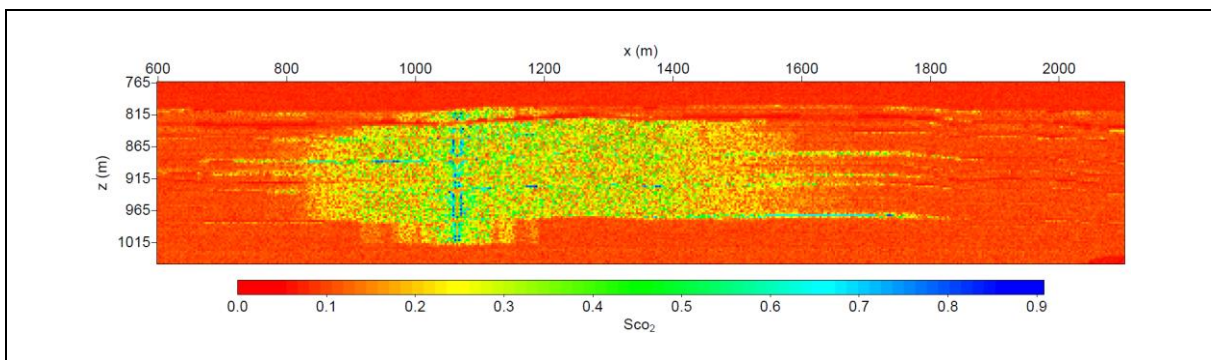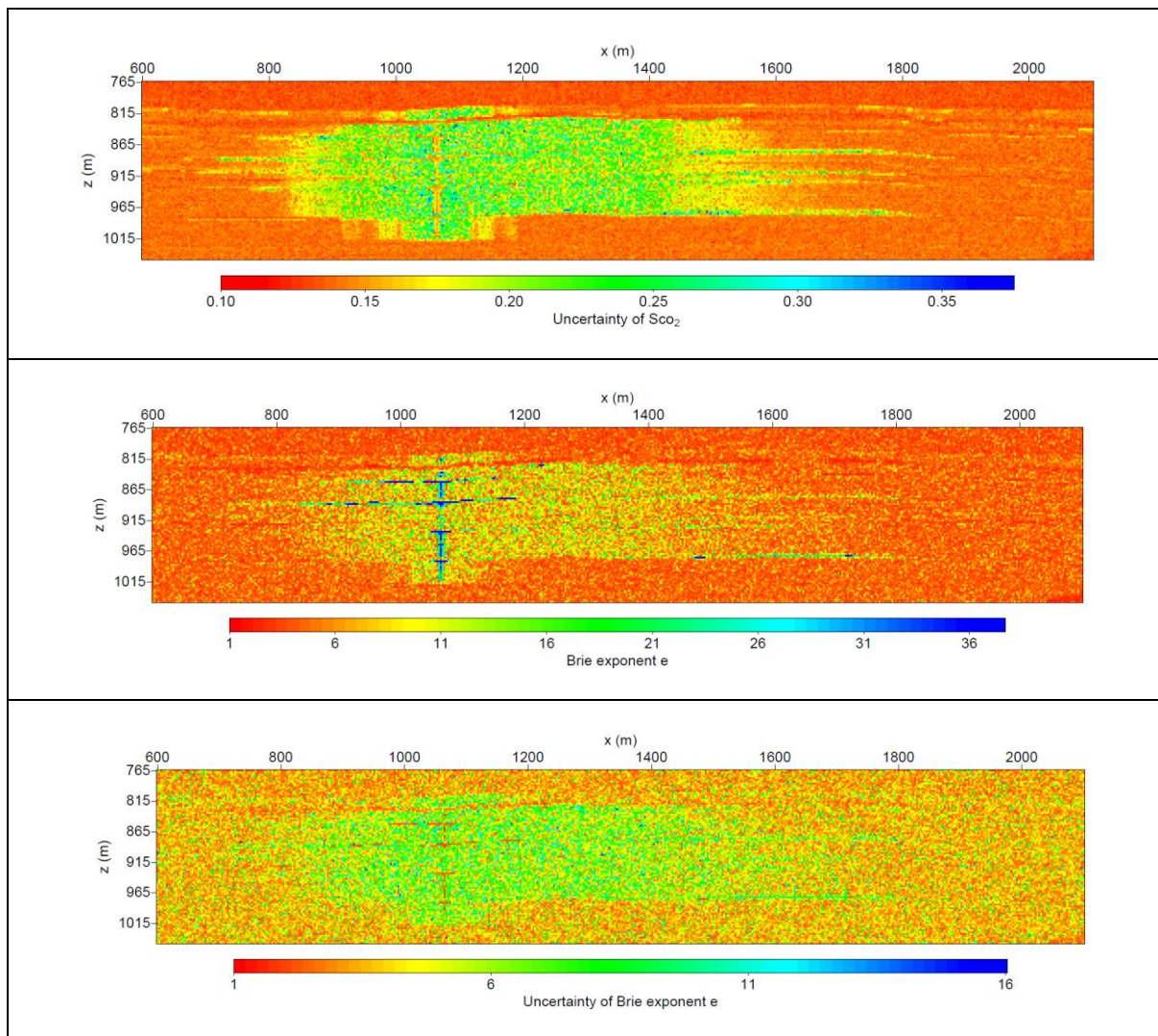
Figure 5-7. From top to bottom: estimation of CO_2 saturation, uncertainty of CO_2 saturation, estimation of Brie exponent, and uncertainty of Brie exponent using Brie rock physics model with e inverted.

Figure 5-8 and Figure 5-9 show the estimation results when we use a Brie rock physics model to invert CO_2 saturation and CO_2 properties (CO_2 bulk modulus, density, and viscosity) simultaneously. The estimated CO_2 saturation is similar with the case when CO_2 properties are defined. The estimated CO_2 bulk modulus is around 0.05 - 0.06 GPa with an uncertainty around 0.01 - 0.02 GPa for the central plume. The estimated CO_2 density is around 700 - 800 kg/m^3 with an uncertainty around 30 - 50 kg/m^3 for the central plume. The viscosity of CO_2 is hard to be inverted using P-wave velocity only as we concluded in the sensitivity tests. Therefore, the related figures for CO_2 viscosity in 2D are not shown here for brevity. It could be explained using the sensitivity results in Figure 5-10 (Yan, 2016). We can see that S_W is well estimated even when the CO_2 properties are not defined using only V_P. The CO_2 properties cannot be well estimated using only V_P as an input. There are several local minima and K_{CO2} cannot converge

29

towards the true model. K_{CO2} and ρ_{CO2} can be better estimated when V_S is added (Dupuy et al., 2017; Yan, 2016). Quality factor Q_P is also important to reduce uncertainty. More details are provided in Yan (2016).
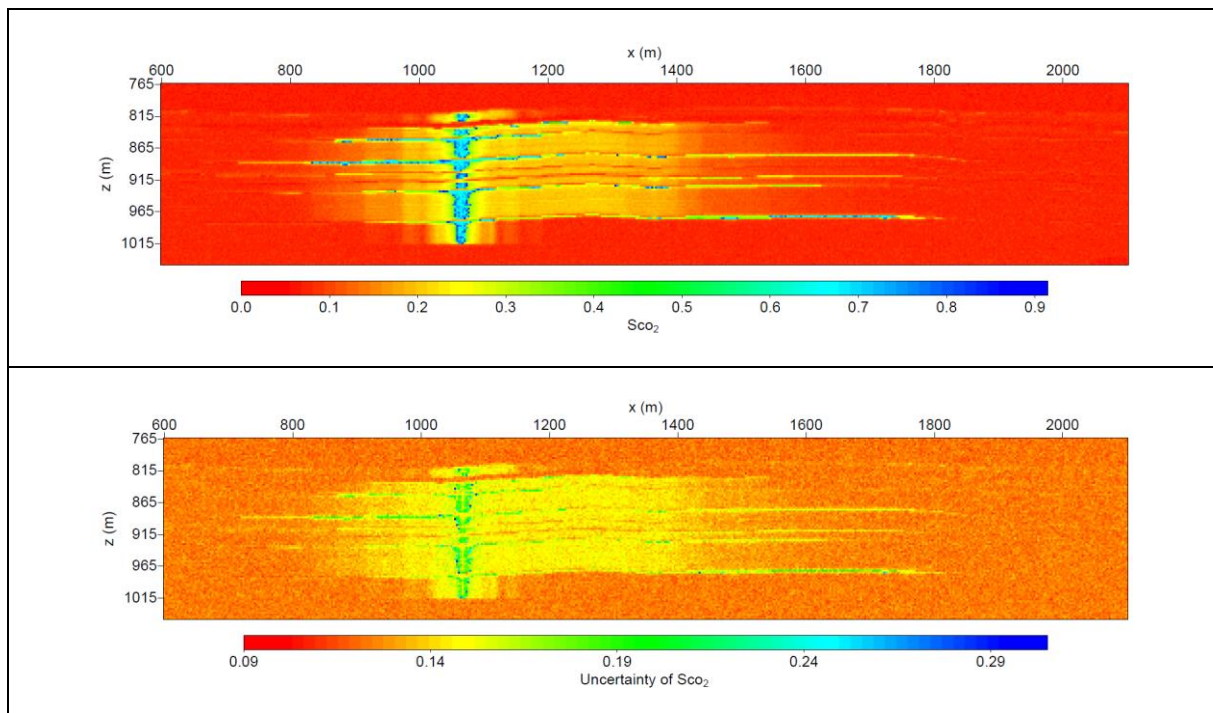
Figure 5-8. Estimation of CO₂ saturation (top panel) and uncertainty of CO₂ saturation (bottom panel) using Brie rock physics model (e = 5) with CO₂ properties inverted.
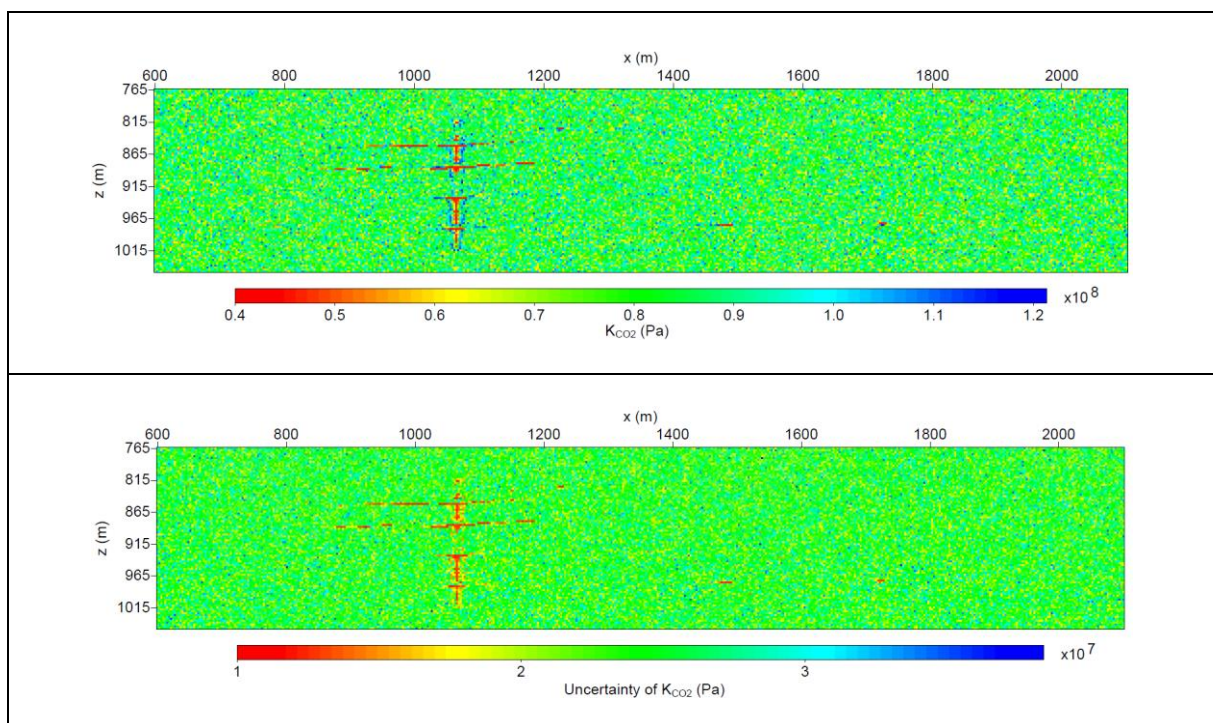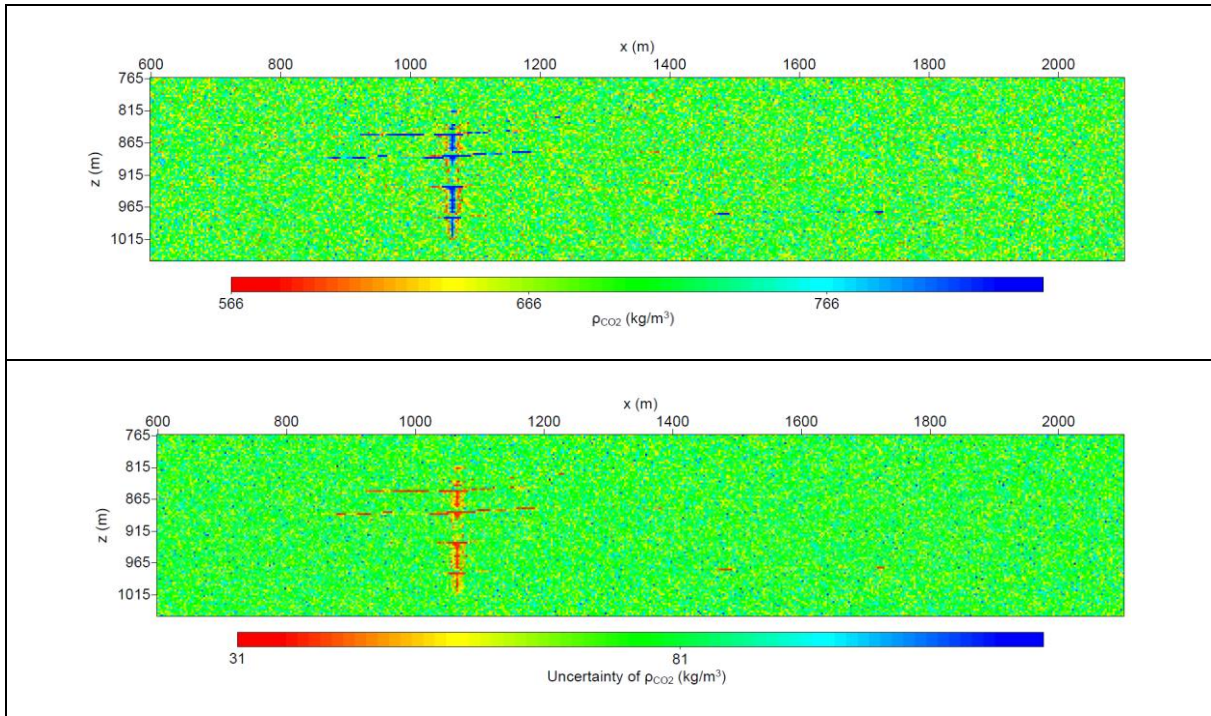
Figure 5-9. From top to bottom: estimation of CO$_2$ bulk modulus, uncertainty of CO$_2$ bulk modulus, estimation of CO$_2$ density, and uncertainty of CO$_2$ density using Brie rock physics model (e = 5) with CO$_2$ properties inverted.
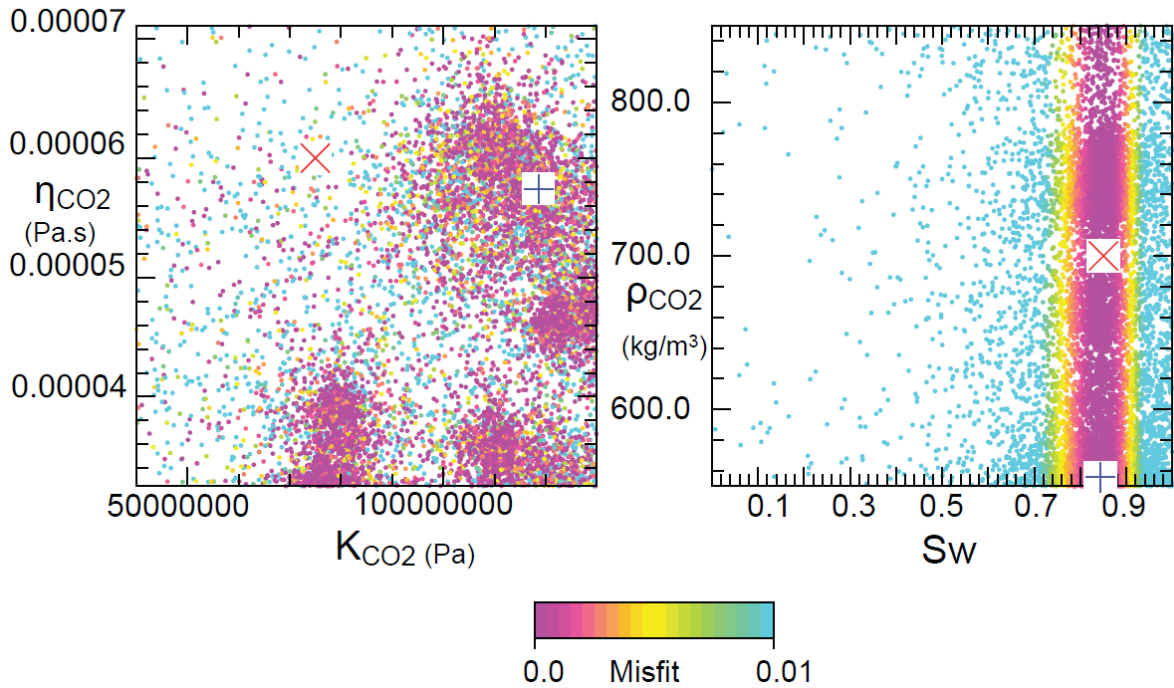
Figure 5-10. Uniform saturation condition (true model S$_W$ = 85%): inversion of CO$_2$ density, CO$_2$ bulk modulus, CO$_2$ viscosity and brine saturation from V$_P$. The blue cross indicates the best model; red cross indicates the true model.

We also conducted the tests for fully patchy mixing with e = 1 (Figure 5-11) and fully uniform mixing with e = 40 (Figure 5-13), and the case with e = 3 (Figure 5-12) (Brie et al., 1995). When e = 1, the Brie rock physics model gives the highest estimation of CO_2 saturation. While the estimation using e = 40 is with a high uncertainty up to 0.4. This can be explained using Figure 2-2 that the P-wave velocity is less sensitive to the change of saturation when brine saturation is low. The estimation results using e = 3 is similar with that using e = 5.
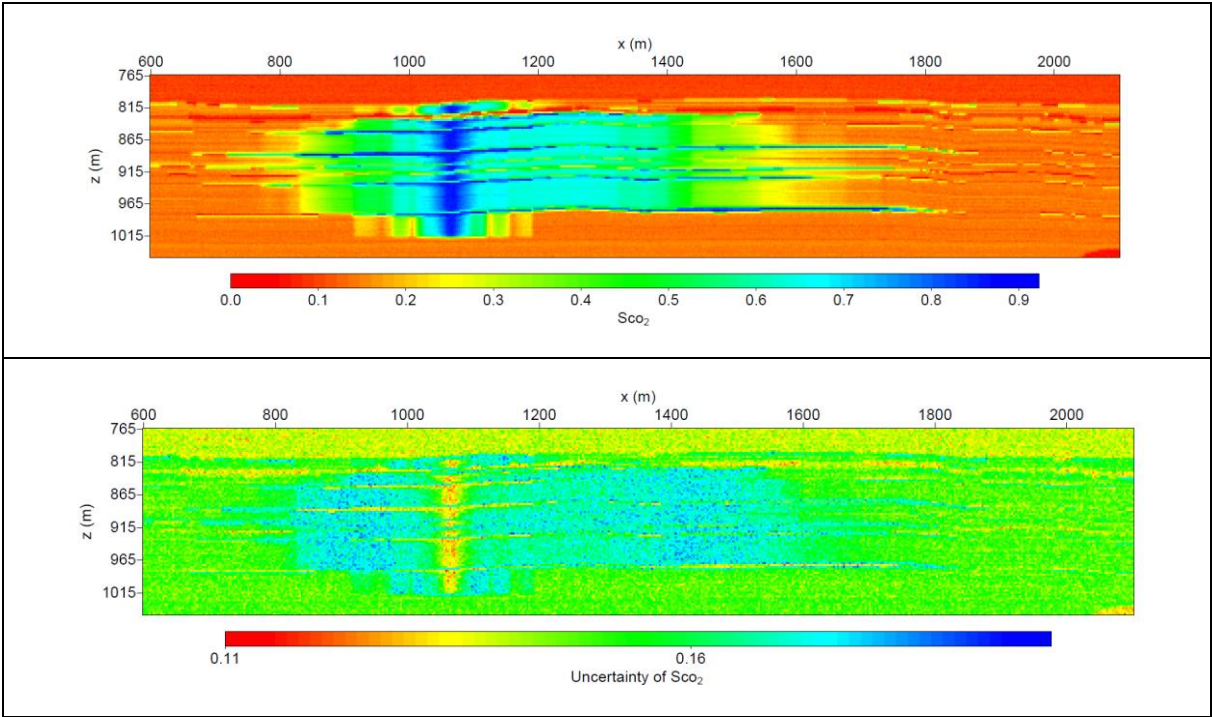
Figure 5-11. Estimation of CO_2 saturation (top panel) and uncertainty of CO_2 saturation (bottom panel) using Brie rock physics model with e = 1.
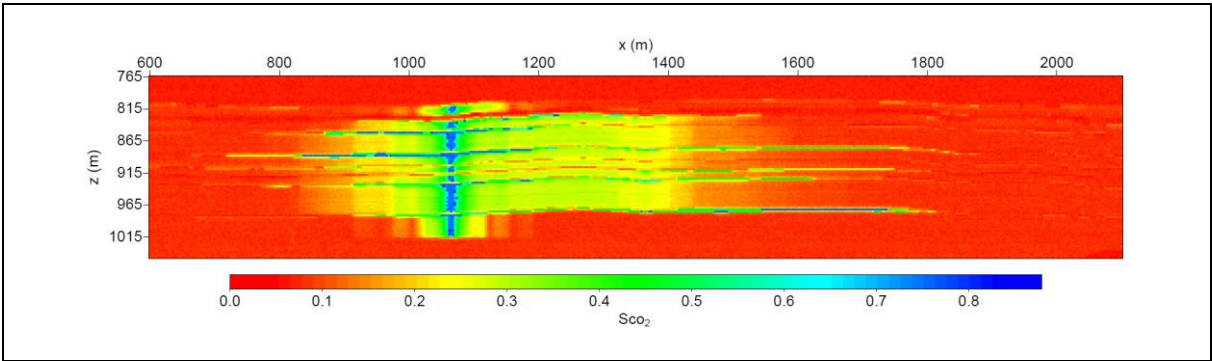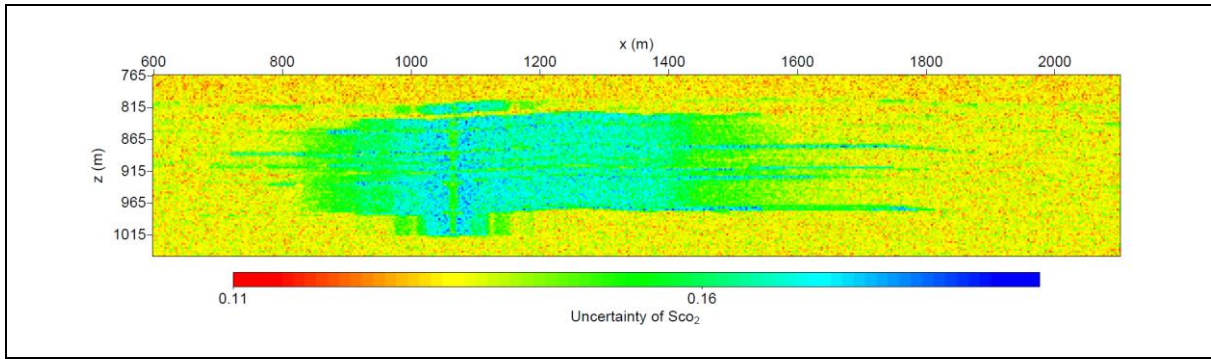
Figure 5-12. Estimation of CO_2 saturation (top panel) and uncertainty of CO_2 saturation (bottom panel) using Brie rock physics model with e = 3.
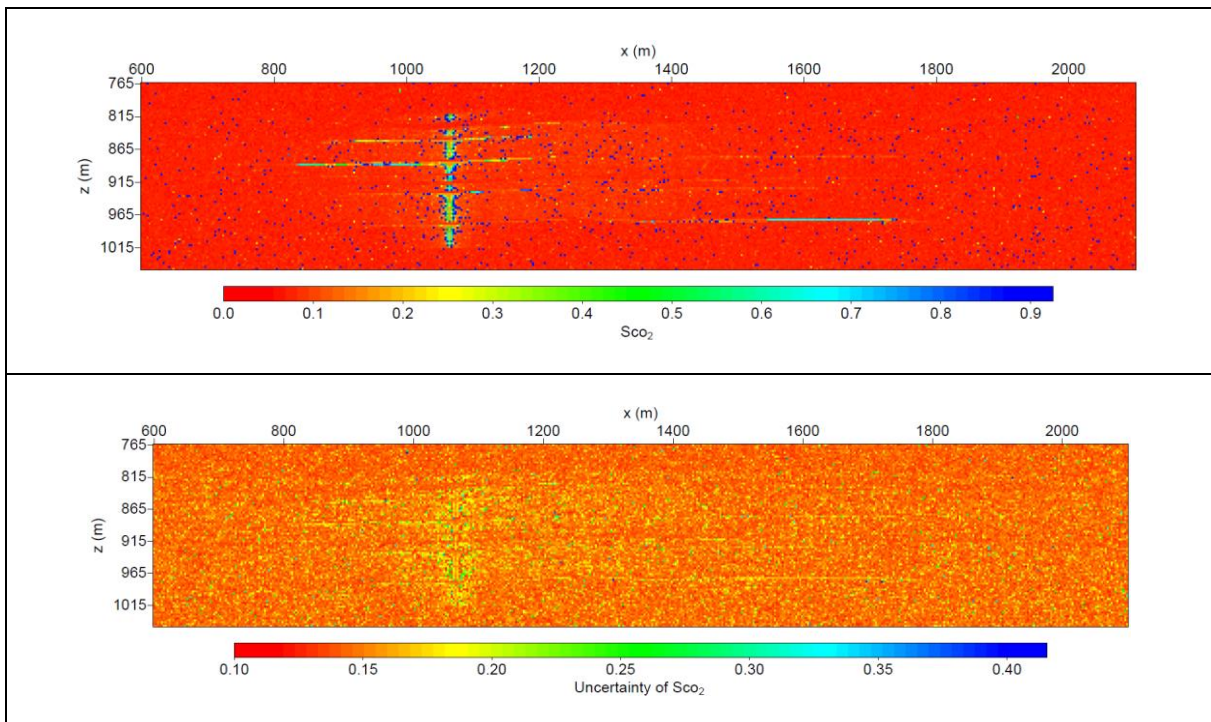
Figure 5-13. Estimation of CO_2 saturation (top panel) and uncertainty of CO_2 saturation (bottom panel) using Brie rock physics model with e = 40.

Figure 5-14 shows the estimation results when we use patchy saturation model. The estimated CO_2 saturation is ranging from 0% to 17% with $\pm$ 0.02 to 0.035 uncertainty. Due to the limitation related to the validity range of saturation, the results are not meaningful and, therefore, we do not show this model for the later application on FWI synthetic model.

We also give a 1D view analysis at x = 1062 m to better visualize the estimation results. The selected trace through the main CO_2 plume. The estimation of CO_2 saturation is given in Figure 5-15 and the jointly estimated other properties are given in Figure 5-16.

Figure 5-14. Estimation of CO₂ saturation (top panel) and uncertainty of CO₂ saturation (bottom panel) using a patchy saturation with *a* = 0.01 m.
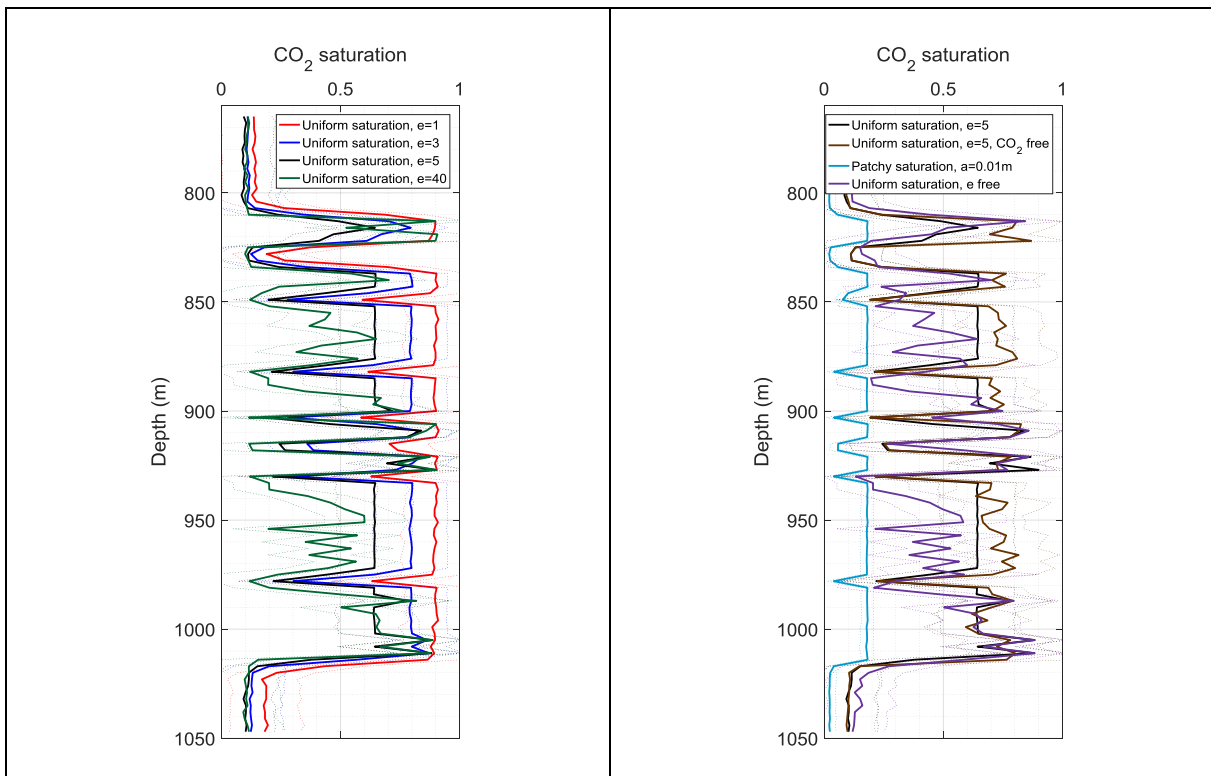
Figure 5-15. 1D estimation of CO₂ saturation using Brie rock physics model with different Brie exponent (left panel) and 1D estimation of CO₂ saturation using different rock physics models (right panel) for x = 1062 m. The dotted lines correspond to the mean value of estimation plus/minus uncertainty.
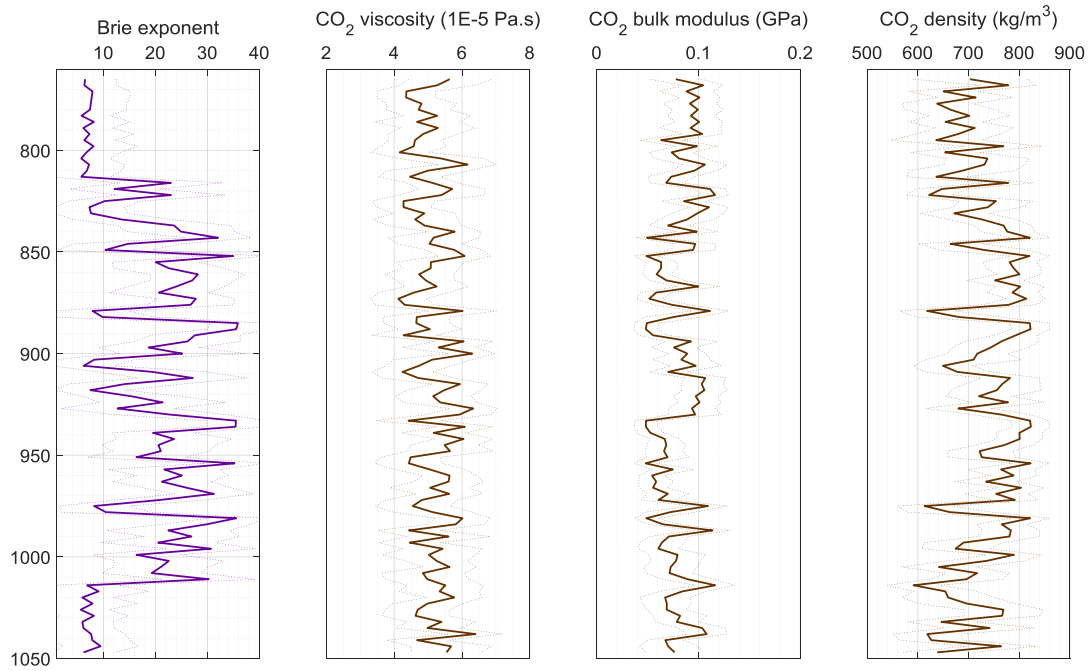
Figure 5-16. From left to right: 1D profile of Brie exponent and other CO₂ properties results (CO₂ viscosity, CO₂ bulk modulus, and CO₂ density) inverted jointly with the CO₂ saturation using different rock physics models for x = 1062 m. The dotted lines correspond to the mean value of estimation plus/minus uncertainty.

6   FWI SYNTHETIC MODEL

In this part of study, we apply the rock physics inversion tool on the synthetic Sleipner data using the results derived from FWI. The goal is to test and demonstrate the validity and efficiency of the proposed rock physics tool prior to the application of the real data set in 2008.

6.1   Data preparation and FWI tests

We start the FWI with a smooth starting model as shown in Figure 6-1. The warm colour region in the central is related to the layers with a low P-wave velocity ranging from 1700 m/s to 1800 m/s. This low-velocity anomaly spot is indicating the CO_2 saturated layers.
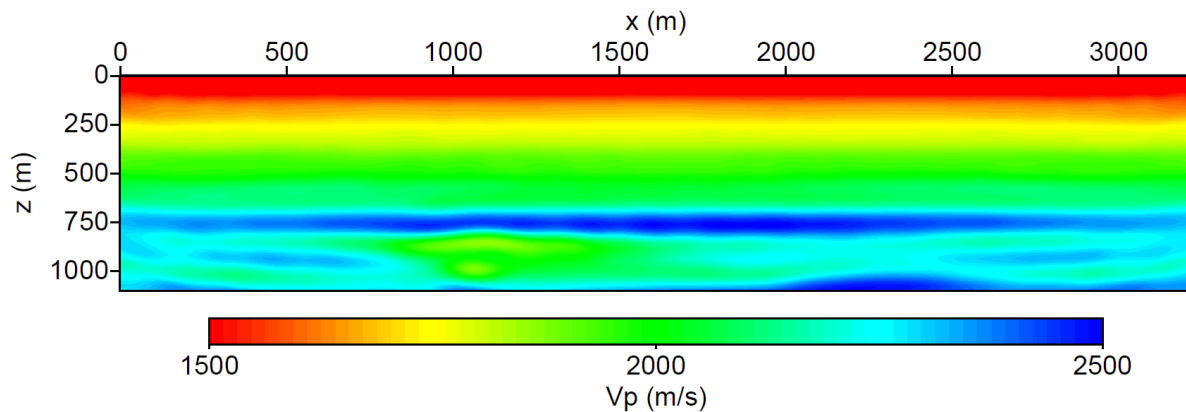
Figure 6-1. Starting model of P-wave velocities before FWI.

We run different FWI tests and generate different V_P results. Figure 6-2 shows the P- wave results derived using different FWI processes. We are using a preconditioned-gradient technique jointed FWI tomographic method. We conduct the FWI process in different ways to obtain the best P- wave results. First, we detect the smoothing factor effects on the P- wave results (as shown in panel (a), (b), (c), (d) in Figure 6-2). The P- wave velocity models derived from in FWI tests 1 and 3 show the effect due to a different value of x-direction smoothing factor. The higher smoothing factor (0.8) in x-direction will slightly increase the P-wave velocity results but does not affect the discrimination of layers (as shown in panel (a), (c) in Figure 6-2). In contrast, the P-wave velocity derived in FWI tests 2 and 4 show the effect due to a different value of z-direction smoothing factor. The z-direction smoothing factor has a strong effect on the vertical resolution. An improper selection of the z-direction smoothing factor will smear the layers and geological variation in depth (as shown in panel (b), (d) in Figure 6-2). Therefore, a z-direction smoothing factor of 0.2 and a relative small z-direction smoothing factor of 0.1 are

36

favourable in our case. In addition, the P-wave velocity results using a FWI without smoothing show many artefacts (panel (e) in Figure 6-2). The velocity in the layers is not laterally constant in this area and cannot be distinguished from each other (panel (e) in Figure 6-2). The last FWI test (panel (f) in Figure 6-2) is designed with estimating the Hessian operator at each iteration step and with a very small damping factor for the Hessian operator (1×10^{-8}). With this more time-consuming computation of the Hessian, the P-wave velocity is better defined and the deeper layers in the reservoir (panel (f) in Figure 6-2) are well reconstructed. The different setting parameters for different FWI tests are described in Table 6-1. More details of the FWI setting parameters are given in Appendix B.

Table 6-1. Different parameter settings for FWI tests.

Parameter	Value for test 1	Value for test 2	Value for test 3	Value for test 4	Value for test 5	Value for test 6
Damping coefficient of Hessian	0.001	0.001	0.001	0.001	0.001	1.00×10^{-8}
Smooth method	Gaussian spatial smoothing	Gaussian spatial smoothing	Gaussian spatial smoothing	Gaussian spatial smoothing	No smoothing	Gaussian spatial smoothing
Wavelength fraction along x	0.2	0.2	0.5	0.2	0	0.2
Wavelength fraction along z	0.1	0.8	0.1	0.5	0	0.2
Estimated Hessian at each iteration	No	No	No	No	No	Yes

We can distinguish approximately 8 CO_2 injected layers from the FWI derived P-wave velocity. With the considering of the higher resolution on layers saturated with CO_2, the full inversion

results of test 6 is used as the input for the rock physics inversion. To save the computational cost in the process of application on the rock physics inversion, we focus on a region of interest with CO_2 saturated. The 1D P-wave velocity profiles for selected region of different FWI tests (Figure 6-3) are extracted to illustrate the velocity variation for each FWI test.
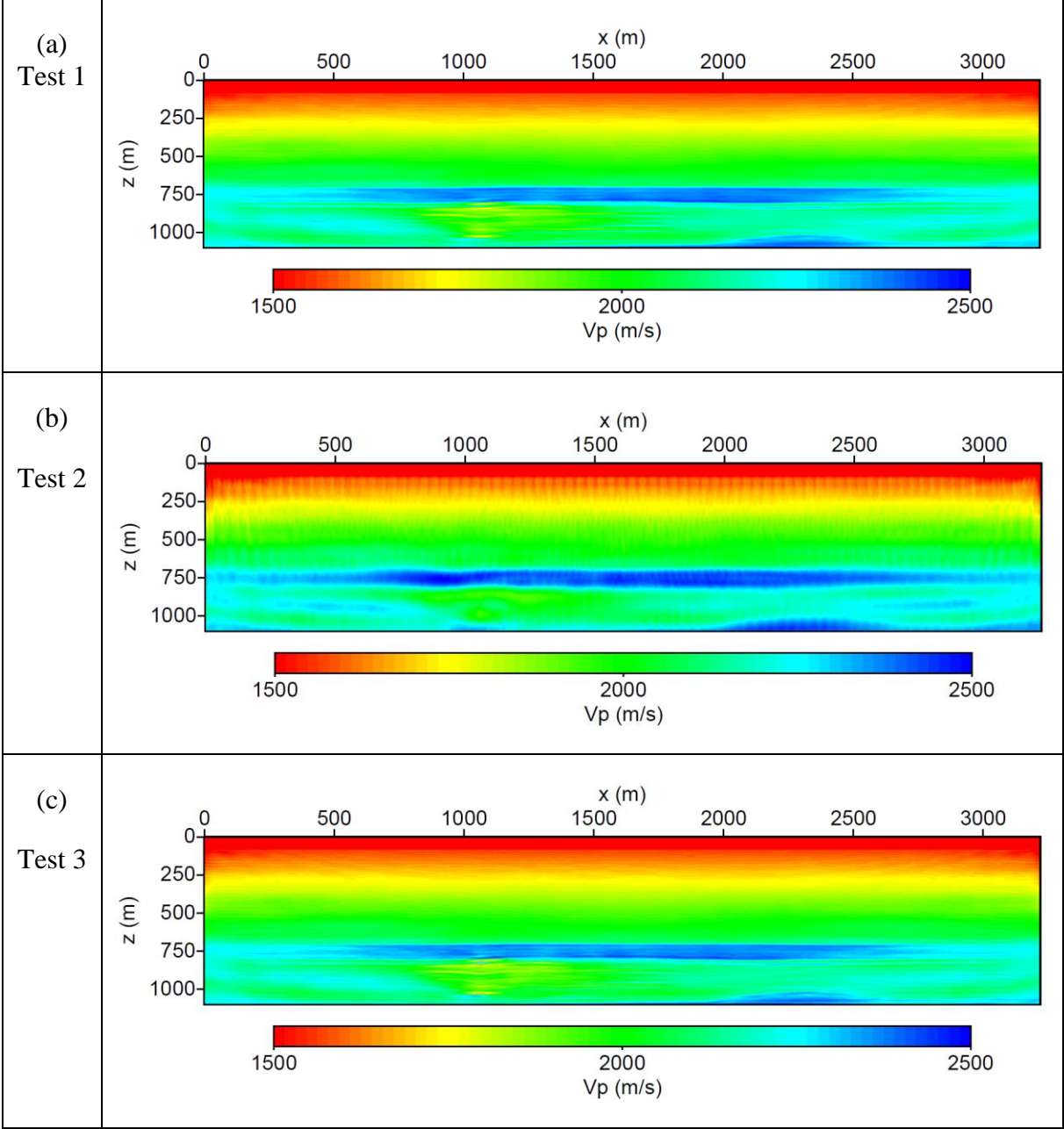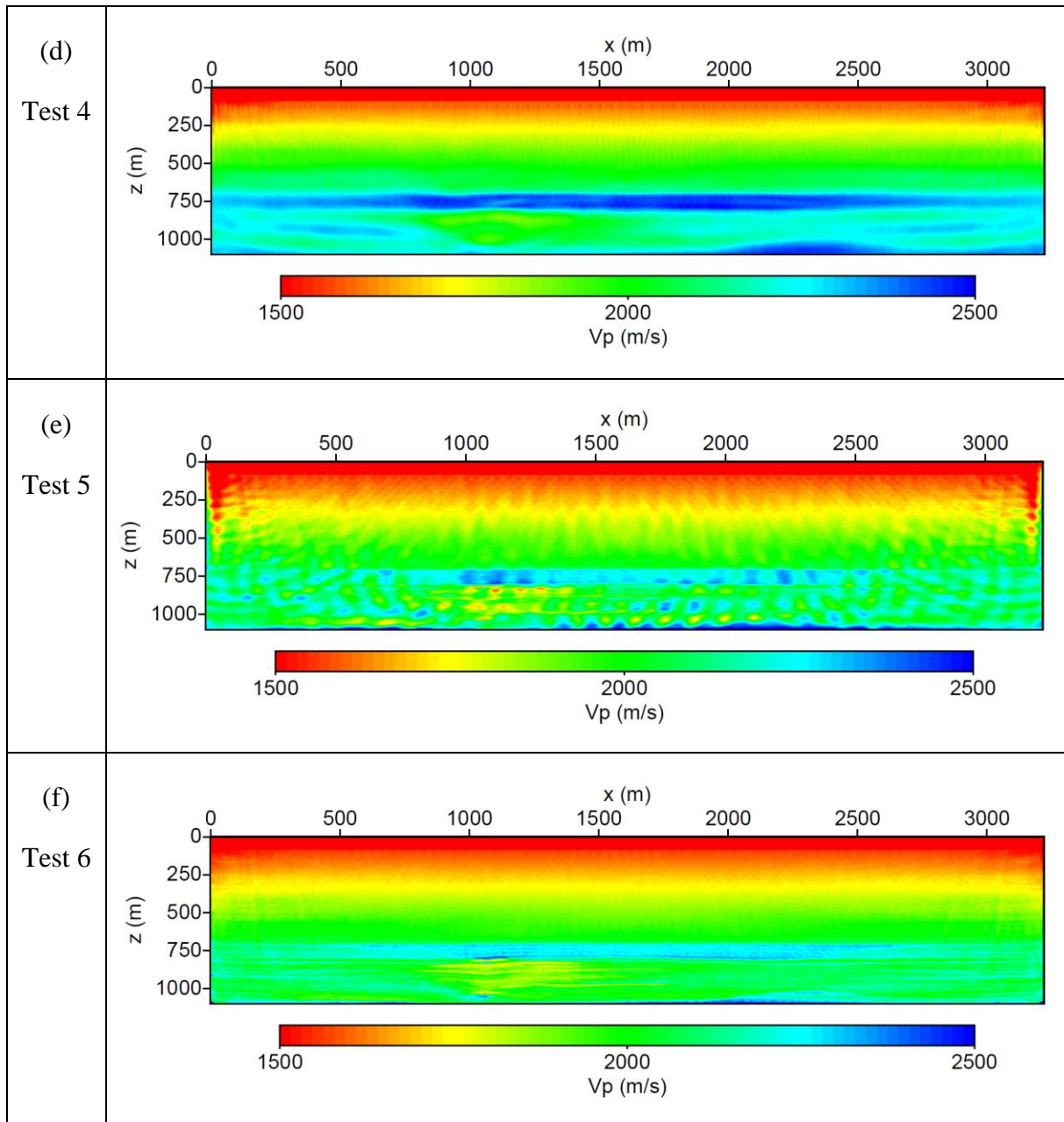
Figure 6-2. P-wave velocities after various FWI tests.
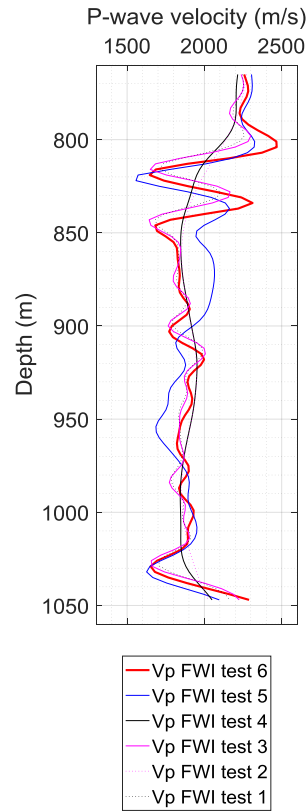
P-wave velocity (m/s)

Figure 6-3. P-wave velocity for different FWI tests at x = 1062 m.

Figure 6-4 shows the selected region of FWI test 6 at depths from 765 m to 1047 m. For a priori rock physics parameters, we use true model derived frame moduli as described in previous chapter (Figure 6-5).
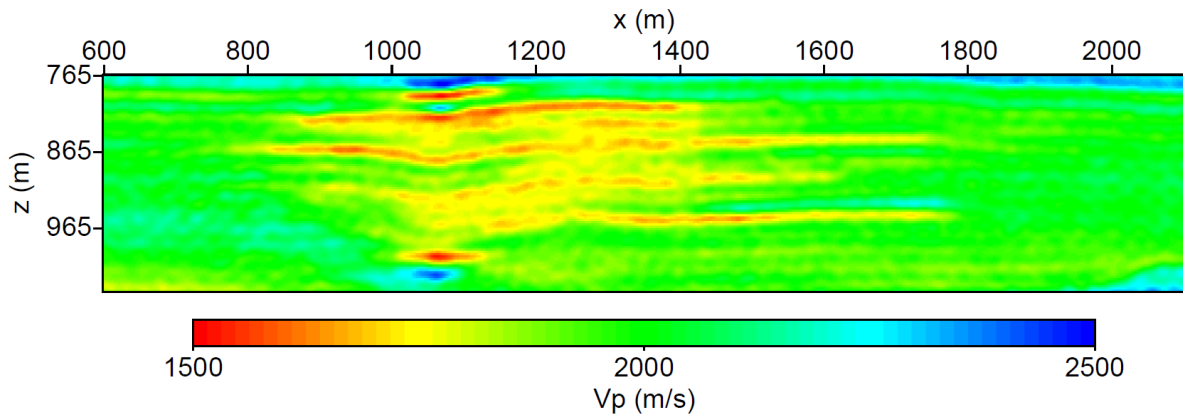
Figure 6-4. P-wave velocity model extracted for the target region from FWI test 6.

40
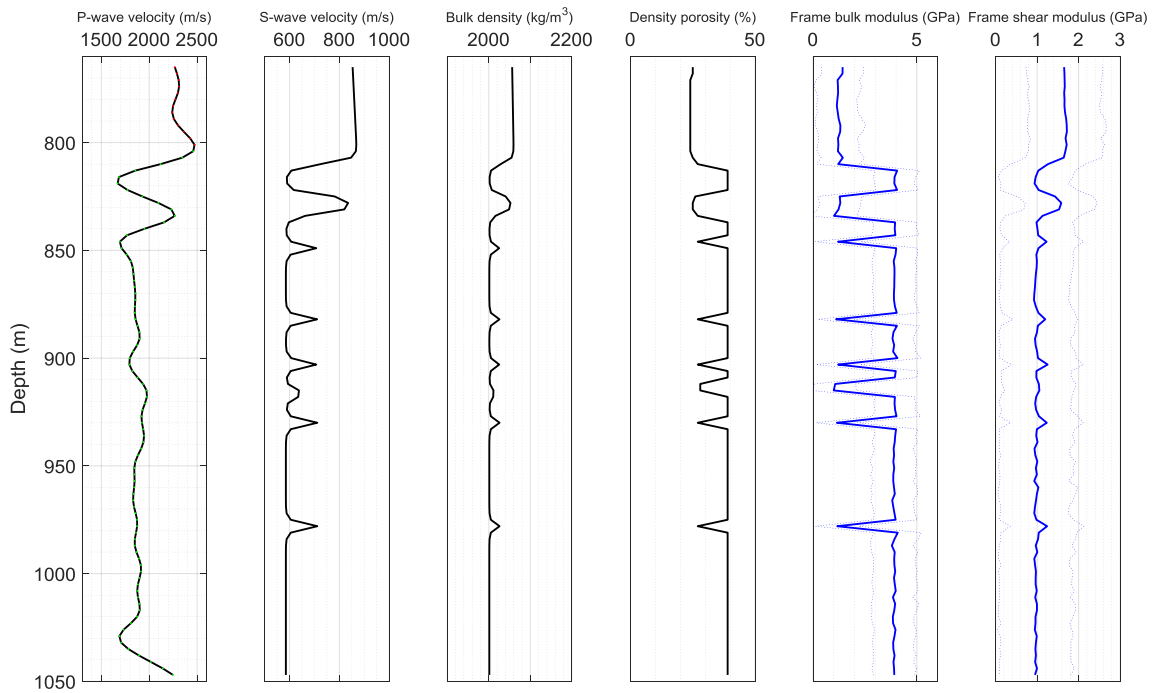
Figure 6-5. From left to right: P-wave velocity of FWI test 6, S-wave velocity, bulk density, density porosity, frame bulk modulus, frame shear modulus at x = 1077 m. The red dots indicate the Nordland caprock shale, and the green dots indicates the Utsira sandstone. The frame moduli (blue lines) are inverted using rock physics inversion for true synthetic model with plus/minus related uncertainty (dotted blue lines).

6.2 Estimation of CO_2 saturation

In this section, we present the estimation results using different rock physics models with a maximum misfit of 0.1 and the corresponding uncertainty. We use a central frequency of 30 Hz and a NA iteration number of 400.

Figure 6-6 shows the CO_2 saturation is ranging from 0.1 to 0.3 $\pm$ 0.1 to 0.15, i.e. between 0 and 0.45 (0 to 45% SCO_2). This is lower than that using the true synthetic model. The reason for this low CO_2 saturation estimation could be the overestimated velocity from FWI.

41
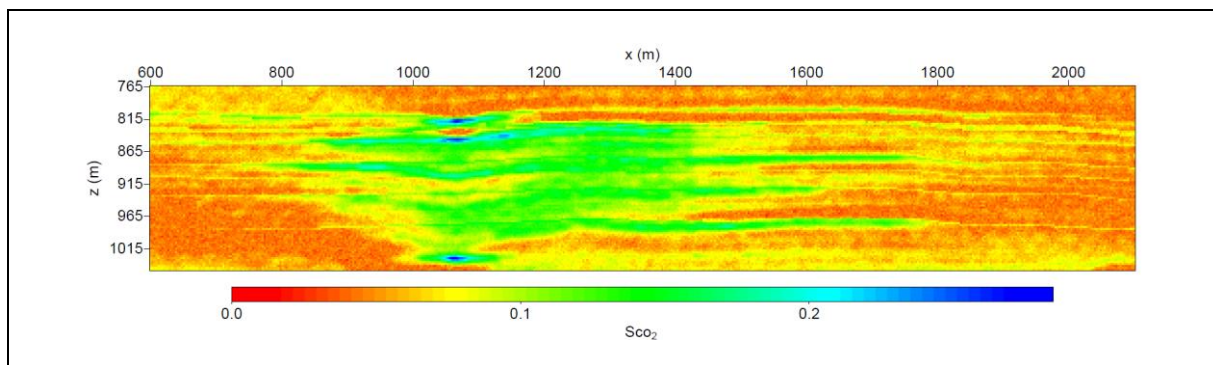
**Figure 6-6. Estimation of CO_2 saturation (top panel) and uncertainty of CO_2 saturation (bottom panel) using Brie rock physics model with e = 5.**

Figure 6-7 shows the estimation results when we use a Brie rock physics model to invert CO_2 saturation and Brie exponent e together. The estimated CO_2 saturation ranges from 20% - 65% with an uncertainty of 0.20 to 0.36, which is higher than using e = 5. The Brie exponent e varies from 8 to 32 with an uncertainty of 5 to 16 for CO_2 saturated layers in general, which indicates the mixture is between a fully patchy mixing and uniform mixing distribution.
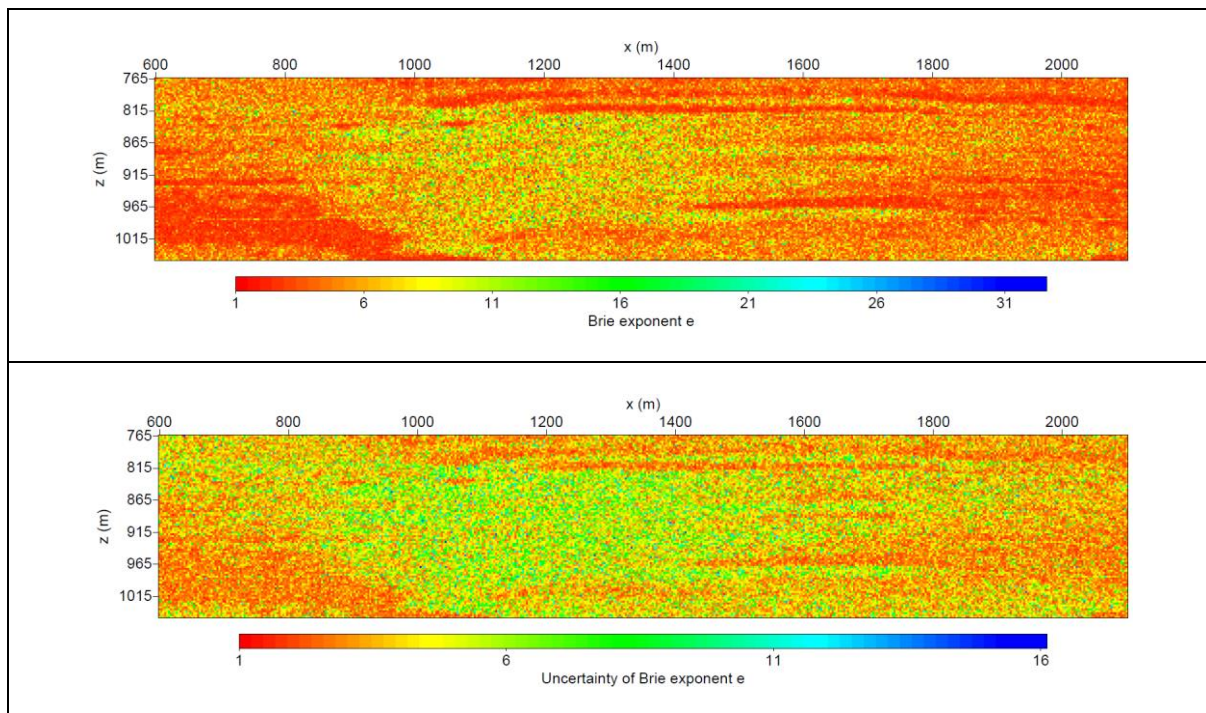
Figure 6-7. From top to bottom: estimation of CO_2 saturation, uncertainty of CO_2 saturation, estimation of Brie exponent, and uncertainty of Brie exponent using Brie rock physics model with Brie exponent e inverted.

Figure 6-8 shows the estimation results when we use a Brie rock physics model with e = 5 to invert CO_2 saturation and other CO_2 properties (CO_2 bulk modulus, CO_2 density, and viscosity) simultaneously. The estimated CO_2 saturation are similar with that when the CO_2 properties are defined. The results of CO_2 bulk modulus and density are not as good as that for the case of true synthetic model. One possible reason is that the true synthetic model is a more favourable case with clear thin layers. The viscosity of CO_2 is also hard to be inverted using only P-wave velocity. The related figures for CO_2 viscosity in 2D are not shown here for brevity.
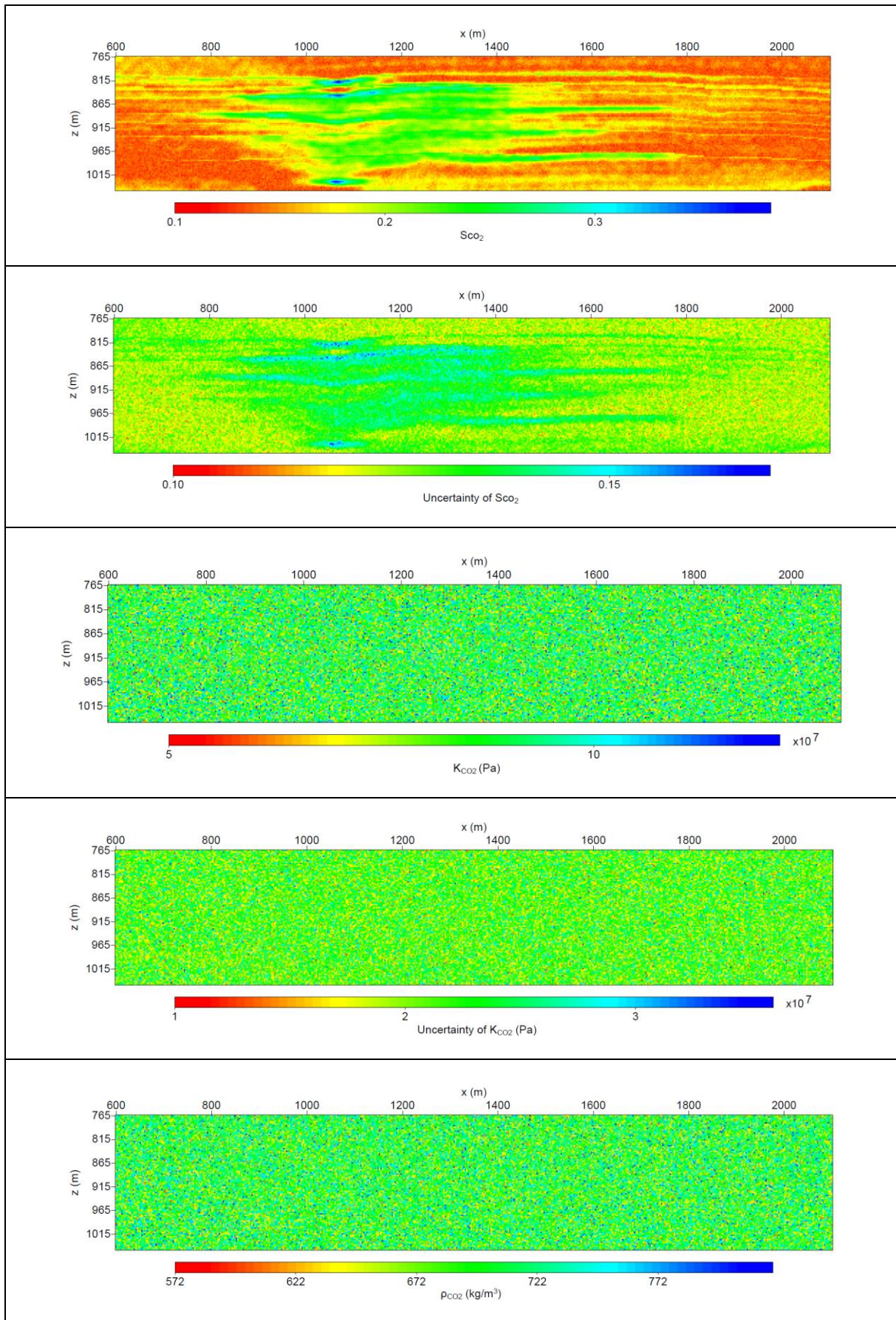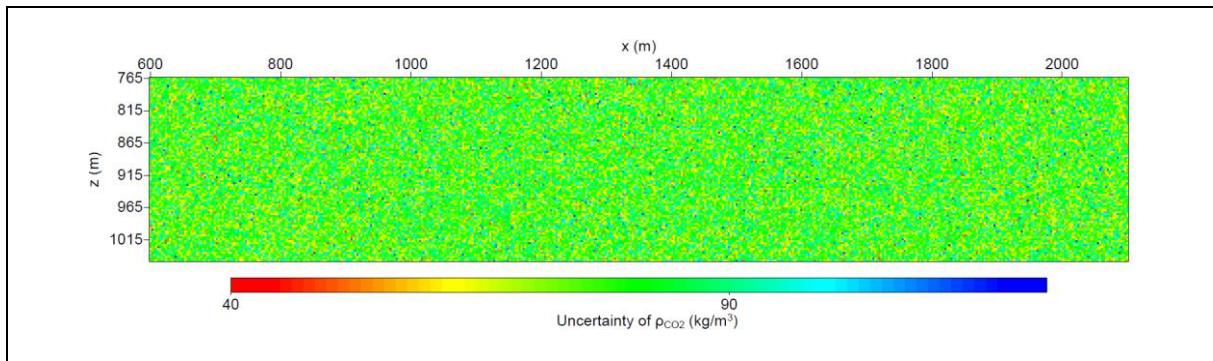
Figure 6-8. From top to bottom: estimation of CO₂ saturation, uncertainty of CO₂ saturation, estimation of CO₂ bulk modulus, uncertainty of CO₂ bulk modulus, estimation of CO₂ denisty, and uncertainty of CO₂ denisty using Brie rock physics model (e = 5) with other CO₂ properties inverted.

We also conducted the Brie rock physics model tests for fully patchy mixing with e = 1 (Figure 6-9) and fully uniform mixing with e = 40 (Figure 6-11), and the case with e = 3 (Figure 6-10) (Brie et al., 1995). The highest saturations for the Brie rock physics model with e = 1, 3 and 40 are known with 82% ± 0.2 uncertainty, 53% ± 0.2 uncertainty, and 92% ± 0.41 uncertainty, respectively. When e = 1, the Brie rock physics model shows the highest amount of CO₂. While the Brie rock physics model with e = 40 does not show the CO₂ saturated layers and has a high uncertainty up to 0.4. It could be due to the P-wave velocity is less changeable when brine saturation is ranging from 0% to 90% for the Brie rock physics model with e = 40 (Figure 2-2). The estimation results using e = 3 is similar with that using e = 5.

For the 2D synthetic data, we also extract the results and the input data at x = 1062 m, where we can observe through the injection point and the above accumulation layers of carbon dioxide. The estimation of CO₂ saturation is given in Figure 6-12 and the jointly estimated other properties are given in Figure 6-13.
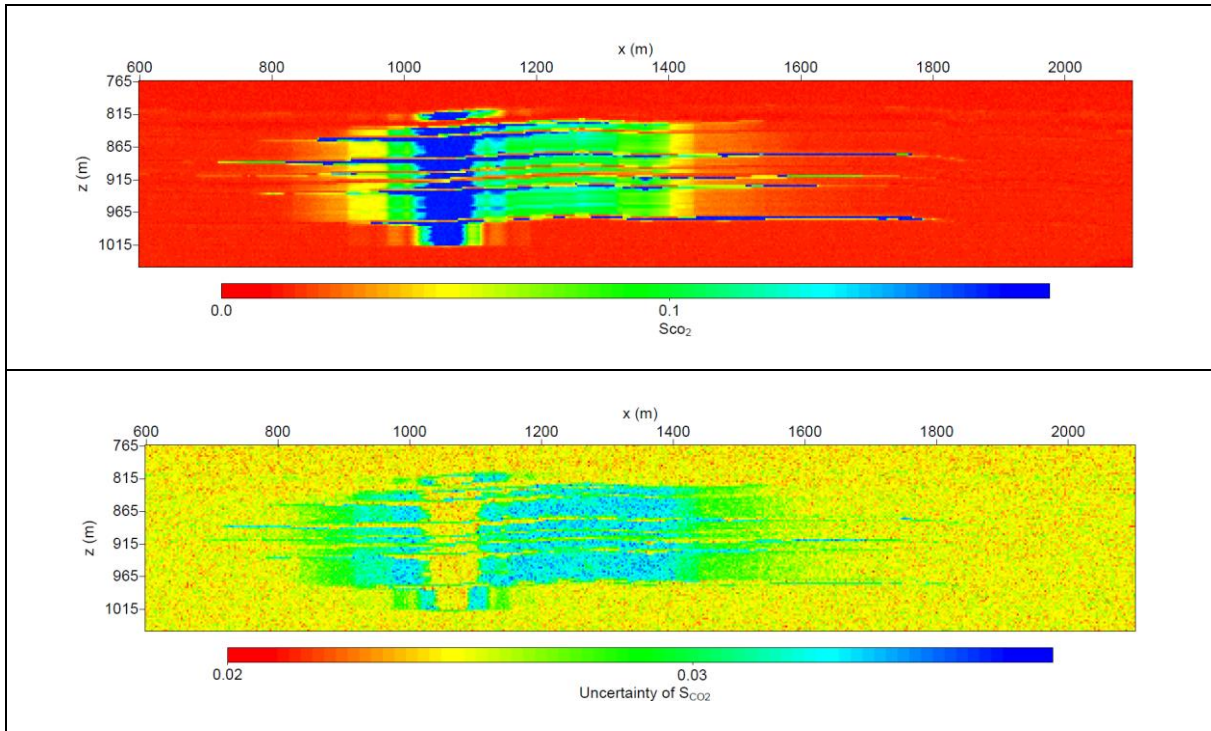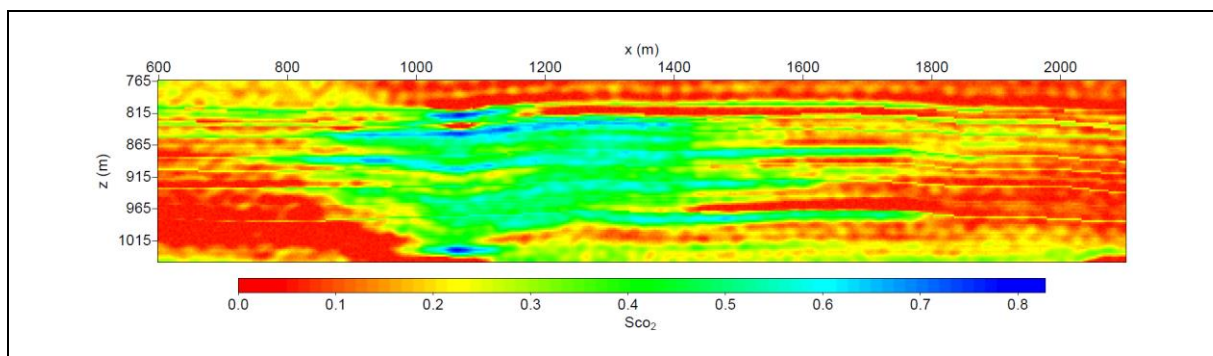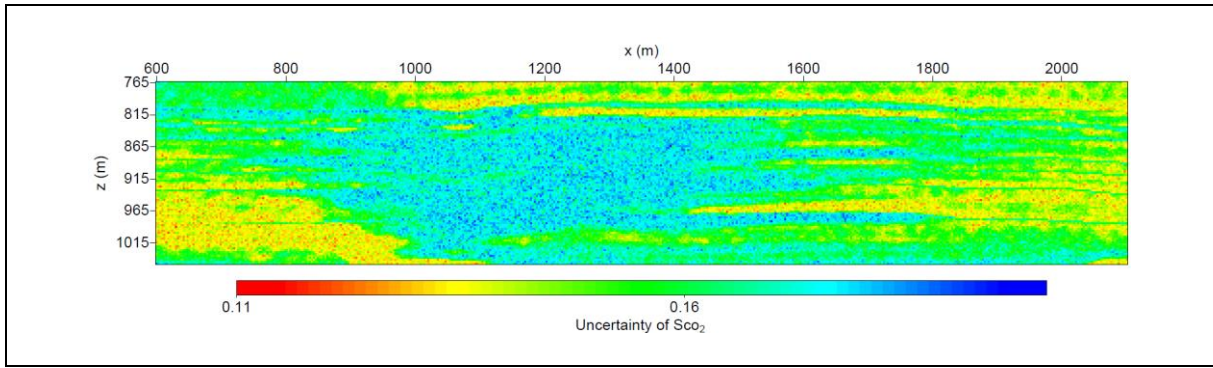
Figure 6-9. Estimation of CO₂ saturation (top panel) and uncertainty of CO₂ saturation (bottom panel) using Brie rock physics model with e = 1.
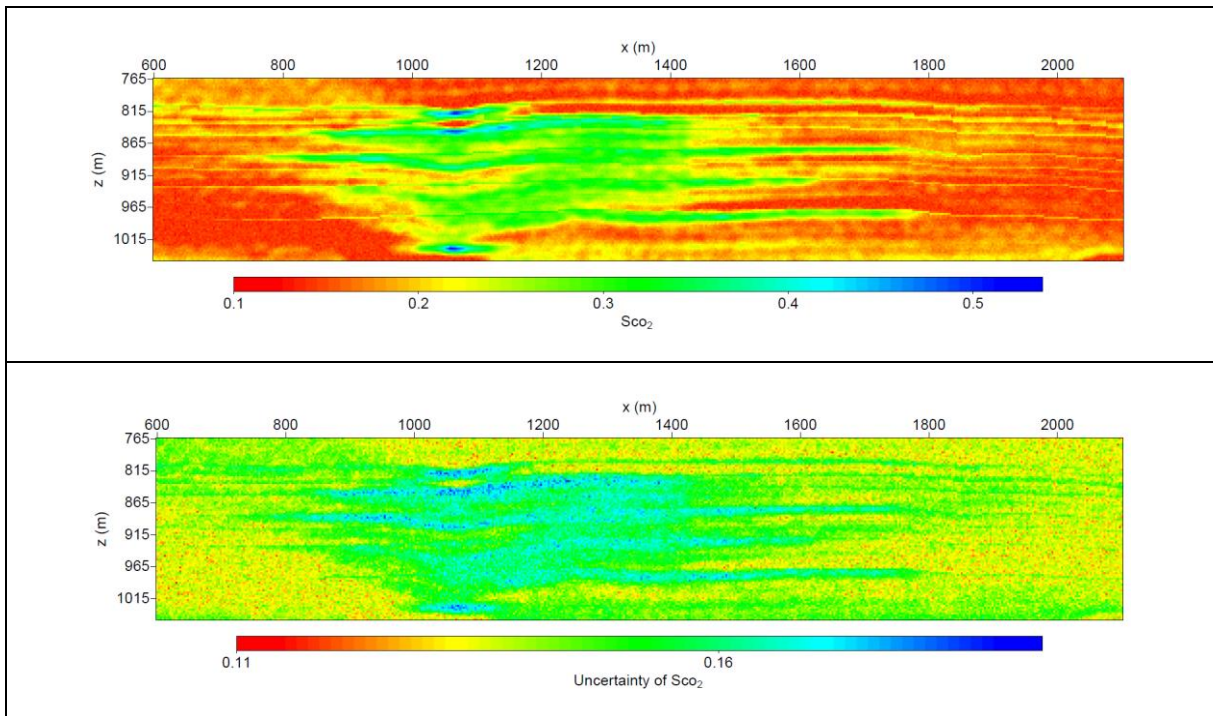
Figure 6-10. Estimation of CO₂ saturation (top panel) and uncertainty of CO₂ saturation (bottom panel) using Brie rock physics model with e = 3.
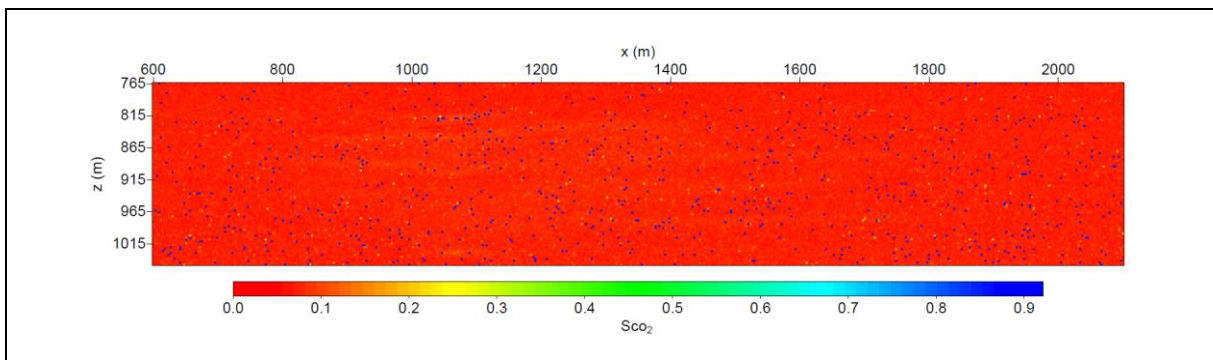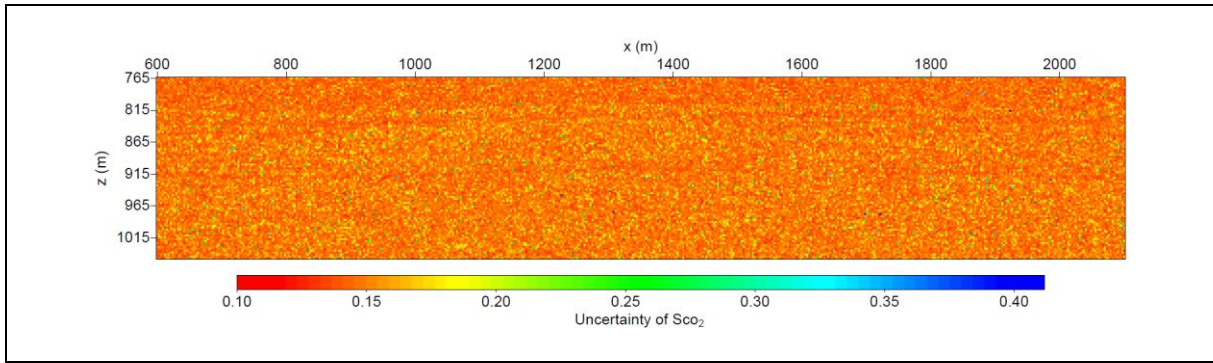
Figure 6-11. Estimation of CO₂ saturation (top panel) and uncertainty of CO₂ saturation (bottom panel) using Brie rock physics model with e = 40.
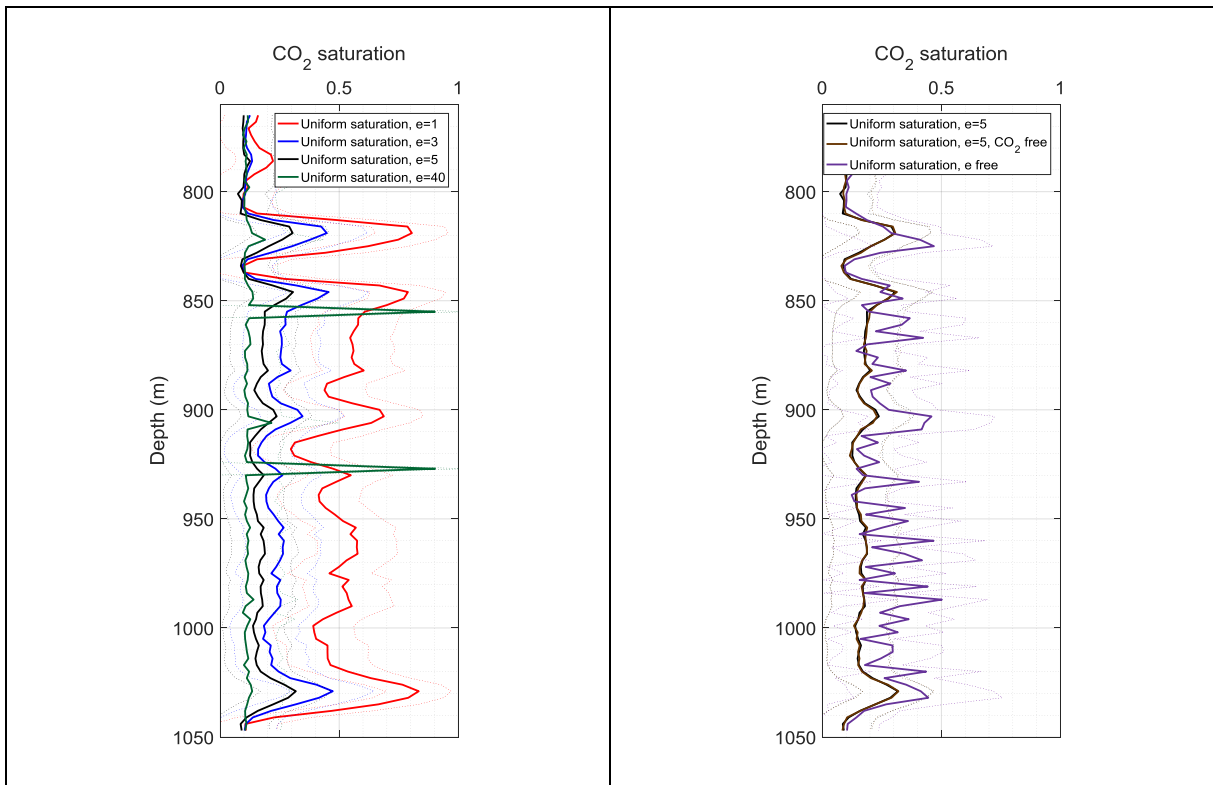
Figure 6-12. 1D estimation of CO₂ saturation using Brie rock physics model with different Brie exponent (left panel) and 1D estimation of CO₂ saturation using different rock physics models (right panel) for x = 1062 m. The dotted lines correspond to the mean value of estimation plus/minus uncertainty.
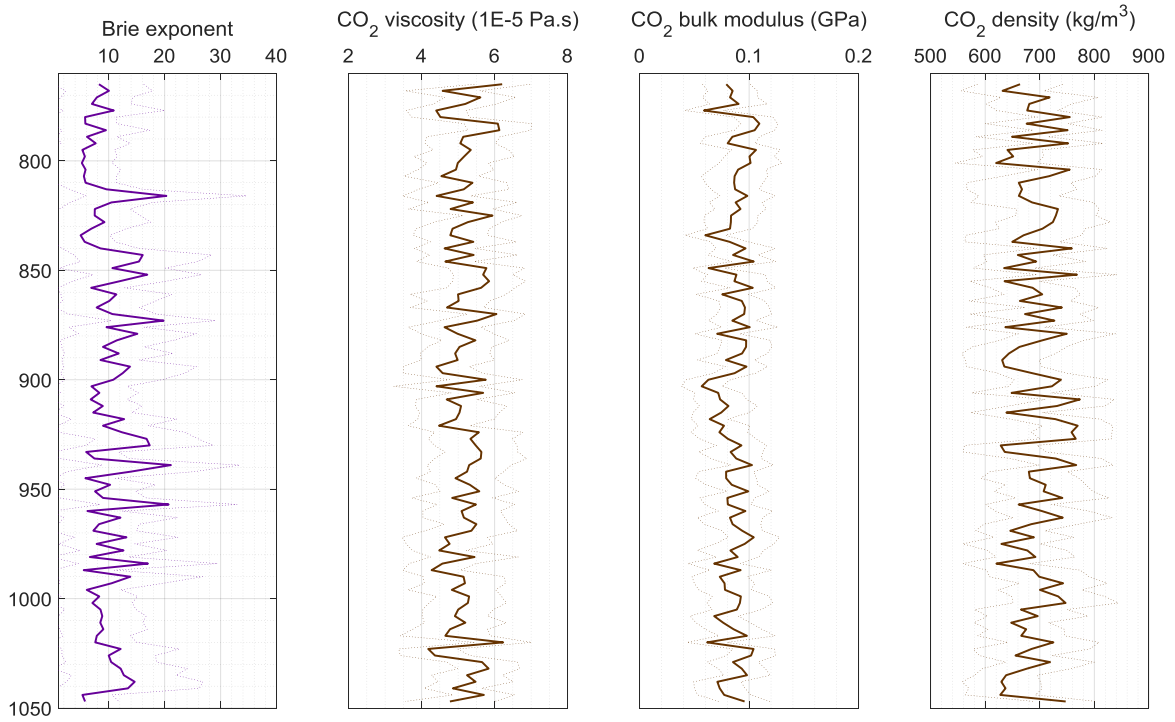
Figure 6-13. From left to right: 1D profile of Brie exponent and other CO₂ properties results (CO₂ viscosity, CO₂ bulk modulus, and CO₂ density) inverted jointly with the CO₂ saturation using different rock physics models for x = 1062 m. The dotted lines correspond to the mean value of estimation plus/minus uncertainty.

7 REAL DATA (INLINE 1881, VINTAGE 2008, AFTER IN-JECTION)

The data is obtained after CO_2 injection in 2008. This inline data is located at about 533 m away of the injection point. The seismic data after time migration of inline 1881 is given in Figure 7-1.
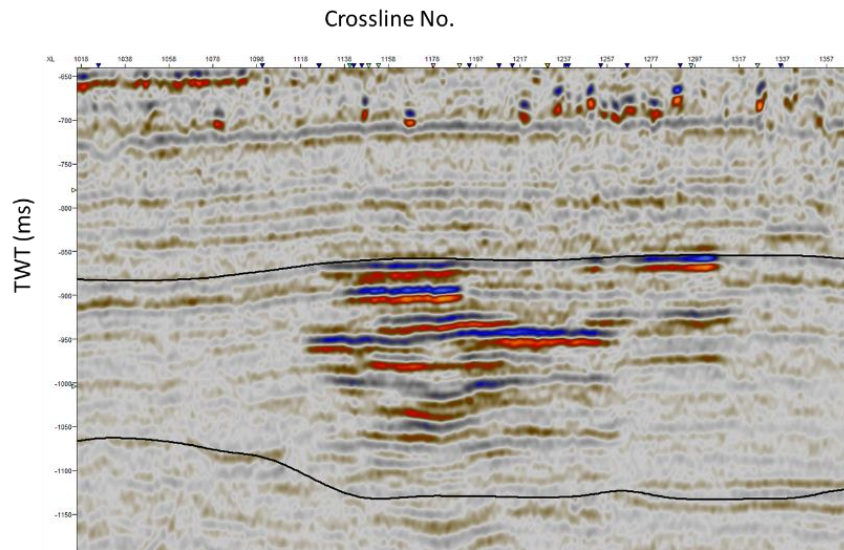
Figure 7-1. Seismic data after time migration from inline 1881.

7.1 Data preparation

Figure 7-2 shows the P-wave velocity derived from FWI. The CO_2 induced low P-wave velocity region is shown with warm colour (Figure 7-2). The FWI results are discussed in Romdhane and Querendez (2014).
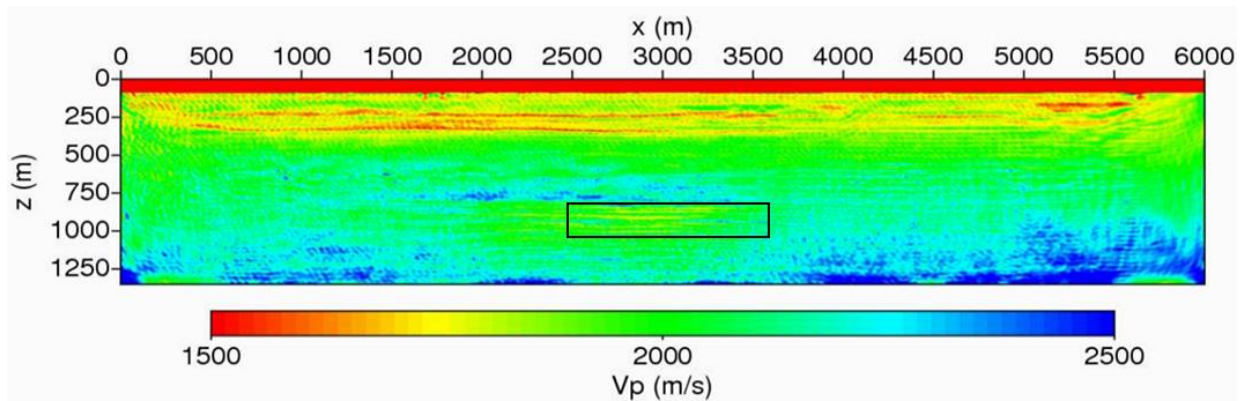
Figure 7-2. P-wave velocity for 2D real data section (inline 1881, 2008 vintage, after CO₂ injection). The black square shows the selected region of interest with CO₂ saturated.

In this case, we use the baseline information derived from the log data as described in Chapter 4. The 1D derived frame properties from the Well 15/9-A16 are smoothed and horizontally extended to 2D layered structure. For efficient computation, we selected a target region from the FWI model (Figure 7-3). The selected region consists of 95×401 grid points. We can see a moderate pushdown effect on P-wave velocity in the region caused by the contrast between the slow-velocity CO₂ and the surrounded high-velocity brine-saturated reservoir.
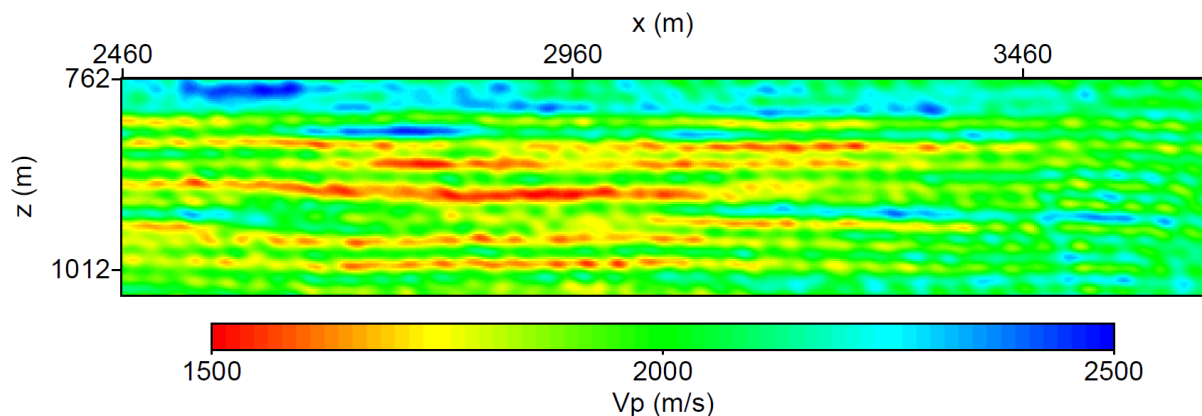
Figure 7-3. P-wave velocity model for target region.

The correlation between monitor P-wave velocity and reservoir frame properties are given by Figure 7-4. The 1D P-wave velocity profile is extracted at x = 2835 m. The log data derived frame properties are shifted form depth of 792 m - 1074 m to the depth of 762 m - 1044 m.
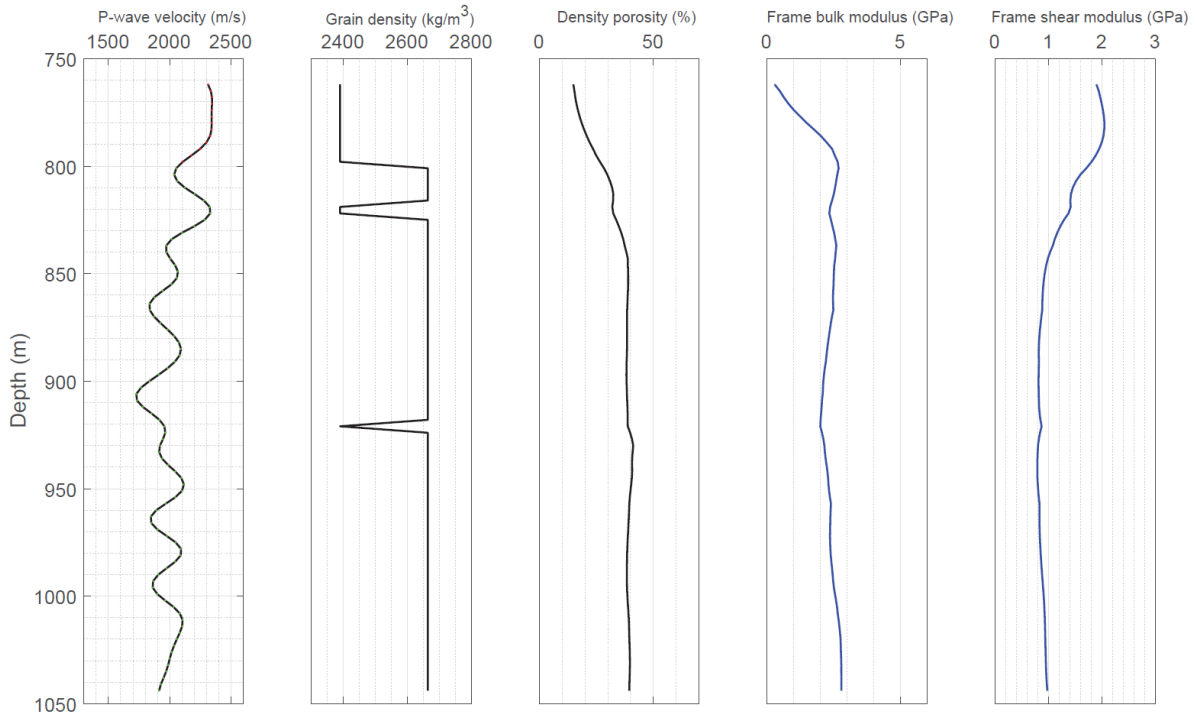
Figure 7-4. Correlation of P-wave velocity of inline 1881 real data and smoothed reservoir properties derived by log data. From left to right: P-wave velocity, grain density, density porosity, frame bulk modulus and frame shear modulus. The red dots indicate the Nordland caprock shale, and the green dots indicates the Utsira sandstone. The log data derived properties from 792 m are shifted to the depth of 762 m. The P-wave velocity profile is extracted at x = 2835 m.

7.2 Estimation of CO_2 saturation

We apply the rock physics tool to the selected region of inline 1881 real data. The estimation of CO_2 saturation for uniform saturation model with Brie exponent e = 5 is given in Figure 7-5. The estimations of CO_2 saturation within the sandstone layers vary in the range of 13% - 30% with a maximum misfit of 0.1. The CO_2 saturation estimates within the sandstone layers are known with ± 0.13 to 0.16 uncertainty. The higher deviation is present where the CO_2 saturation is higher.
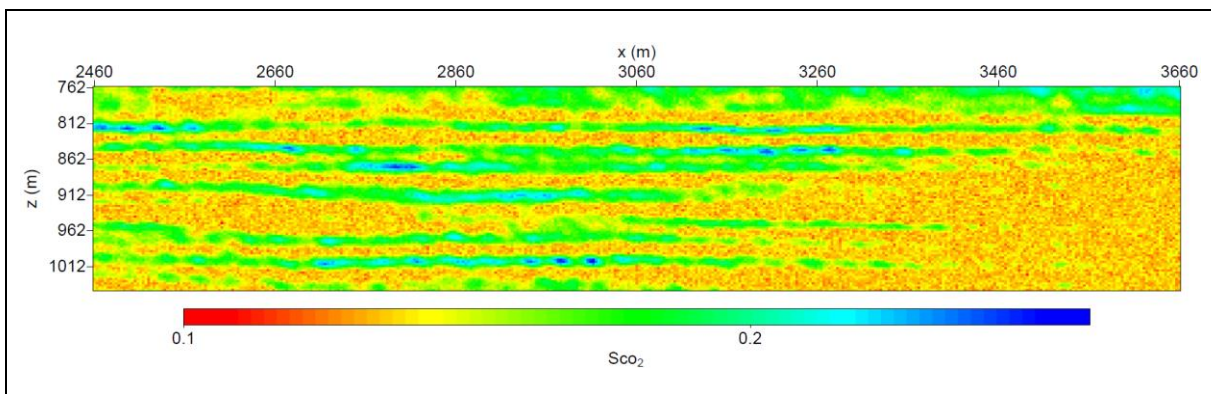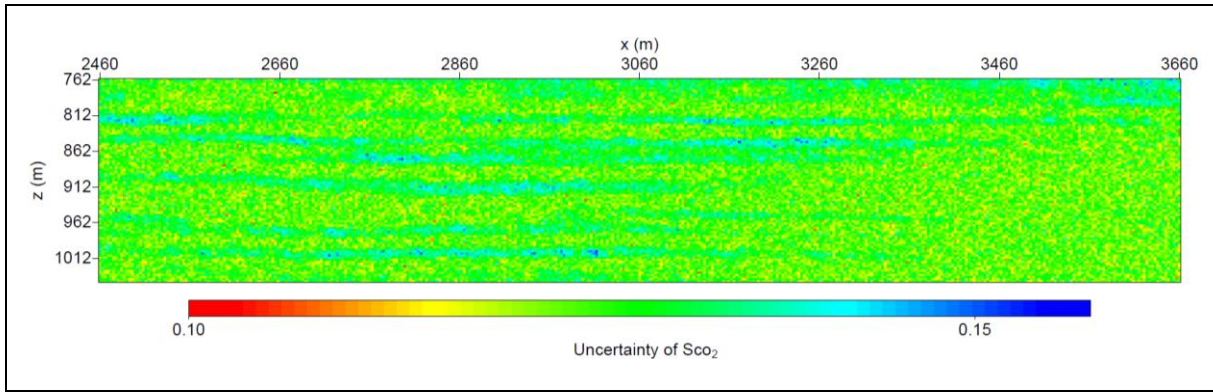
Figure 7-5. Estimation of CO$_2$ saturation (top panel) and uncertainty of CO$_2$ saturation (bottom panel) using Brie rock physics model with e = 5.

The estimations of CO$_2$ saturation and Brie exponent are given in Figure 7-6. The estimations of CO$_2$ saturation within the CO$_2$ saturated sand layers vary in the range of 10% - 56% $\pm$ 0.12 to 0.24 uncertainty. The Brie exponent e varies from 5 to 16 with an uncertainty ranging around 6–15.
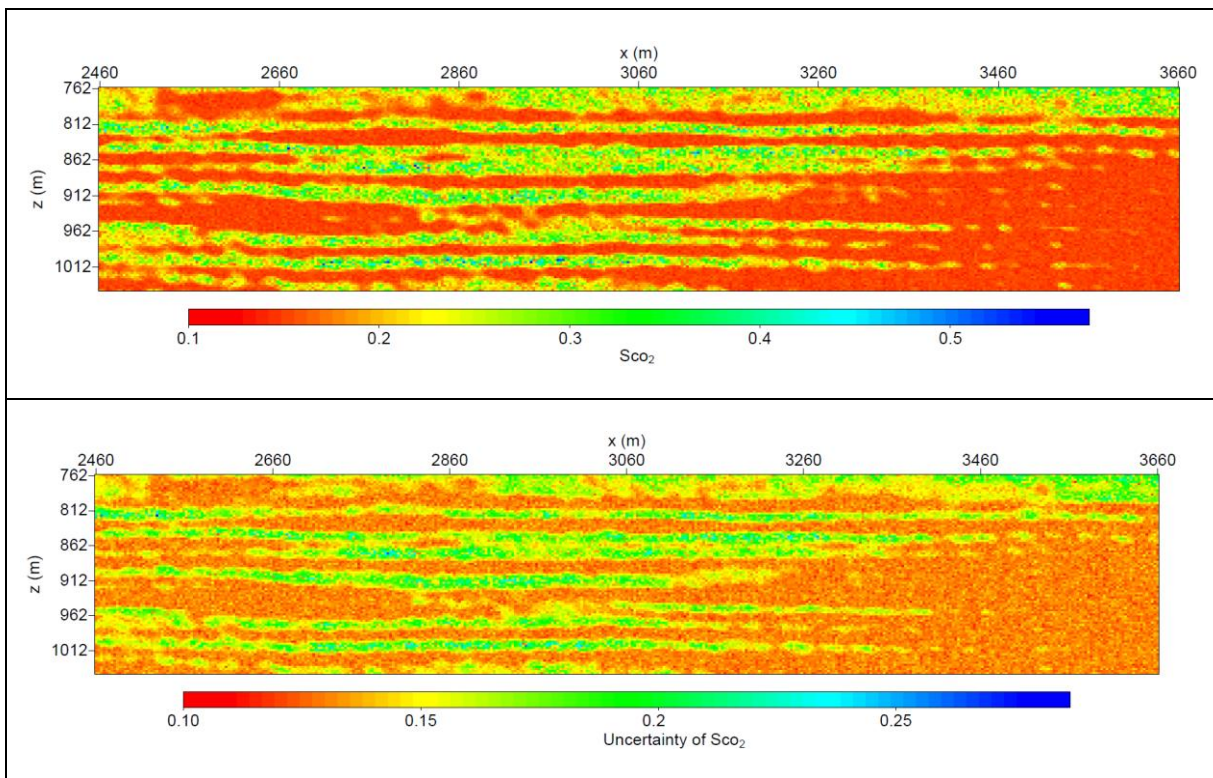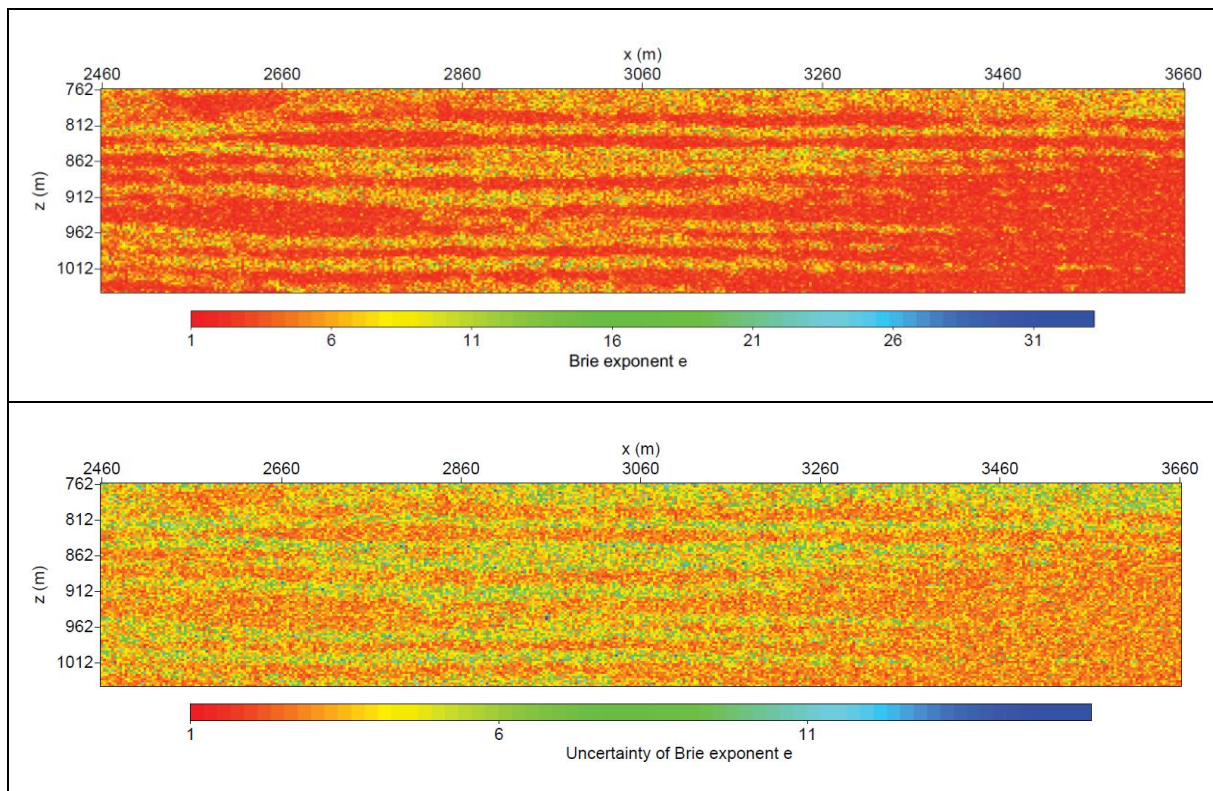
Figure 7-6. From top to bottom: estimation of CO₂ saturation, uncertainty of CO₂ saturation, estimation of Brie exponent, and uncertainty of Brie exponent e using Brie rock physics model with Brie exponent e inverted.

We also conduct the Brie rock physics model for cases of fully patchy mixing with e = 1 (Figure 7-7) and fully uniform mixing with e = 40 (Figure 7-9), and the case with e = 3 (Figure 7-8) (Brie et al., 1995). The Brie rock physics model with e = 1 gives the highest estimation of CO_2 saturation up to 62% $\pm$ 0.2 uncertainty. While the estimation of CO_2 saturation using e = 40 have a high uncertainty up to 0.4. The estimation of CO_2 saturation using e = 3 is similar with that using e = 5. The 2D estimation results of CO_2 saturation from patchy saturation model are very low and not shown here for brevity.
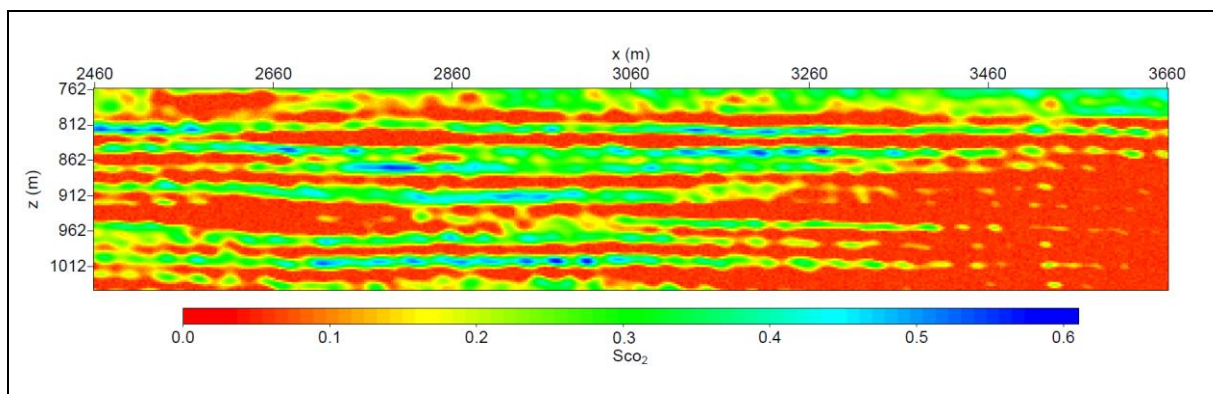
Figure 7-7. Estimation of CO₂ saturation (top panel) and uncertainty of CO₂ saturation (bottom panel) using Brie rock physics model with e = 1.

Figure 7-8. Estimation of CO₂ saturation(top panel) and uncertainty of CO₂ saturation (bottom panel) using Brie rock physics model with e = 3.
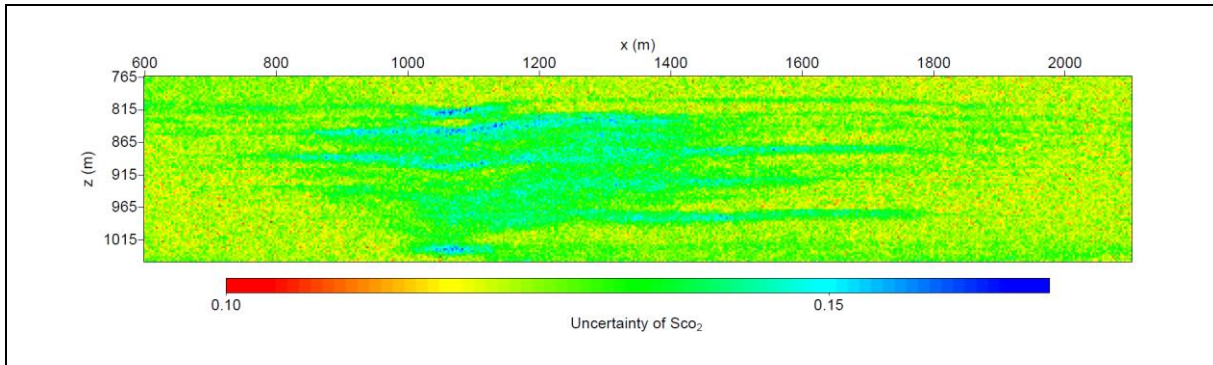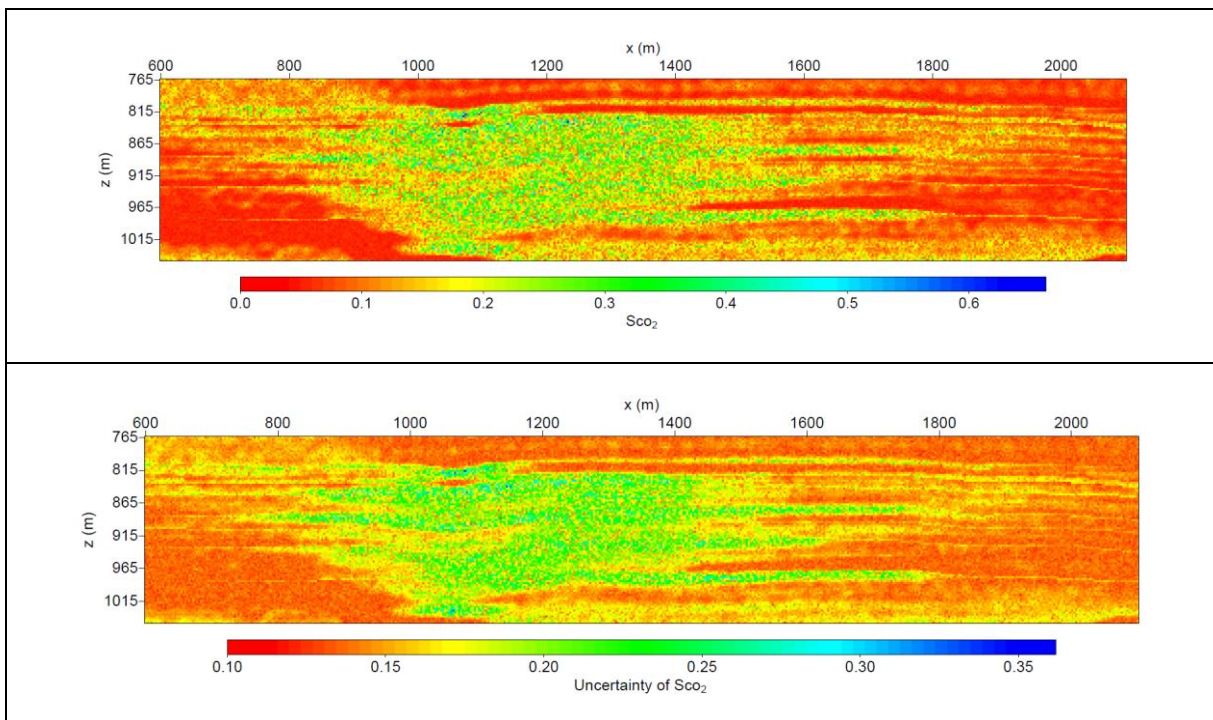
Figure 7-9. Estimation of CO₂ saturation (top panel) and uncertainty of CO₂ saturation (bottom panel) using Brie rock physics model with e = 40.

Figure 7-10 shows the estimation results when we use a Brie rock physics model (e = 5) to invert CO_2 saturation and CO_2 properties (CO_2 bulk modulus, density, and viscosity) simultaneously. The estimated CO_2 saturation is similar with the case when CO_2 properties are defined (Figure 7-5). The figures of estimation results for other CO_2 properties (CO_2 bulk modulus, density, and viscosity) are not shown here for brevity.
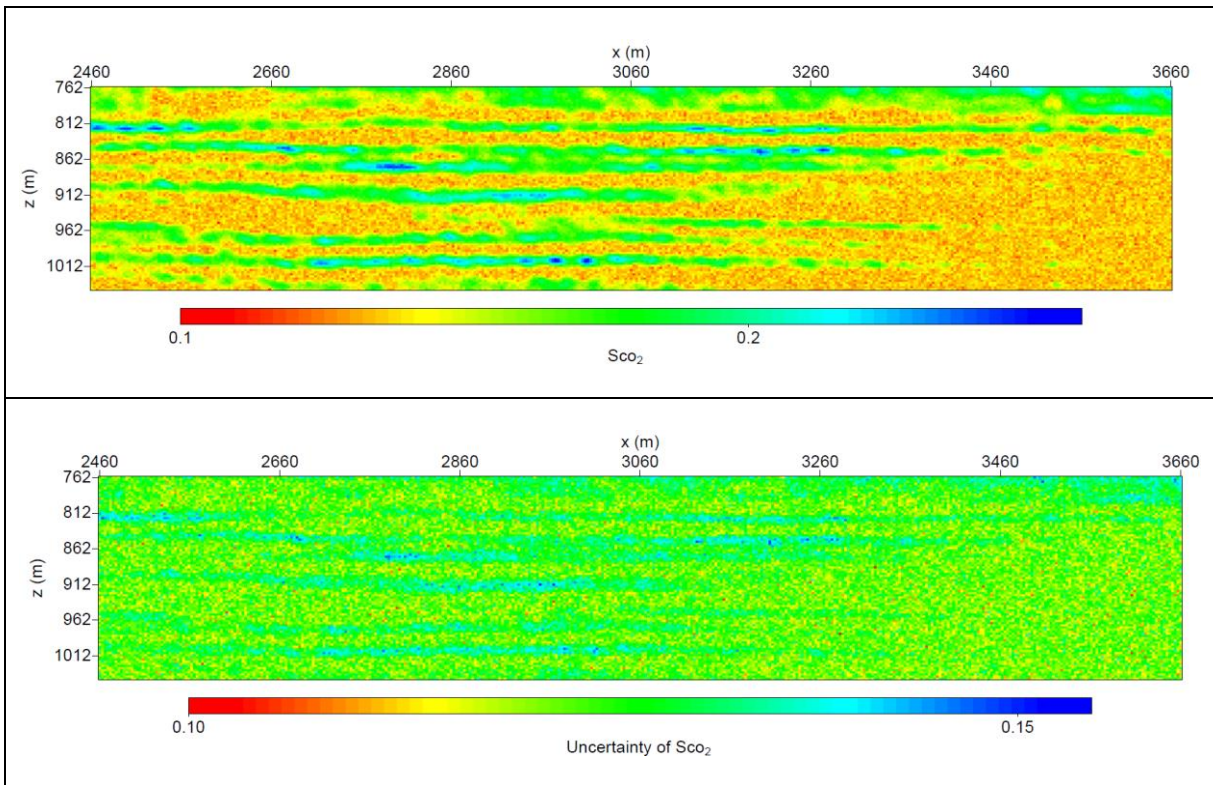
Figure 7-10. Estimation of CO₂ saturation (top panel) and uncertainty of CO₂ saturation (bottom panel) using Brie rock physics model (e = 5) with other CO₂ properties inverted.

To better understand and compare the estimations of CO_2 saturation by different rock physics models, we compare the results for 1D profiles (Figure 7-11, Figure 7-12) for x = 2835 m.

Figure 7-11. 1D estimation of CO_2 saturation using Brie rock physics model with different Brie exponent (left panel) and 1D estimation of CO_2 saturation using different rock physics models (right panel) for x = 2835 m. The dotted lines correspond to the mean value of estimation plus/minus uncertainty.

Figure 7-11 shows the 1D profile of CO_2 saturations estimated using different rock physics models. The uniform saturation model with a smaller Brie exponent gives a higher estimation of CO_2 saturation. The higher Brie exponent e is indicating that the fluids are mixed at the finest scale (uniform mixing). The estimation of CO_2 saturation is low with around 12% for uniform saturation model with e = 40 within the CO_2 saturated zone. The high CO_2 saturation phenomenon is located in 7 layers at depths of approximately 810 m, 846 m, 873 m, 918 m, 942 m, 972 m and 1005 m. The difference of the estimated CO_2 saturation from uniform saturation using different Brie exponents is bigger for the shallower layers, which seems to be saturated with a higher CO_2 concentration. The estimation of CO_2 saturation is more consistent for the deeper deposited layers with lower CO_2 saturation. It could be due to the buoyancy effect controlling the CO_2 migration towards upper layers (with temporary boundaries created by the thin intra-shale layers). In addition, estimation of CO_2 saturation varies dramatically and seems higher than the other models when we use the uniform saturation to invert CO_2 saturation and CO_2 properties simultaneously. On the contrary, the patchy saturation with a bubble size *a* equal to 0.01 m gives a lower estimation of CO_2 saturation. This could be due to the limit validity range

of patchy saturation. Therefore, we do not show this model for real data application on inline 1838.

The jointly estimated CO_2 properties and Brie exponent are given in Figure 7-12. The higher estimation of Brie exponent (8 - 16) and the higher estimation of CO_2 saturation seem to have a spatial correlation. The CO_2 properties are difficult to inverted, while given a reasonable range of CO_2 properties can give a similar estimation of CO_2 saturation with defined range of properties. In this context, if we know the pressure and temperature in the reservoir, we can have reasonable ranges for CO_2 properties. For example, Alnes et al. (2011) study the CO_2 density variation at Sleipner using gravity data. They consider the increased temperature effects and conclude that the density variation is small (675 ± 20 kg/m^3).

Figure 7-12. From left to right: 1D profile of Brie exponent and other CO_2 properties results (CO_2 viscosity, CO_2 bulk modulus, and CO_2 density) inverted jointly with the CO_2 saturation using different rock physics models for x = 2835 m. The dotted lines correspond to the mean value of estimation plus/minus uncertainty.

57

8 REAL DATA (INLNE 1838, VINTAGE 1994, BEFORE IN-JECTION)

The idea for this section is to characterize the baseline frame properties before the CO_2 injection. The derived reservoir information will be used as input to the estimation of CO_2 saturation. Figure 8-1 and Figure 8-2 show the starting velocity for FWI and P-wave velocity tomography from FWI, respectively. The baseline information is based on the seismic data acquired in 1994.
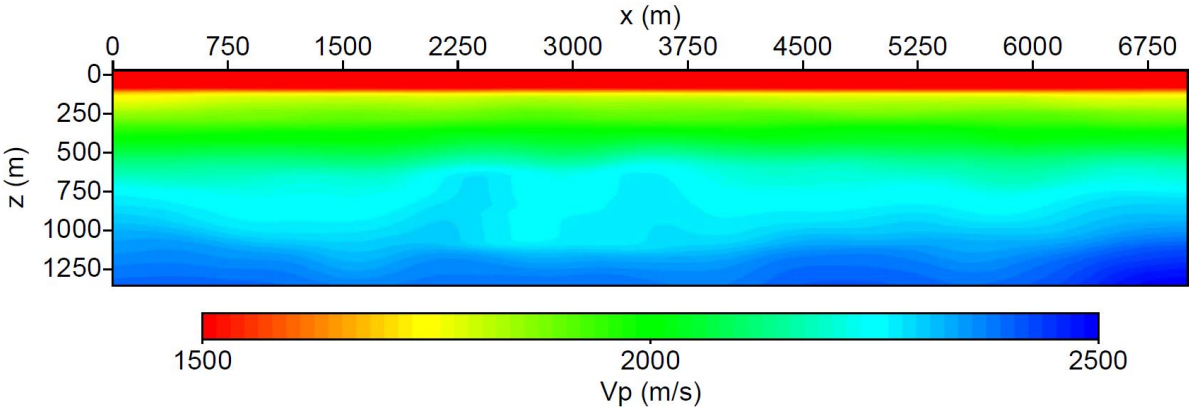
Figure 8-1. P-wave velocity starting model for FWI.
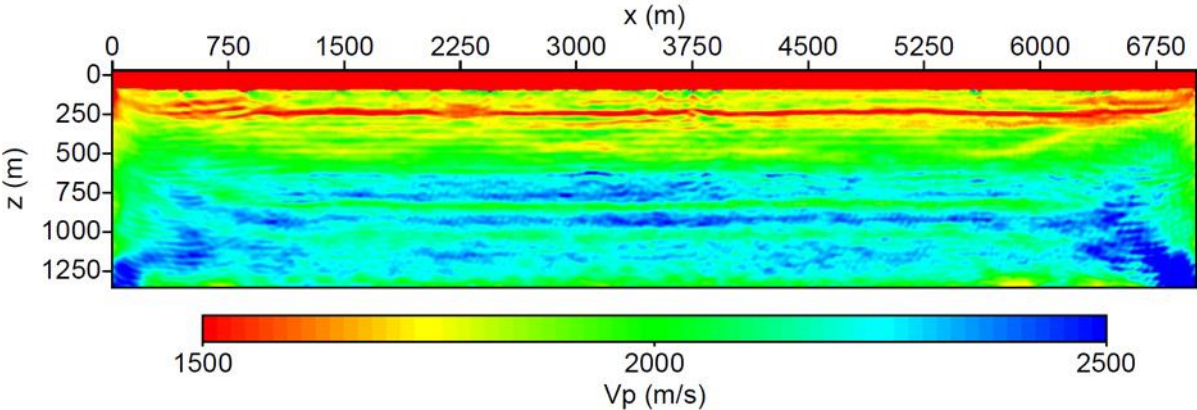
Figure 8-2. P-wave velocity model at last iteration of FWI using smoothing $r_2 = 5$.

8.1 Data preparation and a priori rock properties

A target region is selected after we analysed the FWI results for the monitor data that will be described in Chapter 9. The selected P-wave velocity is given in Figure 8-3. Based on the gradient (first derivative) of the P-wave velocity with respect to depth, we can identify 10 distinct horizons and construct the lithology variations, which are later used to define the a priori rock properties.

58
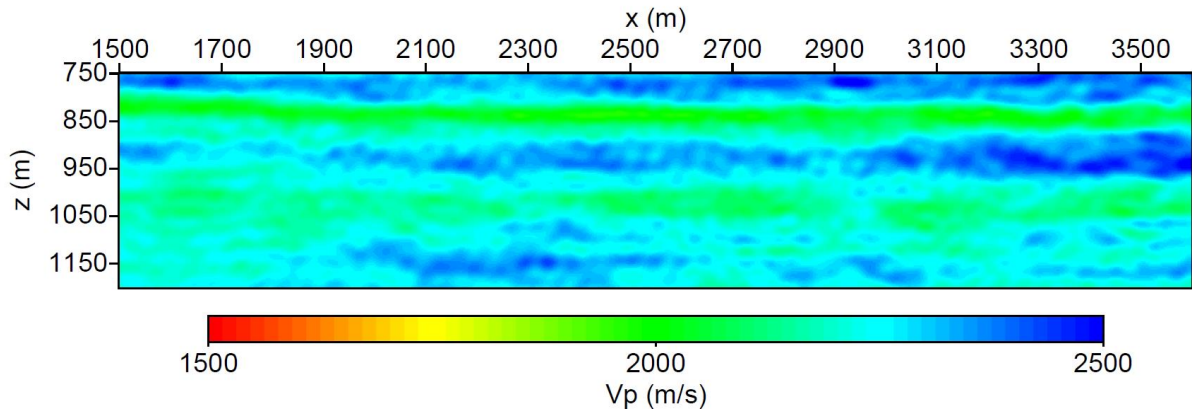
Figure 8-3. Selected P-wave velocity model for vintage 1994 before CO₂ injection.

Because S-wave velocity and bulk density are crucial for the estimation of frame properties (Dupuy et al., 2017), we build the S-wave velocity (Figure 8-4) and the bulk density by using Vernik's and Gardner's relation (Mavko et al., 2009), respectively (see equations (21), (22)). Porosity is derived using a density porosity relation (see equation (23)).
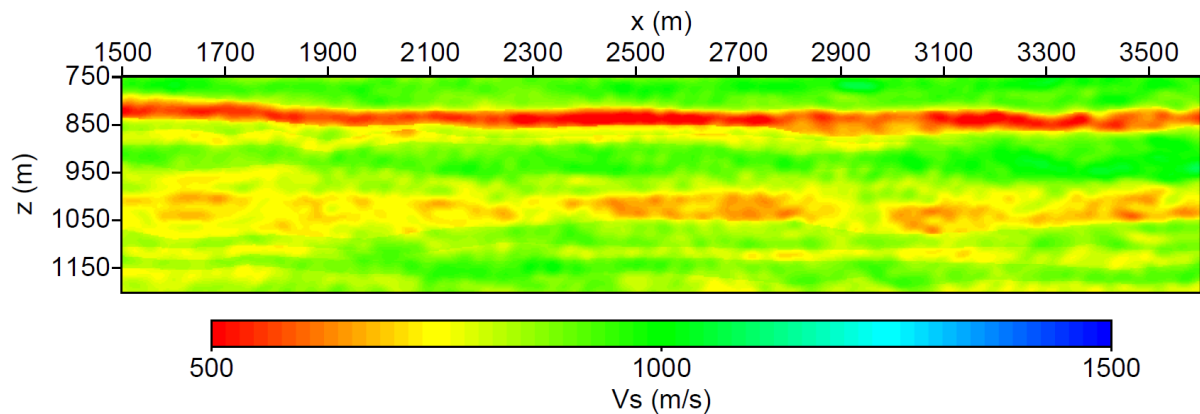
Figure 8-4. S-wave velocity model obtained from Vernik's relation.

The corresponding 2D properties of permeability, cementation factor and grain density are built according to the a priori properties as given in Table 3-1. Then, based on the 2D a priori properties, we invert the bulk and shear frame moduli by combination of inputs of P- and S-wave velocities, and bulk density. The estimation result is given using the mean value of the models with misfit lower than 0.1.

8.2   Estimation of frame moduli

The estimation results of K_d and G_d (including the related uncertainty) from V_P, V_S, and density are shown in Figure 8-5.
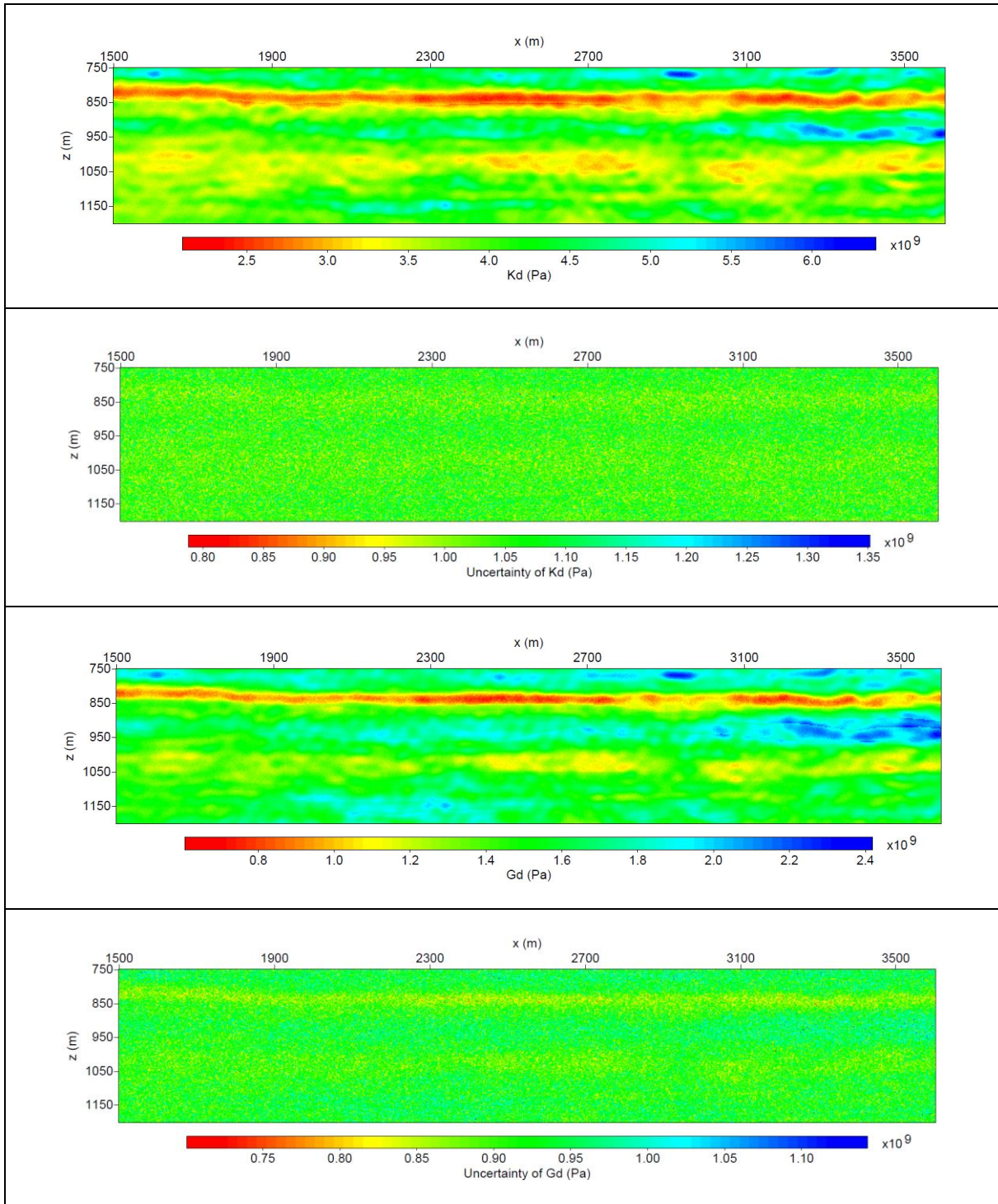
Figure 8-5. From top to bottom: estimation of frame bulk modulus K_d, uncertainty of frame bulk modulus K_d , estimation of frame shear modulus G_d, and uncertainty of frame shear modulus G_d.

From the 2D estimation results, we average the derived frame properties for all shale and sandstone layers, respectively. Table 8-1 summarises the obtained results.

Table 8-1. Averaged estimated frame moduli and porosity derived for baseline vintage (1994).

Lithology	K_d (GPa)	G_d (GPa)	Porosity
Shale	4.25	1.67	24 %
Sandstone	3.60	1.42	38 %

We also tried the test to estimate K_d and G_d with only P-wave velocity as input (Figure 8-6). We observe higher uncertainties related to the frame moduli estimation. As the inversion system is under-determined, the frame moduli results (Figure 8-6) have a checkerboard pattern but the main trends are still visible.
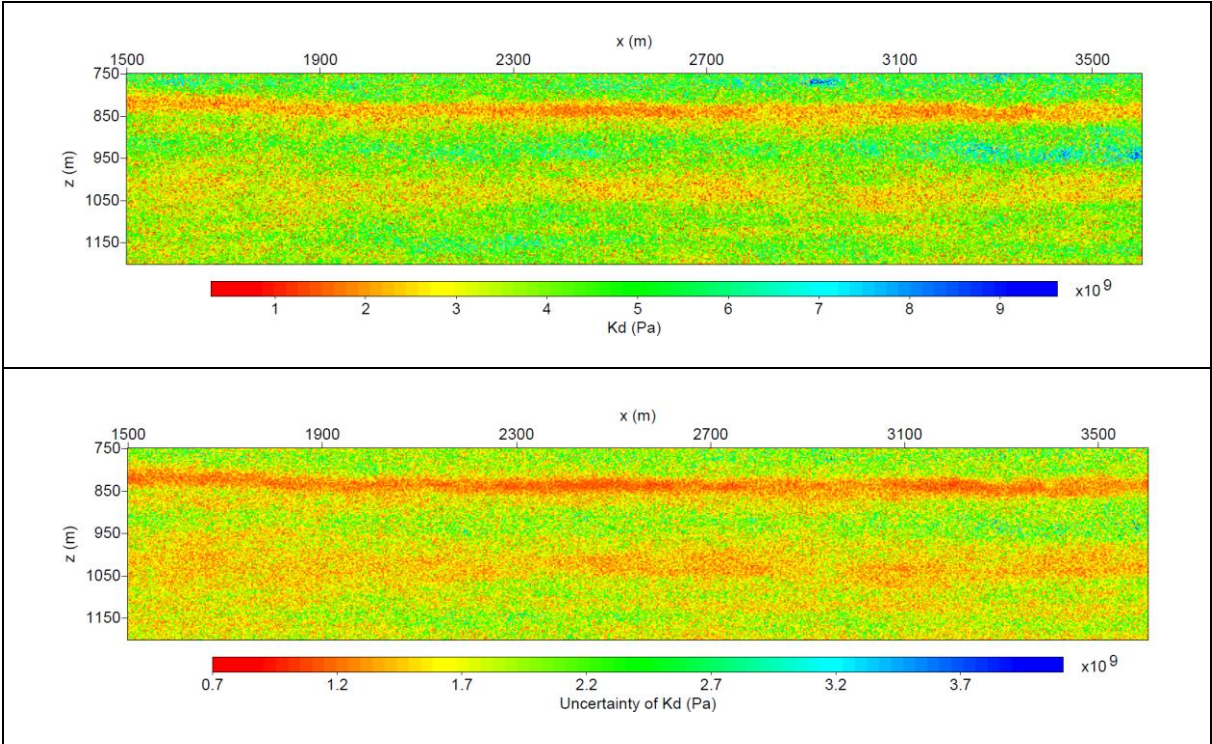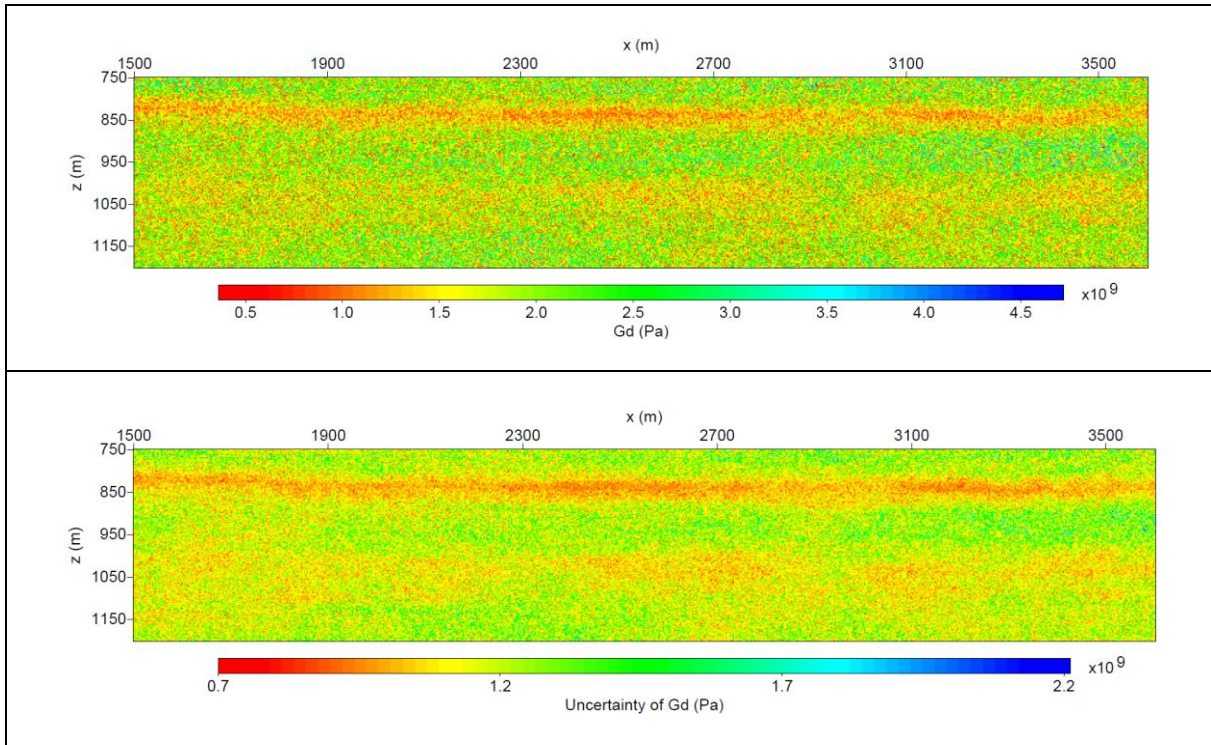
Figure 8-6. From top to bottom: estimation of frame bulk modulus K$_d$, uncertainty of frame bulk modulus K$_d$, estimation of frame shear modulus G$_d$, and uncertainty of frame shear modulus G$_d$ using only P-wave velocity as input.

9 REAL DATA (INLINE 1838, VINTAGE 2008, AFTER IN-JECTION)

Inline 1838 is the section where the injection point is located Figure 9-1.

Figure 9-1. Seismic data after time migration for inline 1838.

Figure 9-2 shows P-wave starting model for FWI. The starting model is extracted from the seismic data acquired in 2008. Figure 9-3 shows the P-wave velocity from FWI. The extension of low P-wave velocity region is a bit larger than that for inline 1881 (Figure 7-2). More information about data processing and FWI tests can see Appendix C

Figure 9-2. P-wave velocity starting model for FWI.

Figure 9-3. P-wave velocity model at last iteration of FWI using smoothing $r_2 = 5$.

9.1   Data preparation and a priori rock properties

The RPI is applied to the FWI derived P-wave velocity. We select a region corresponding to the CO_2 accumulation (Figure 9-4).
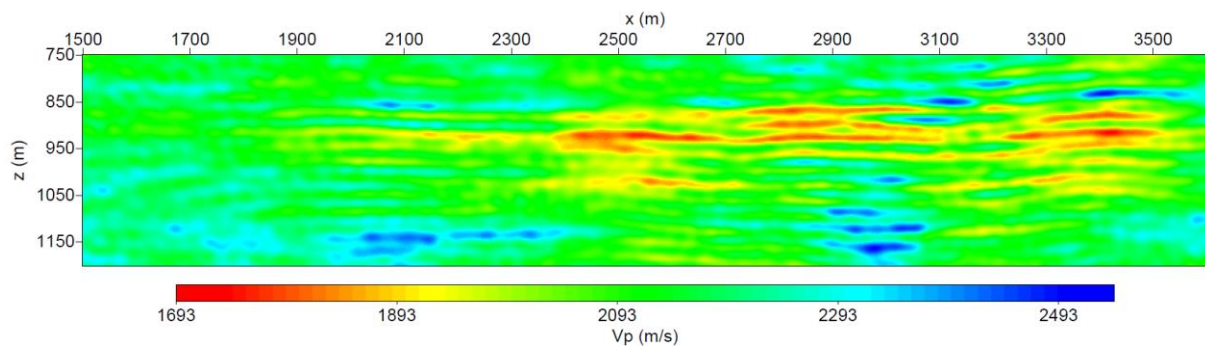
Figure 9-4. Selected P-wave velocity model for vintage 2008 (inline 1838).

The a priori frame properties are built (Figure 9-5) based on the structure of P-wave velocity gradient after CO_2 injection and based on the properties derived from the baseline before CO_2 injection shown in Table 8-1. The other a priori properties (grain density, grain bulk modulus, permeabityand cemetation factor) are built in the same way.
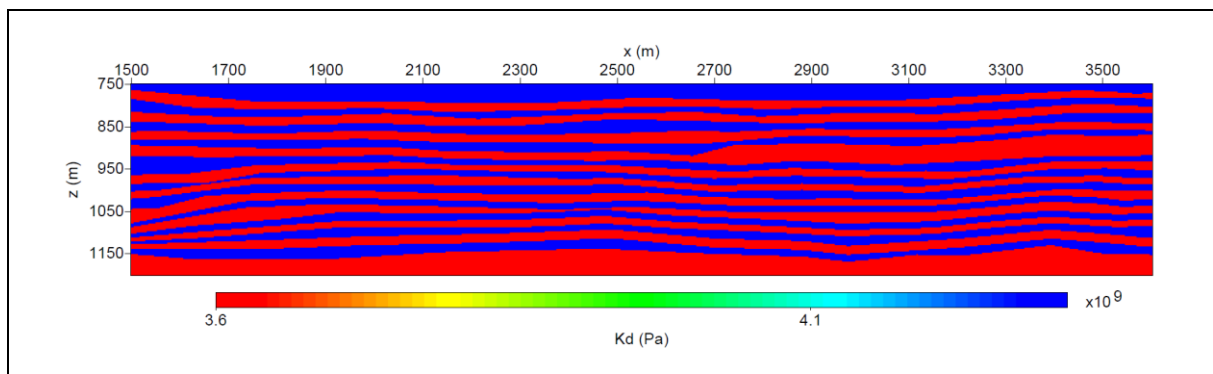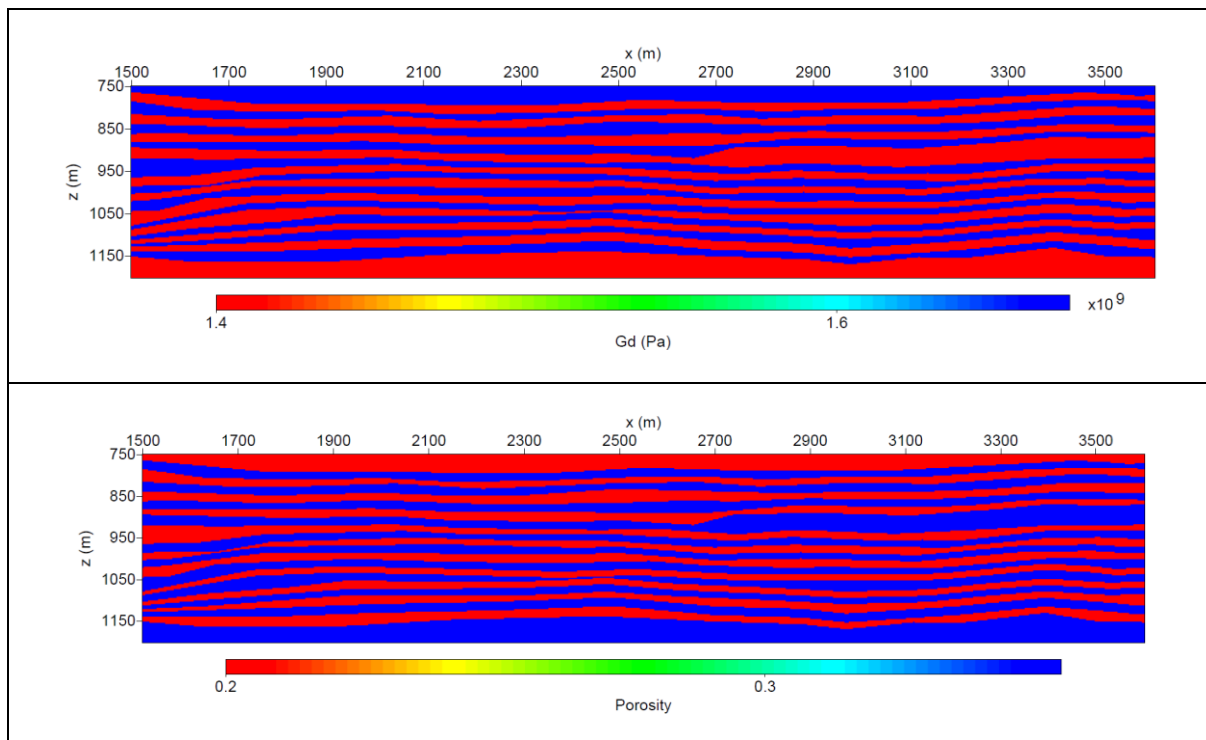
Figure 9-5. From top to bottom: frame bulk modulus K_d, frame shear modulus G_d, porosity.

9.2 Estimation of CO_2 saturation

The estimation results of CO_2 saturation are shown in following figures, including the related uncertainty analysis. Due to the limited range of validity of the patchy saturation model (only high or low saturations), we only show the results for the uniform saturation model.

Figure 9-6 shows the estimation of CO_2 saturation using e = 5. There are two distinct high CO_2 saturated layers, one at depth of around 1140 m, which could be around the injection point. Another is at depth from 900 m – 950 m, which is just below the caprock with a high amount CO_2 trapped. The estimations of CO_2 within the sandstone layer at 1140 m has CO_2 saturations from 30% to 40%. The CO_2 saturation is higher (from 30% to 75%) in the top layers. The uncertainty of the estimation for CO_2 saturation within the sandstone layers is around 0.15 to 0.23. In general, we observe that higher uncertainty is associated with the high CO_2 saturated regions.
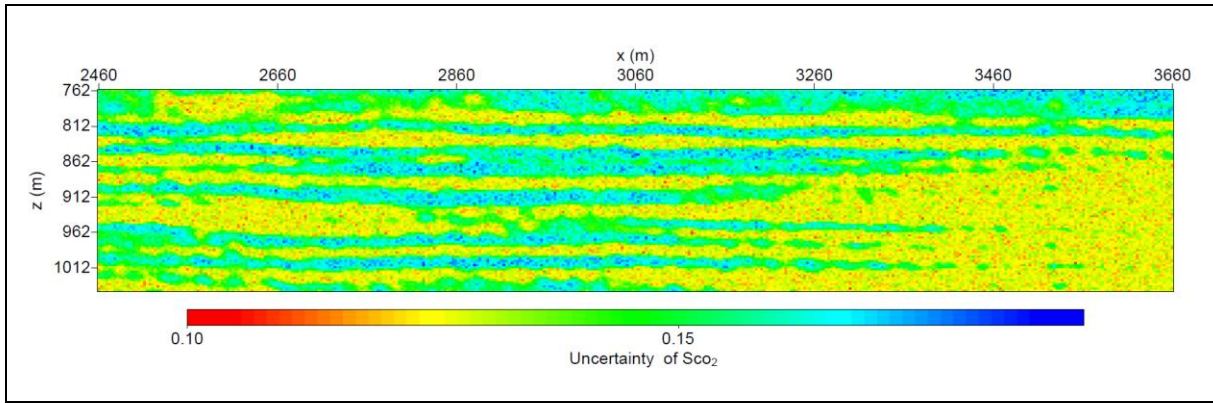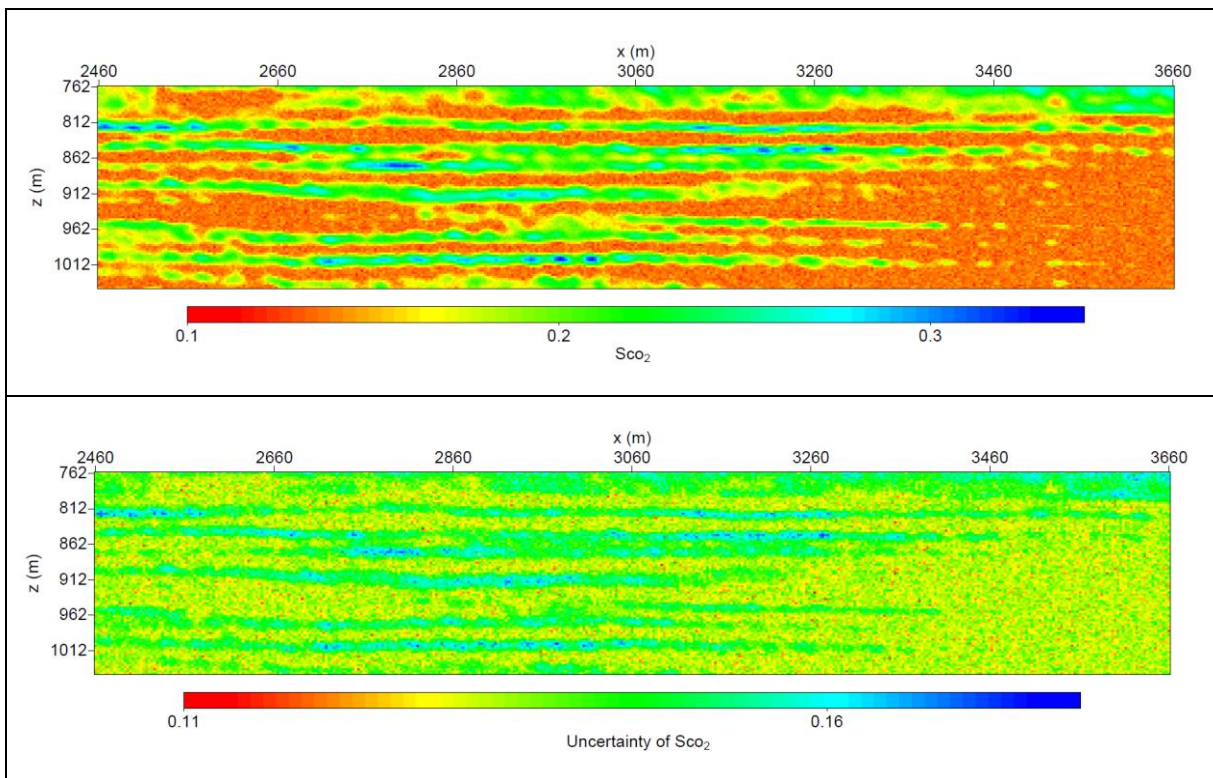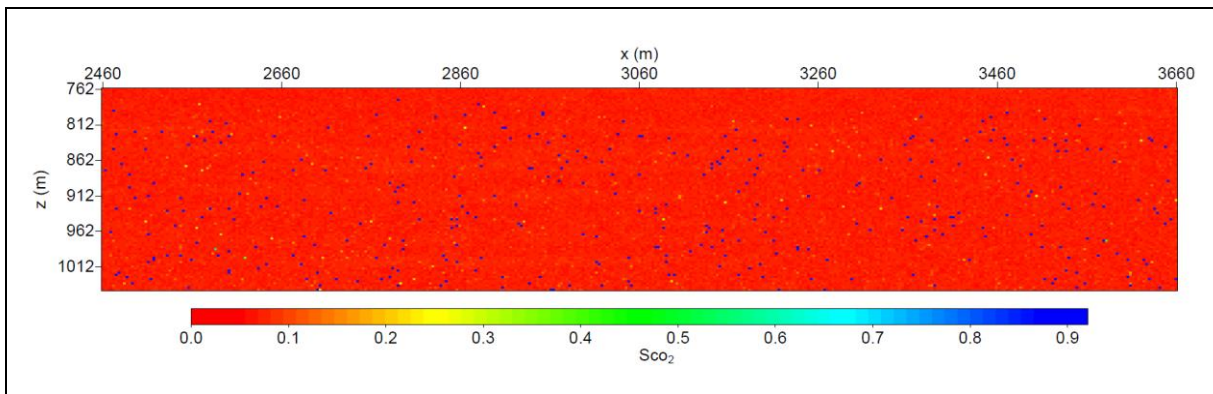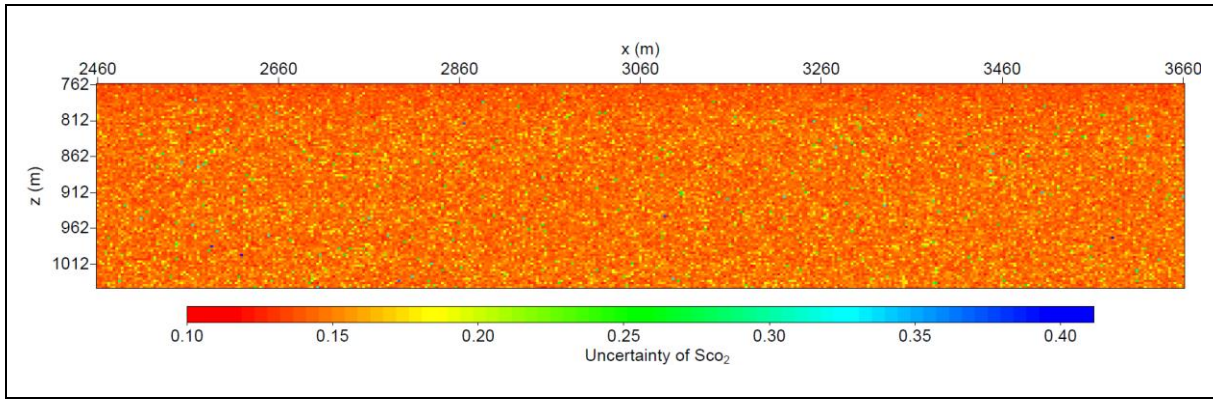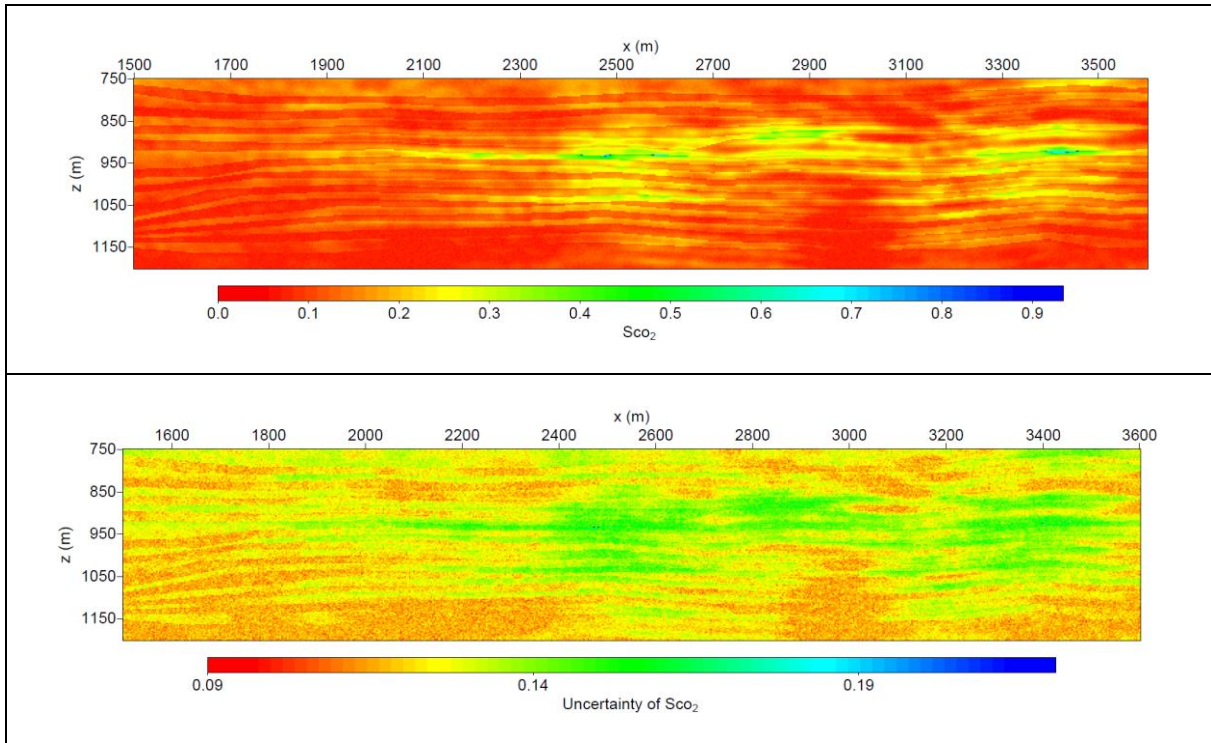
Figure 9-6. Estimation of CO₂ saturation (top panel) and uncertainty of CO₂ saturation (bottom panel) using Brie rock physics model with e = 5.

Figure 9-7 shows the estimations of CO_2 saturation and Brie exponent. The estimations of CO_2 saturation within the sand layers vary in the range of 30% to 70%. The estimation of CO_2 saturation within sand layers is known with $\pm$ 0.15 to 0.3 uncertainty. The Brie exponent e within CO_2 saturated layers varies from 10 to 28 with an uncertainty about 6 to 16. The estimated Brie exponent is higher and more uniform than we found for inline 1881.
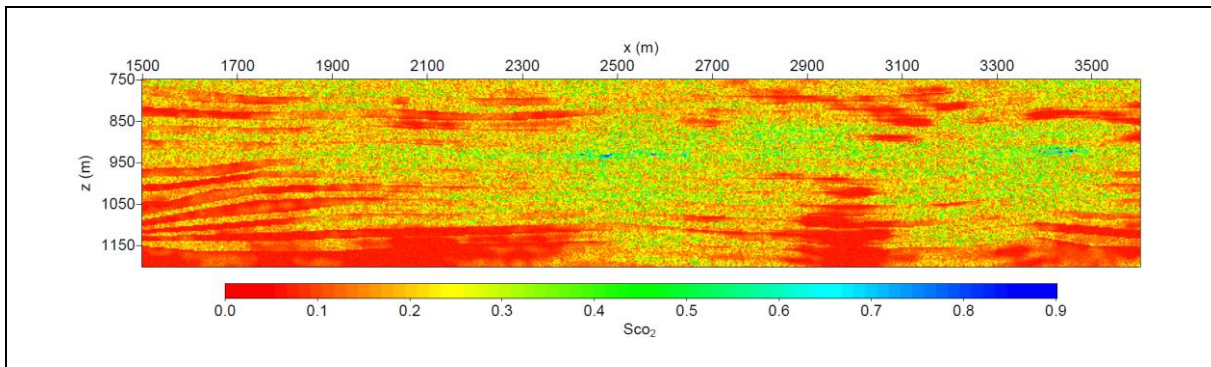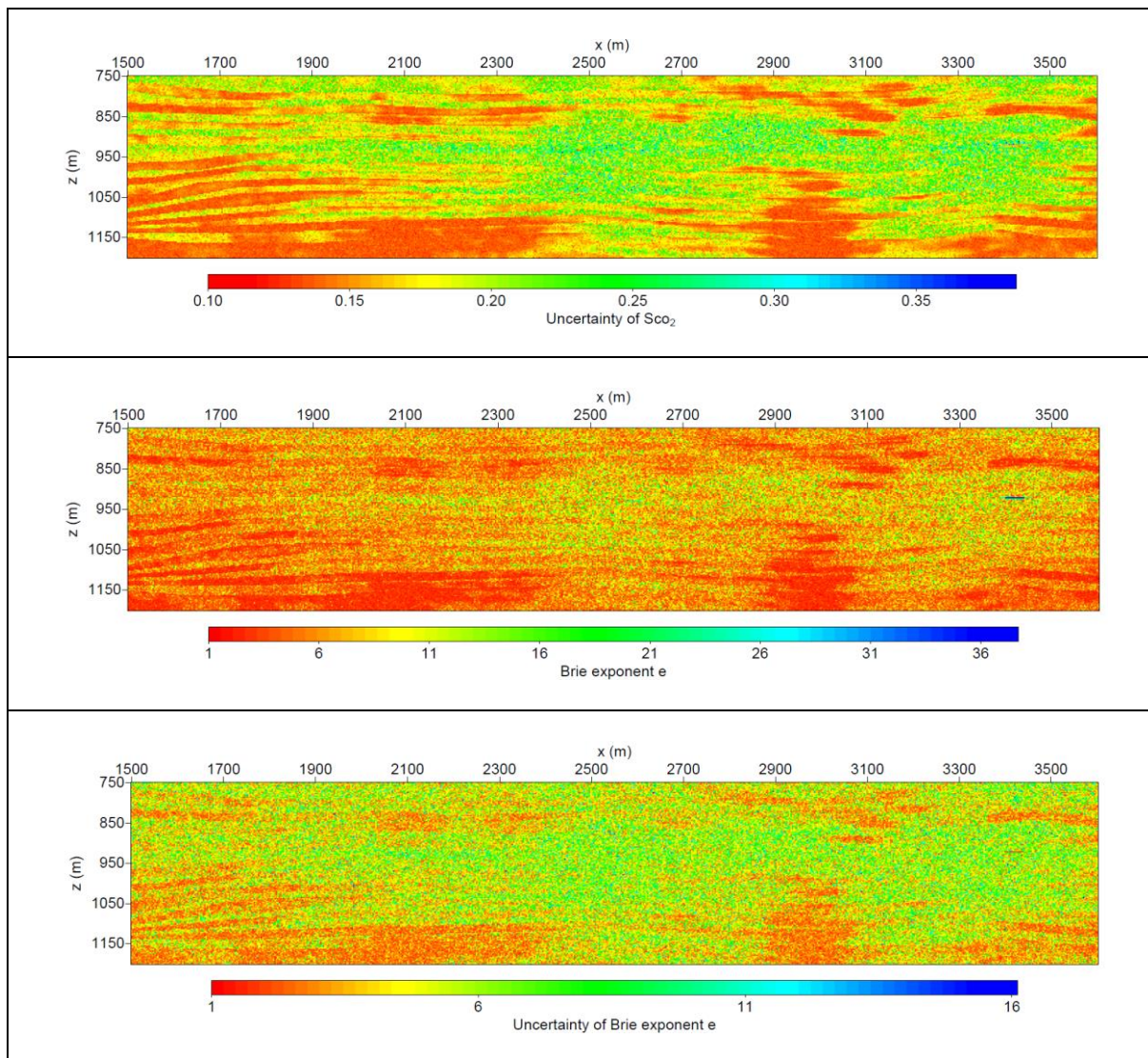
Figure 9-7. From top to bottom: estimation of CO₂ saturation, uncertainty of CO₂ saturation, estimation of Brie exponent, and uncertainty of Brie exponent using Brie rock physics model with Brie exponent e inverted.

The other estimation results of CO_2 saturation from uniform saturation are not shown here for brevity. To better understand the results, we select 1D vertical profiles, some crossing the CO_2 accumulations (Figure 9-8, Figure 9-9, Figure 9-10, Figure 9-11, Figure 9-12, Figure 9-13) and one vertical profile outside of the main plume (Figure 9-14).

We find that patchy mixing (e = 1) tends to give the highest estimation of CO_2 saturation (up to 90 − 100%). The uniform mixing (e = 40) seems to give peak responses for CO_2 saturation within CO_2 accumulated layers (top or near the injection points). The Brie exponent is also higher within CO_2 layers. In summary, the highest CO_2 saturation appears at the depth of around 935 m - 940 m. In addition, we found that the estimated CO_2 saturation is varying around 10% for the one vertical profile (Figure 9-14) outside of the main plume. The CO_2 properties (CO_2

viscosity, CO_2 bulk modulus, and CO_2 density) cannot be well estimated using only P-wave velocity (Figure 9-9, Figure 9-11, Figure 9-13), which is similar as our other case studies (Dupuy et al., 2017; Yan, 2016).
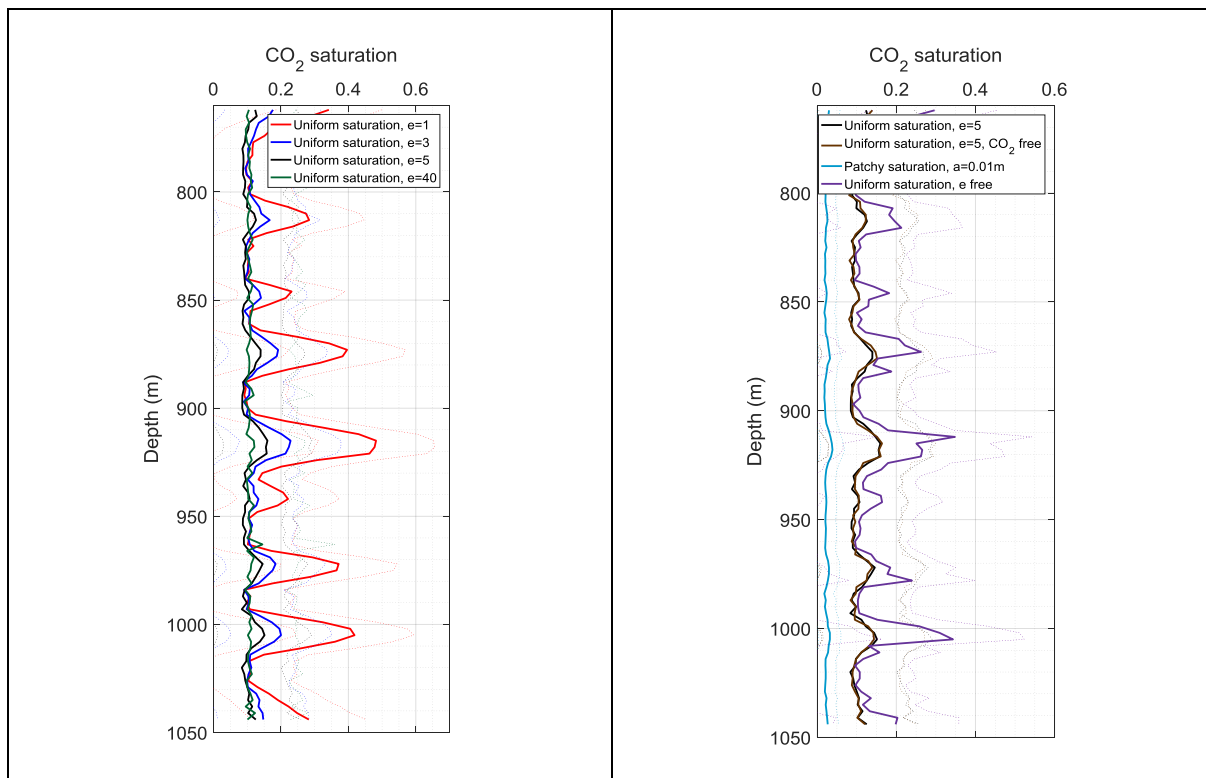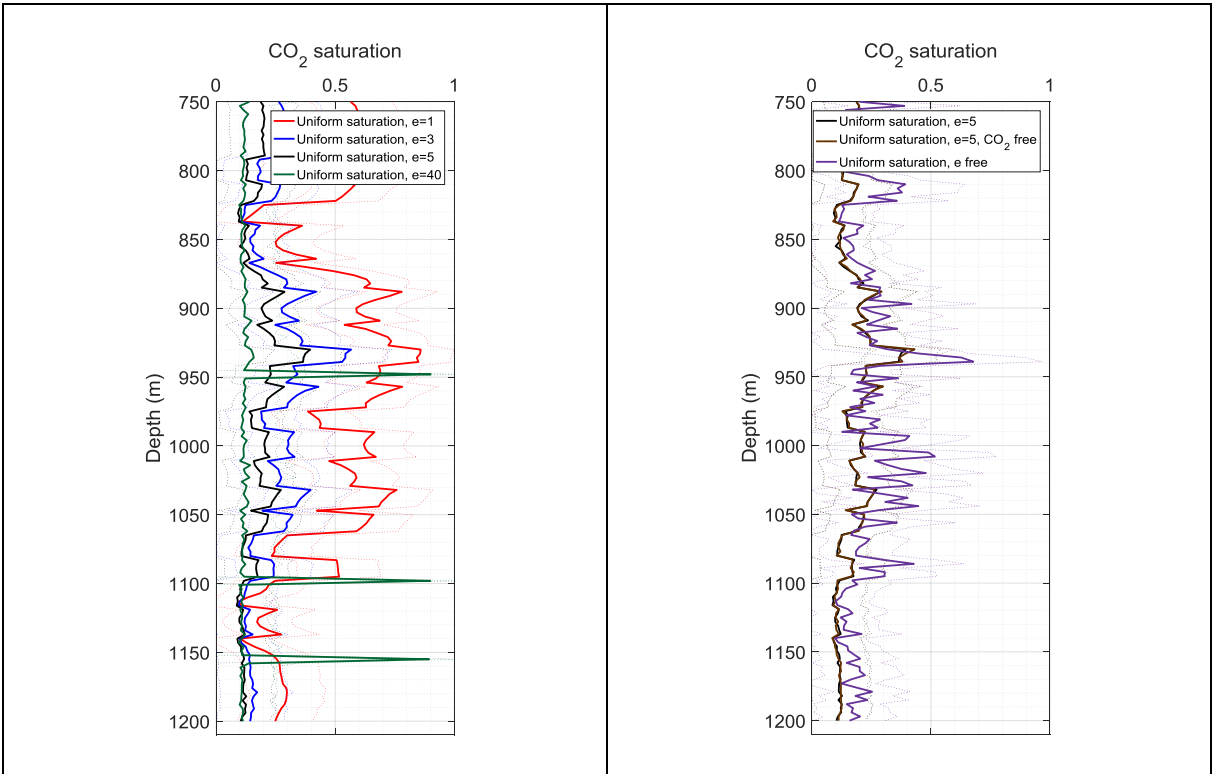

Figure 9-8. 1D estimation of CO_2 saturation using Brie rock physics model with different Brie exponent (left panel) and 1D estimation of CO_2 saturation using different rock physics models (right panel) for x = 2403 m (inside of plume). The dotted lines correspond to the mean value of estimation plus/minus uncertainty.
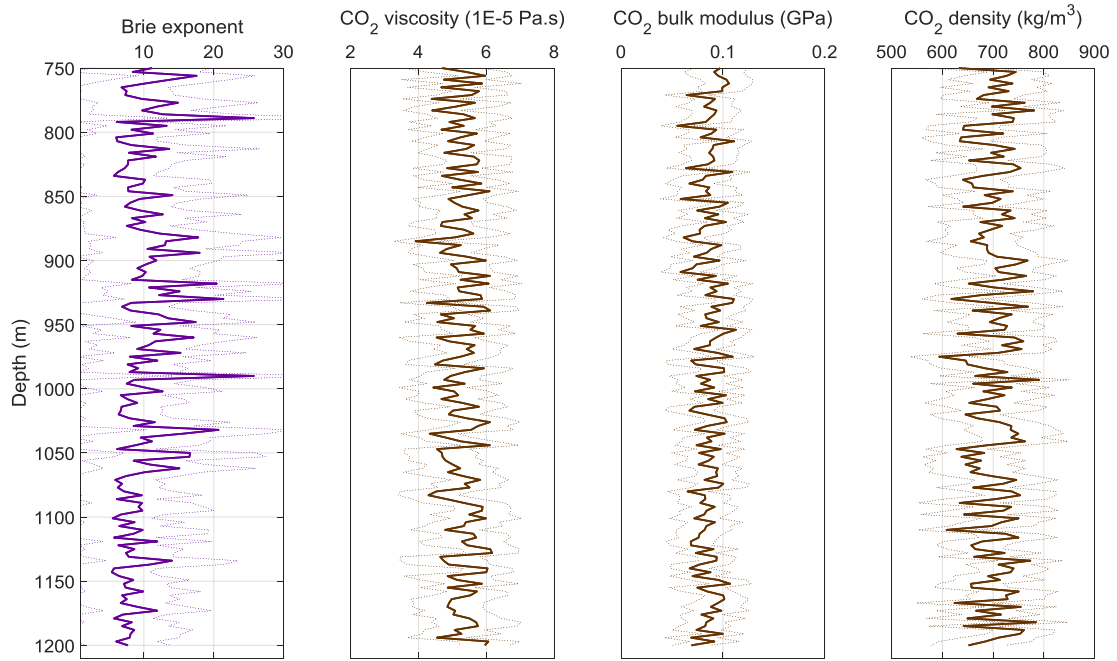
Figure 9-9. From left to right: 1D profile of Brie exponent and other CO₂ properties results (CO₂ viscosity, CO₂ bulk modulus, and CO₂ density) inverted jointly with the CO₂ saturation using different rock physics models for x = 2403 m (inside of plume). The dotted lines correspond to the mean value of estimation plus/minus uncertainty.
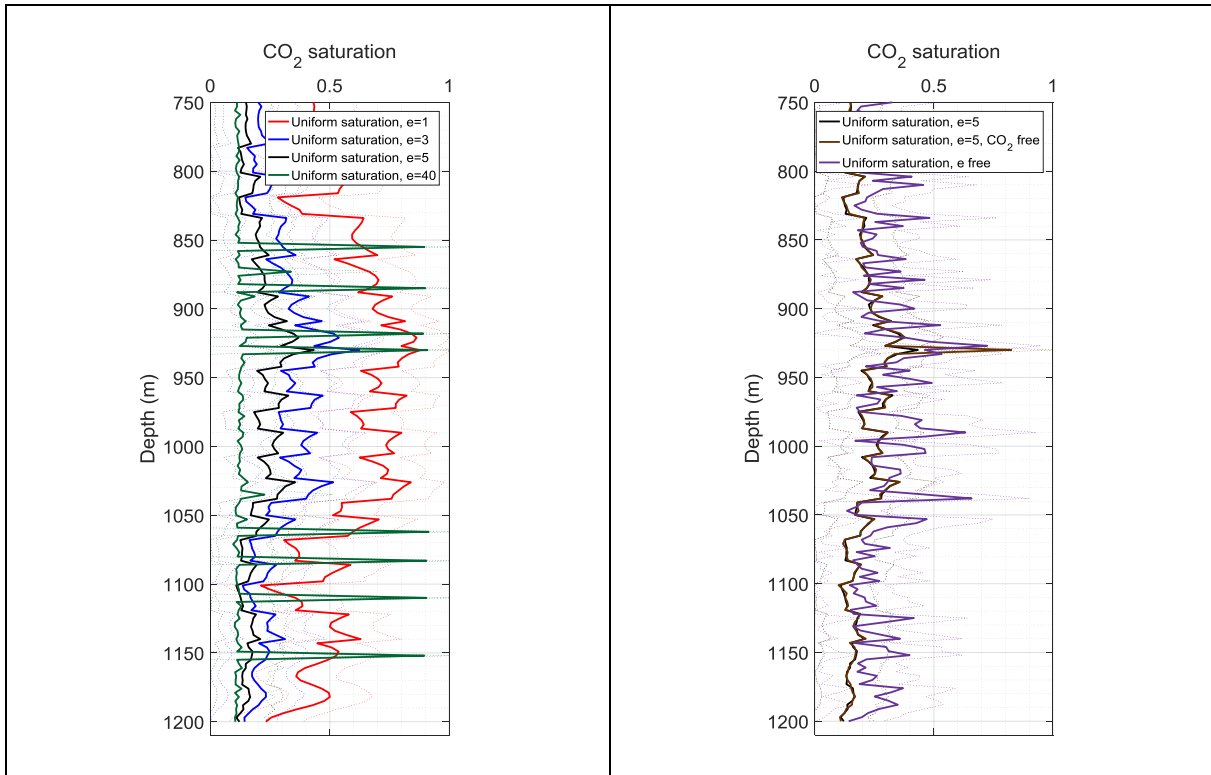
Figure 9-10. 1D estimation of CO₂ saturation using Brie rock physics model with different Brie exponent (left panel) and 1D estimation of CO₂ saturation using different rock physics models (right panel) for x = 2553 m (inside of plume). The dotted lines correspond to the mean value of estimation plus/minus uncertainty.

69
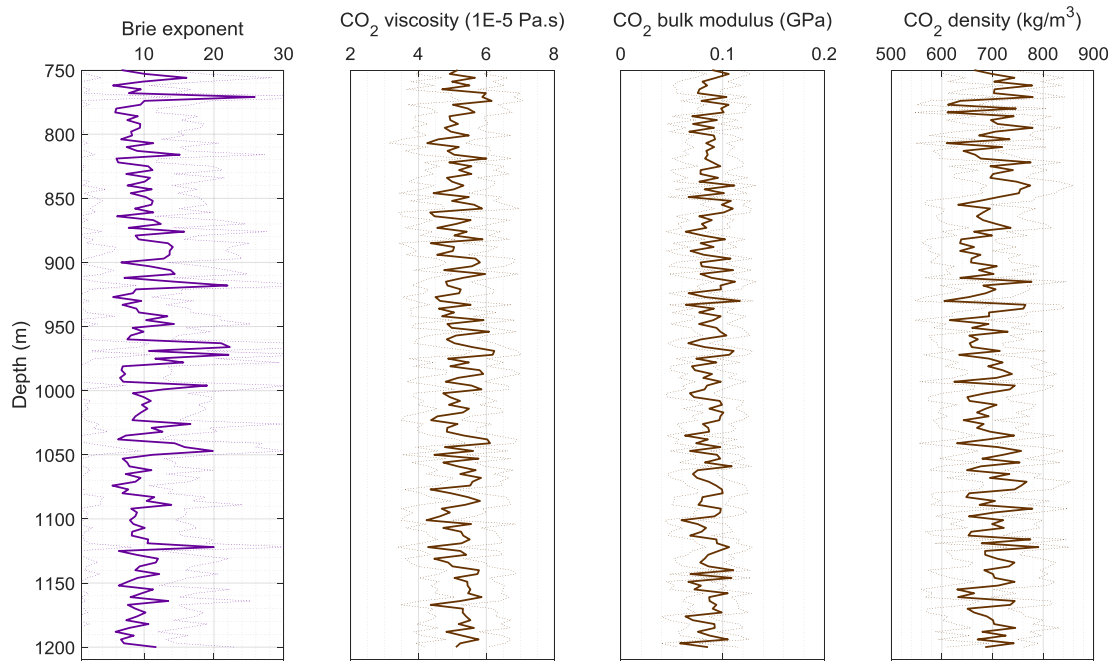
Figure 9-11. From left to right: 1D profile of Brie exponent and other CO₂ properties results (CO₂ viscosity, CO₂ bulk modulus, and CO₂ density) inverted jointly with the CO₂ saturation using different rock physics models for x = 2553 m (inside of plume). The dotted lines correspond to the mean value of estimation plus/minus uncertainty.
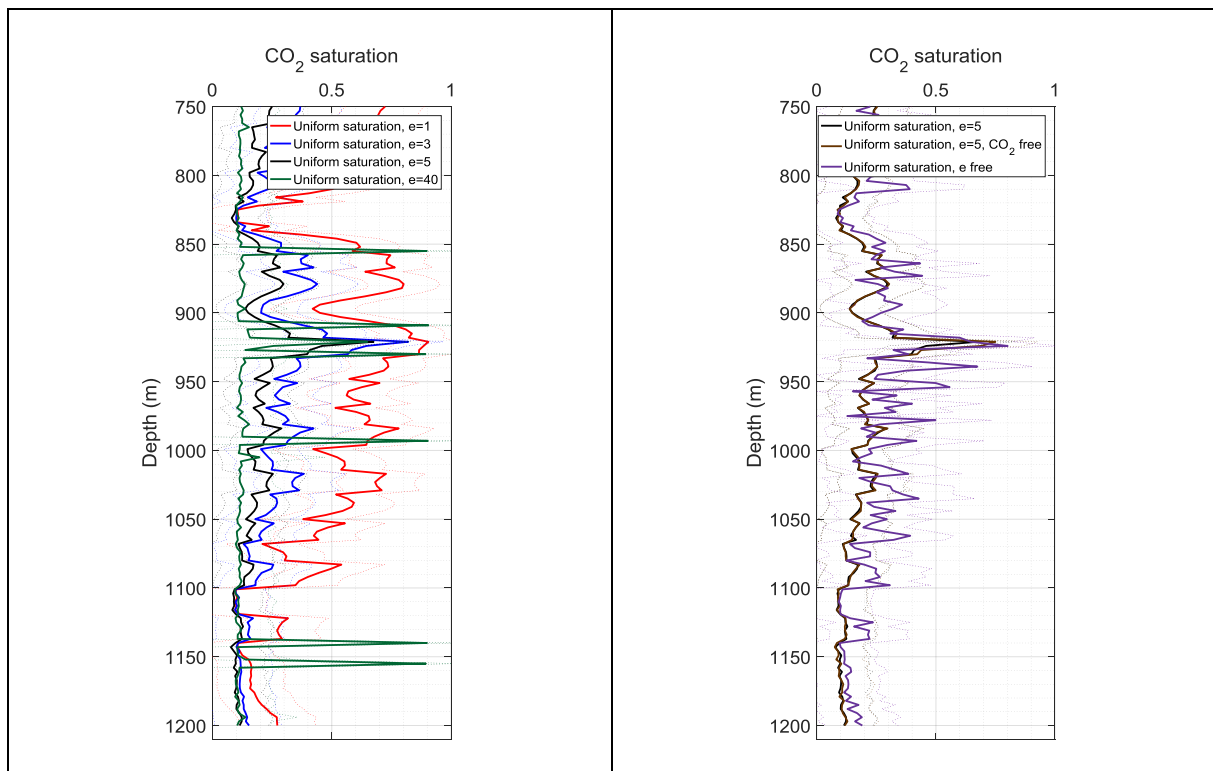
Figure 9-12. 1D estimation of CO₂ saturation using Brie rock physics model with different Brie exponent (left panel) and 1D estimation of CO₂ saturation using different rock physics models (right panel) for x = 3453 m (inside of plume). The dotted lines correspond to the mean value of estimation plus/minus uncertainty.
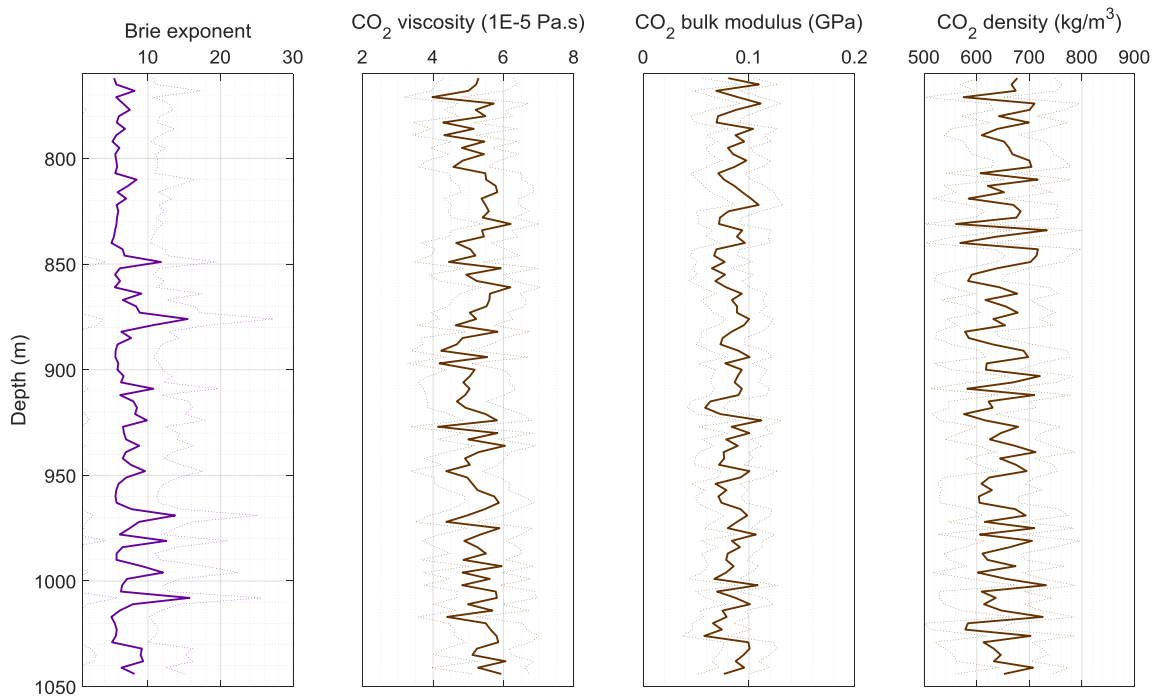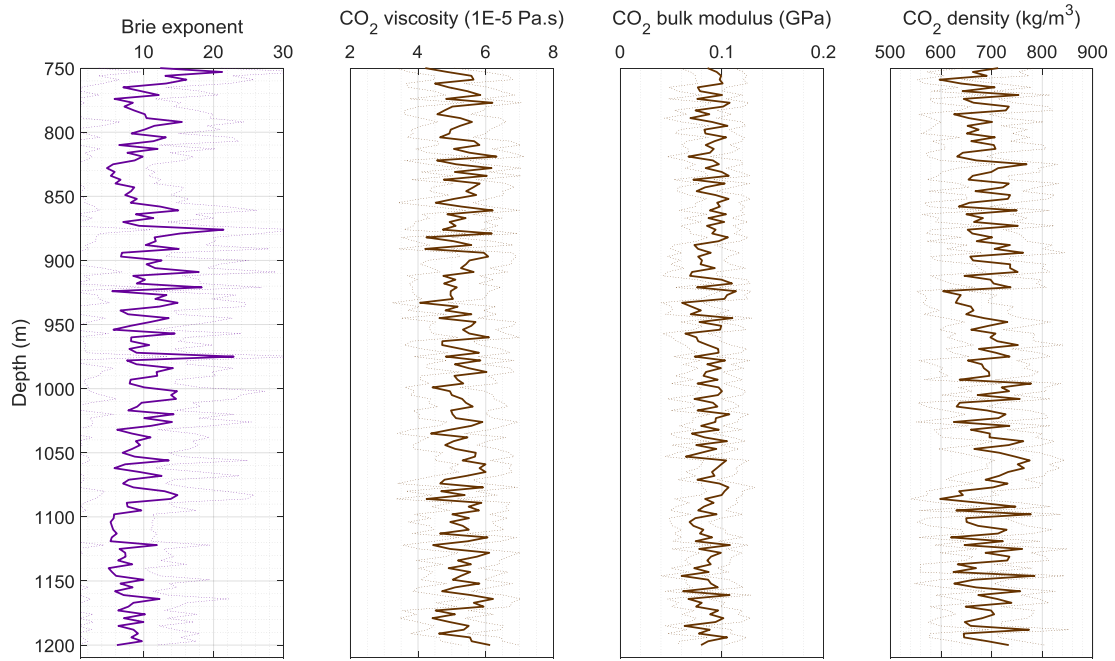
Figure 9-13. From left to right: 1D profile of Brie exponent and other CO₂ properties results (CO₂ viscosity, CO₂ bulk modulus, and CO₂ density) inverted jointly with the CO₂ saturation using different rock physics models for x = 3453 m (inside of plume). The dotted lines correspond to the mean value of estimation plus/minus uncertainty.
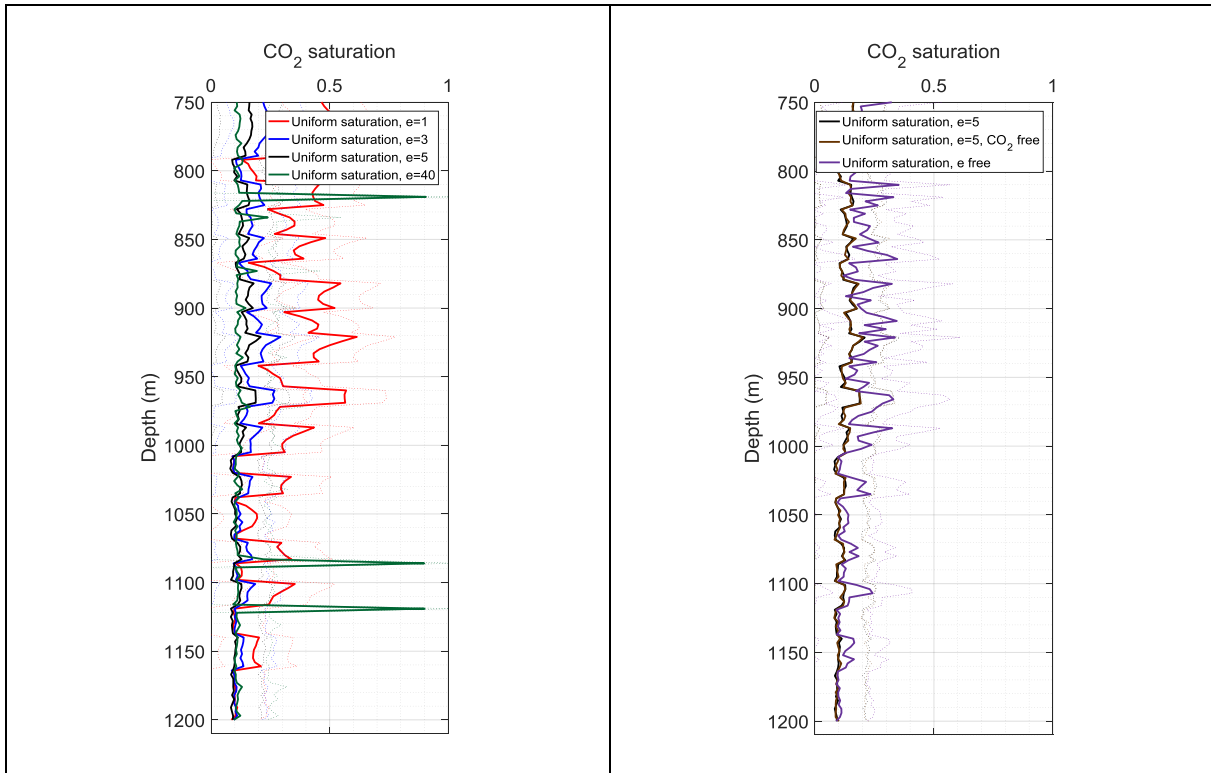
Figure 9-14. 1D estimation of CO₂ saturation using Brie rock physics model with different Brie exponent (left panel) and 1D estimation of CO₂ saturation using different rock physics models (right panel) for x = 1803 m (outside of plume). The dotted lines correspond to the mean value of estimation plus/minus uncertainty.

71

10 DISCUSSION

From all the studies, we can conclude that the uncertainties of CO_2 saturation are ranging around 0.1 - 0.2 for Brie rock physics model with e = 5 including the case with undefined CO_2 properties. When we invert the CO_2 saturation and Brie exponent simultaneously, the uncertainties of CO_2 saturation increase to around 0.3. Because we only have one input data (P-wave velocity), we can expect better estimation of CO_2 saturation when we have more information (Dupuy et al., 2016; Yan, 2016). The additional inputs will help the estimation when other parameters as Brie exponent, CO_2 bulk modulus are inverted jointly with CO_2 saturation, especially P-wave quality factor and S-wave velocity (Yan, 2016).

For the inline 1881, we show the two-step workflow as: first, estimate the frame properties from log data, and then, we estimate the CO_2 saturation using the log frame properties as a priori input. The baseline derived information from the log data is about 2 km away from the injection point and with a high sonic frequency, which can induce an inconsistency with the seismic monitor data of inline 1881. To minimize the uncertainty, we smooth the sonic data. While this smoothing may involve another risk in smearing out the lithology information. Instead of smoothing and extending horizontally, we might use the log data information and interpolate it based on the lithology variation. However, the created layers (as used for inline 1838) would be another source of uncertainties, which could be included in the further research work. We have a quite low estimation of CO_2 saturation around 20 to 60% for inline 1881, which is lower compared with some other existed studies at Sleipner (Chadwick and Noy, 2010; Savioli et al., 2017). There are several reasons for this low saturation estimation. First, the 2D section corresponding to inline 1881 is 533 m away from the injection point. Second, the FWI method tends to overestimate the velocity. For example, the P-wave velocity of the sandstone before CO_2 injection from log data (well 15/9-A16) ranges from $2000 - 2100$ m/s while the P-wave velocity of the sandstone before CO_2 injection from the FWI of inline 1838 ranges from 2000 to 2200 m/s and up to 2400 m/s. This increased velocity could be due to the smearing effect and other limitations of the FWI method (Dupuy et al., 2017).

For the study performed on inline 1838 data, we change the two-step workflow as: first extract the frame moduli from FWI baseline results, and then, we estimate the CO_2 saturation after applying FWI to the monitor data and using the baseline information as a priori input. For the extraction of baseline information for inline 1838, the FWI results are smeared out and it is

difficult to resolve the shale sand interbedded layers. Therefore, the utilization of the extracted rock frame properties is not straightforward. In our study, we use an average value to represent the lithology variation. Including the lateral variations of the frame moduli in each layers can improve the a priori inputs. For the monitor data, the improved resolution benefited from the injected CO_2. But it is still difficult to resolve 1 m to 3 m thick shale layers. It could be due to the band-limited seismic wave, which cannot resolve the thin layers (Dejtrakulwong et al., 2010). The derived results suggest much higher CO_2 saturation for inline 1838 than that for inline 1881. The reason could be the better estimated frame properties when we using FWI data. The relation between the P-wave velocity and CO_2 saturation can also explain it. For example, the fully brine saturated case from FWI is corresponding to higher P-wave velocities. This lead to the higher estimation of CO_2 saturation for monitor data, which we think is more correct.

The estimation results in our study of CO_2 saturation within shale layers and sand layers outside of CO_2 accumulation never reach 0% CO_2 saturation. For example, the lowest CO_2 saturation we can see in the estimation of CO_2 saturation for inline 1838 is around 6%. There are several reasons for this phenomenon. First, the 'shale' that we see is not purely shale due to the resolution limitation of FWI. Second, the geological study shows that the sand layers in the Sleipner are interbedded with 1-3 m shale layers, which is under seismic resolution. At Sleipner, most of the CO_2 bearing layers are thin and subject to tuning effects (Arts et al., 2004b). This thin shale imbedded sequence can be also found in other CCS projects like Ketzin (Stenhouse, 2009). Therefore, we have a more homogeneous CO_2 distribution without a very high CO_2 saturation zone inside. Third, we show the mean estimation of the results instead of the model with lowest misfit. The CO_2 saturation can be 0% when we take into account the mean value with uncertainty. Some other issues and limitations in our study are listed as:

1. The uncertainties associated with the pressure effect should be discriminated from the fluid saturation change.
2. The frequency dependent fluid properties are difficult to investigate using only one frequency of 30 Hz. This may induce uncertainties induced by the frequency dispersion. For example, a higher P-wave velocity associated the same CO_2 saturation for a higher frequency.

We also compare our results with some other studies. Lumley et al. (2008) use the seismic data to monitor the CO_2 distribution as Sleipner. They conclude that the seismic tool can detect the CO_2 presentation but it is difficult to quantify the CO_2 saturation when it is larger than 10-30%.

Ravazzoli and Gómez (2014) emphasize several issues related to the feasibility of using seismic data and the influence of saturation transition zones. They suggest to use AVA to help the estimation of the state of CO_2 (Ravazzoli and Gómez, 2011). Sen et al. (2016) introduced a capillary pressure equilibrium theory in their study and they found that the CO_2 distribution at Sleipner is more uniform for high CO_2 saturation and more patch for low CO_2 saturation. In our study, we also found similar trends, i.e. that the Brie exponent is higher for CO_2 saturated layers, which is indicating a more uniform mixing phase. Ghosh et al. (2015) proposed a time-lapse method combined with a pressure-dependent differential effective medium (PDEM) theory. They conclude that the CO_2 is more patchy for the sand layers with mud layer capped and some is mixed more uniformly with brine. Zhang et al. (2014) suggested that the maximum limit of the CO_2 saturation is 89% from the relative permeability, while the CO_2 saturation from their model can reach up to around 87%. Chadwick and Noy (2010) shows an approach using history-matching simulations and 4D seismic data ad get even higher estimation of maximum CO_2 saturation of 98%. This is comparable with our application results in inline 1838, in which case the maximum CO_2 saturation can reach 90% - 93% $\pm$ 0.15 to 0.25.

11 CONCLUSIONS AND OUTLOOK

11.1 Conclusions

Our study shows a two-step workflow combining the use of a rock physics tool and the high-resolution estimations from FWI. The rock physics inversion is applied on different datasets including the synthetic data and real data for different vintages and 2D sections. We focus on the estimation of CO_2 saturation, considering the results derived in the sensitivity tests of this report (Yan, 2016). Some conclusions are given hereafter:

1. The application on synthetic data validates the feasibility the rock physics tool for the estimation of CO_2 saturation.
2. We use generic rock physics models, which may be more realistic and help to understand the mixture mechanism in the CO_2 storage process.
3. We provide a method to extract the baseline frame properties using P-wave velocity combined with S-wave velocity and density. We also show an approach using the P-wave velocity gradient to construct the a priori information of the reservoir.
4. We estimate the CO_2 saturation using only P-wave velocity from FWI. The uncertainty related to the CO_2 saturation estimation is usually low.
5. The extended White's model (patchy saturation) does not work well on the estimation of CO_2 saturation due to the validity range limited to very high or low saturations.
6. We provide a way to evaluate the uncertainty using the mean estimation including all the models with misfit lower than a certain value.
7. The uncertainty is higher for higher CO_2 saturations. In the case of inline 1838, we obtain high CO_2 saturation (up to around 90% $\pm$ 0.15 - 0.25). We show that the undefined CO_2 properties is not crucial for the estimation of CO_2 saturation.
8. The Brie exponent is varying from 5 to 25 for the CO_2 saturated layers. This indicates that the brine and CO_2 mixture distribution is not fully patchy (e = 1) nor fully uniform (e = 40) mixing.

11.2 Further work

In our studies, we show the quantitative estimation of CO_2 saturation by the combination of FWI and RPI. The rock physics inversion results are dependent on the resolution of the FWI

results and are limited to acoustic approximation in our case. Using higher frequencies in FWI (if such frequency content is present in the data) and multi-parameter FWI can help to better constrain the RPI step. We expect to use FWI to estimate more information (such as P-wave quality factor and S-wave velocity) to give a better constrain on estimation of CO_2 saturation and other properties (Dupuy et al., 2017; Yan, 2016). The impact of the pressure change after CO_2 injection and the impact on the frame properties need to be considered carefully, even if the pressure effects should be limited at Sleipner. In addition, the in-situ properties of CO_2 in the reservoir can affect the CO_2 saturation results. Therefore, it can be meaningful to consider the in-situ CO_2 saturation and monitor the change of frame moduli. In addition, capillary pressure (Santos* et al., 2014) and the injected volume of CO_2 can help the understanding of the CO_2 Capture and Storage process.

12 REFERENCES

Adler, P. M., C. G. Jacquin, and J. F. Thovert, 1992, The formation factor of reconstructed porous media: Water Resources Research, v. 28, p. 1571-1576.

Alnes, H., O. Eiken, S. Nooner, G. Sasagawa, T. Stenvold, and M. Zumberge, 2011, Results from sleipner gravity monitoring: Updated density and temperature distribution of the CO2 plume: Energy Procedia, v. 4, p. 5504-5511.

Arts, R., A. Chadwick, and O. Eiken, 2004, Recent time-lapse seismic data show no indication of leakage at the Sleipner CO2-injection site: Proceedings of the 7th International Conference on Greenhouse Gas Technologies (GHGT-7), p. 653-662.

Arts, R., A. Chadwick, O. Eiken, S. Thibeau, and S. Nooner, 2008, Ten years' experience of monitoring CO2 injection in the Utsira Sand at Sleipner, offshore Norway: First break, v. 26.

Bergmann, P., and A. Chadwick, 2015, Volumetric bounds on subsurface fluid substitution using 4D seismic time shifts with an application at Sleipner, North Sea: Geophysics, v. 80, p. B153-B165.

Bickle, M. J., 2009, Geological carbon storage: Nature Geoscience, v. 2, p. 815-818.

Biot, M. A., 1956a, Theory of propagation of elastic waves in a fluid-saturated porous solid. I. Low-frequency range: The Journal of the acoustical Society of america, v. 28, p. 168-178.

Biot, M. A., 1956b, Theory of propagation of elastic waves in a fluid-saturated porous solid. II. Higher frequency range: the Journal of the Acoustical Society of America, v. 28, p. 179-191.

Boait, F., N. White, M. Bickle, R. Chadwick, J. Neufeld, and H. Huppert, 2012, Spatial and temporal evolution of injected CO2 at the Sleipner Field, North Sea: Journal of Geophysical Research: Solid Earth, v. 117.

Brie, A., F. Pampuri, A. Marsala, and O. Meazza, 1995, Shear sonic interpretation in gas-bearing sands: SPE Annual Technical Conference and Exhibition.

Brown, S., G. Bussod, and P. Hagin, 2007, AVO monitoring of CO 2 sequestration: A benchtop-modeling study: The Leading Edge, v. 26, p. 1576-1583.

Carcione, J. M., and S. Picotti, 2006, P-wave seismic attenuation by slow-wave diffusion: Effects of inhomogeneous rock properties: Geophysics, v. 71, p. O1-O8.

Carcione, J. M., S. Picotti, D. Gei, and G. Rossi, 2006, Physics and seismic modeling for monitoring CO2 storage: Pure and Applied Geophysics, v. 163, p. 175-207.

Castagna, J. P., M. L. Batzle, and R. L. Eastwood, 1985, Relationships between compressional-wave and shear-wave velocities in clastic silicate rocks: Geophysics, v. 50, p. 571-581.

Chadwick, R., S. Holloway, G. Kirby, U. Gregersen, and P. Johannessen, 2000, The Utsira Sand, Central North Sea–an assessment of its potential for regional CO2 disposal: Proceedings of the 5th International Conference on Greenhouse Gas Control Technologies (GHGT-5), Cairns, Australia, p. 349-354.

Chadwick, R., and D. Noy, 2010, History-matching flow simulations and time-lapse seismic data from the Sleipner CO2 plume: Geological Society, London, Petroleum Geology Conference series, p. 1171-1182.

Chadwick, R., P. Zweigel, U. Gregersen, G. Kirby, S. Holloway, and P. Johannessen, 2004, Geological reservoir characterization of a CO 2 storage site: the Utsira Sand, Sleipner, northern North Sea: Energy, v. 29, p. 1371-1381.

Dupuy, B., S. Garambois, and J. Virieux, 2016, Estimation of rock physics properties from seismic attributes — Part 1: Strategy and sensitivity analysis: GEOPHYSICS, v. 81, p. M35-M53.

Dupuy, B., A. Romdhane, P. Eliasson, E. Querendez, H. Yan, V. A. Torres, and A. Ghaderi, 2017, Quantitative seismic characterisation of CO2 at the Sleipner storage site, North Sea Interpretation, In press.

Dupuy, B., and A. Stovas, 2014, Influence of frequency and saturation on AVO attributes for patchy saturated rocks: GEOPHYSICS, v. 79, p. B19-B36.

Furre, A.-K., A. Kiær, and O. Eiken, 2015, CO2-induced seismic time shifts at Sleipner: Interpretation, v. 3, p. SS23-SS35.

Furre, A. K., and O. Eiken, 2014, Dual sensor streamer technology used in Sleipner CO2 injection monitoring: Geophysical Prospecting, v. 62, p. 1075-1088.

Gardner, G., L. Gardner, and A. Gregory, 1974, Formation velocity and density—The diagnostic basics for stratigraphic traps: Geophysics, v. 39, p. 770-780.

Gasda, S., H. Nilsen, and H. Dahle, 2012, Upscaled models for CO2 migration in geological formations with structural heterogeneity: ECMOR XIII-13th European Conference on the Mathematics of Oil Recovery.

Gassmann, F., 1951, Uber die elastizitat poroser medien: Verteljahrss-chrift der Naturforschenden Gesellschaft in Zurich, 96, 1–23: Translated to English in the 16th issue of Geophysics.

Gaus, I., M. Azaroual, and I. Czernichowski-Lauriol, 2005, Reactive transport modelling of the impact of CO 2 injection on the clayey cap rock at Sleipner (North Sea): Chemical Geology, v. 217, p. 319-337.

Ghaderi, A., and M. Landrø, 2009, Estimation of thickness and velocity changes of injected carbon dioxide layers from prestack time-lapse seismic data: Geophysics, v. 74, p. O17-O28.

Ghosh, R., M. K. Sen, and N. Vedanti, 2015, Quantitative interpretation of CO 2 plume from Sleipner (North Sea), using post-stack inversion and rock physics modeling: International Journal of Greenhouse Gas Control, v. 32, p. 147-158.

Han, D.-h., A. Nur, and D. Morgan, 1986, Effects of porosity and clay content on wave velocities in sandstones: Geophysics, v. 51, p. 2093-2107.

Hashin, Z., and S. Shtrikman, 1963, A variational approach to the theory of the elastic behaviour of multiphase materials: Journal of the Mechanics and Physics of Solids, v. 11, p. 127-140.

Institute, G. C., 2016, The Global Status of CCS: 2016 Summary Report.

Johnson, D. L., J. Koplik, and R. Dashen, 1987, Theory of dynamic permeability and tortuosity in fluid-saturated porous media: Journal of fluid mechanics, v. 176, p. 379-402.

Landrø, M., 2001, Discrimination between pressure and fluid saturation changes from time-lapse seismic data: Geophysics, v. 66, p. 836-844.

Landrø, M., and M. Zumberge, 2017, Estimating saturation and density changes caused by CO_2 injection at Sleipner—Using time-lapse seismic amplitude-variation-with-offset and time-lapse gravity: Interpretation.

Lindeberg, E., 2013, *in* C. Calculation of thermodynamic properties of CO_2, H_2O and their mixtures also including salt with the Excel macro ''CO2 Thermodynamics''. , ed., Trondheim, SINTEF.

Lumley, D., D. Adams, R. Wright, D. Markus, and S. Cole, 2008, Seismic monitoring of CO 2 geo-sequestration: realistic capabilities and limitations, SEG Technical Program Expanded Abstracts 2008, Society of Exploration Geophysicists, p. 2841-2845.

Mavko, G., T. Mukerji, and J. Dvorkin, 2009, The rock physics handbook: Tools for seismic analysis of porous media, Cambridge university press.

Meadows, M., 2008, Time-lapse seismic modeling and inversion of CO 2 saturation for storage and enhanced oil recovery: The Leading Edge, v. 27, p. 506-516.

Michael, K., A. Golab, V. Shulakova, J. Ennis-King, G. Allinson, S. Sharma, and T. Aiken, 2010, Geological storage of CO 2 in saline aquifers—a review of the experience from existing storage operations: International Journal of Greenhouse Gas Control, v. 4, p. 659-667.

Mora, P., 1987, Nonlinear two-dimensional elastic inversion of multioffset seismic data: Geophysics, v. 52, p. 1211-1228.

Norman, T., H. Alnes, O. Christensen, J. Zach, O. Eiken, and E. Tjåland, 2008, Planning time-lapse CSEM-surveys for joint seismic-EM monitoring of geological carbon dioxide injection: First EAGE CO2 Geological Storage Workshop.

Pratt, R. G., C. Shin, and G. Hick, 1998, Gauss–Newton and full Newton methods in frequency–space seismic waveform inversion: Geophysical Journal International, v. 133, p. 341-362.

Pratt, R. G., and M. Worthington, 1990, Inverse theory applied to multi-source cross-hole tomography. Part 1: Acoustic wave-equation method: Geophysical prospecting, v. 38, p. 287-310.

Pride, S., 2005, Hydrogeophysics: Water Science and Technology Library: Springer, p. 253–284.

Pride, S. R., J. G. Berryman, and J. M. Harris, 2004, Seismic attenuation due to wave-induced flow: Journal of Geophysical Research: Solid Earth, v. 109.

Ravazzoli, C. L., and J. L. Gómez, 2011, AVA seismic reflectivity analysis in carbon dioxide accumulations: Sensitivity to CO 2 phase and saturation: Journal of Applied Geophysics, v. 73, p. 93-100.

Ravazzoli, C. L., and J. L. Gómez, 2014, Seismic reflectivity in carbon dioxide accumulations: a review, CO2 Sequestration and Valorization, InTech.

Romdhane, A., and E. Querendez, 2014, CO2 characterization at the Sleipner field with full waveform inversion: Application to synthetic and real data: Energy Procedia, v. 63, p. 4358-4365.

Sambridge, M., 1999, Geophysical inversion with a neighbourhood algorithmöII. Appraising the ensemble: Geophys. J. Int, v. 138, p. 727-746.

Santos*, J. E., G. B. Savioli, L. A. Macias, J. M. Carcione, and D. Gei, 2014, Influence of capillary pressure on CO2 storage and monitoring, SEG Technical Program Expanded Abstracts 2014, Society of Exploration Geophysicists, p. 4971-4976.

Savioli, G. B., J. E. Santos, J. M. Carcione, and D. Gei, 2017, A model for CO2 storage and seismic monitoring combining multiphase fluid flow and wave propagation simulators. The Sleipner-field case: Computational Geosciences, v. 21, p. 223-239.

Sen, A., R. Ghosh, and N. Vedanti, 2016, Saturation estimation from 4D seismic data from Sleipner Field by a capillary pressure-based rock-physics model, SEG Technical Program Expanded Abstracts 2016, Society of Exploration Geophysicists, p. 3314-3321.

Shin, C., S. Jang, and D. J. Min, 2001, Improved amplitude preservation for prestack depth migration by inverse scattering theory: Geophysical prospecting, v. 49, p. 592-606.

Singh, V. P., A. Cavanagh, H. Hansen, B. Nazarian, M. Iding, and P. S. Ringrose, 2010, Reservoir modeling of CO2 plume behavior calibrated against monitoring data from Sleipner, Norway: SPE annual technical conference and exhibition.

Song, Z.-M., P. R. Williamson, and R. G. Pratt, 1995, Frequency-domain acoustic-wave modeling and inversion of crosshole data: Part II—Inversion method, synthetic experiments and real-data results: Geophysics, v. 60, p. 796-809.

Span, R., and W. Wagner, 1996, A new equation of state for carbon dioxide covering the fluid region from the triple-point temperature to 1100 K at pressures up to 800 MPa: Journal of physical and chemical reference data, v. 25, p. 1509-1596.

Tarantola, A., 1984, Inversion of seismic reflection data in the acoustic approximation: Geophysics, v. 49, p. 1259-1266.

Teja, A., and P. Rice, 1981, Generalized corresponding states method for the viscosities of liquid mixtures: Industrial & Engineering Chemistry Fundamentals, v. 20, p. 77-81.

Traub, B., 2008, 2ReMoVe - WP 3.4: Sleipner AVO study on synthetic Sleipner data, SINTEF Petroleumsforskning AS, SINTEF Petroleum Research.

Vernik, L., D. Fisher, and S. Bahret, 2002, Estimation of net-to-gross from P and S impedance in deepwater turbidites: The Leading Edge, v. 21, p. 380-387.

Virieux, J., and S. Operto, 2009, An overview of full-waveform inversion in exploration geophysics: Geophysics, v. 74, p. WCC1-WCC26.

White, D., 2013, Toward quantitative CO 2 storage estimates from time-lapse 3D seismic travel times: An example from the IEA GHG Weyburn–Midale CO 2 monitoring and storage project: International Journal of Greenhouse Gas Control, v. 16, p. S95-S102.

White, J., 1975, Computed seismic speeds and attenuation in rocks with partial gas saturation: Geophysics, v. 40, p. 224-232.

Yan, H., 2016, Rock Physics Inversion for CO2 Characterization at Sleipner: Sensitivity Tests and Baseline Application, Project Report, Trondheim, Norwegian University of Science and Technology.

Yan, H., B. Dupuy, A. Romdhane, and B. Arntsen, 2017a, Rock physics inversion for CO2 injection at Sleipner: 4th International Workshop of Rock Physics.

Yan, H., B. Dupuy, A. Romdhane, and B. Arntsen, 2017b, Rock Physics Inversion for CO2 Saturation Estimation at Sleipner-Sensitivity Tests and Baseline Application: 79th EAGE Conference and Exhibition 2017.

Zhang, G., P. Lu, and C. Zhu, 2014, Model predictions via history matching of CO2 plume migration at the Sleipner Project, Norwegian North Sea: Energy Procedia, v. 63, p. 3000-3011.

APPENDIX

Appendix A Supplementary notes of Sleipner well 15/9-A16

In this section, we show the estimation of frame moduli with a threshold of maximum misfit equal to 0.1 (Figure A- 1) and 10 (Figure A- 2). We found that the the mean estimations of frame properties are similar for using maximum misfit of 10 and 0.1. The discrepancy between the best estimation and the mean estimation using a misfit threshold of 10 are slightly bigger than that for the case using a misfit threshold of 0.1.
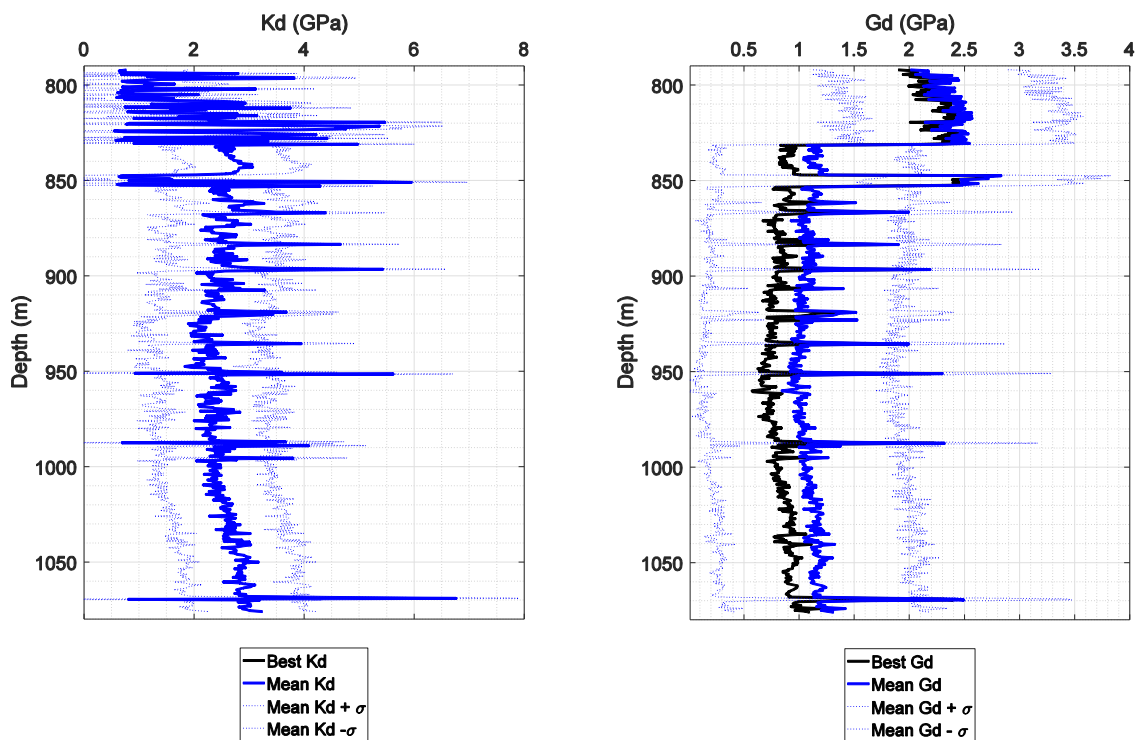
Figure A- 1. Estimation results of frame bulk modulus K_d (left) and frame shear modulus G_d (right) inverted by the inputs of P-wave velocity, S-wave velocity derived by Vernik's relation, and density log. The black lines correspond to the best estimation with lowest misfit. The blue lines correspond to the mean value of estimation with a maximum misfit of 0.1. The dotted lines correspond to the mean value of estimation plus/minus uncertainty.
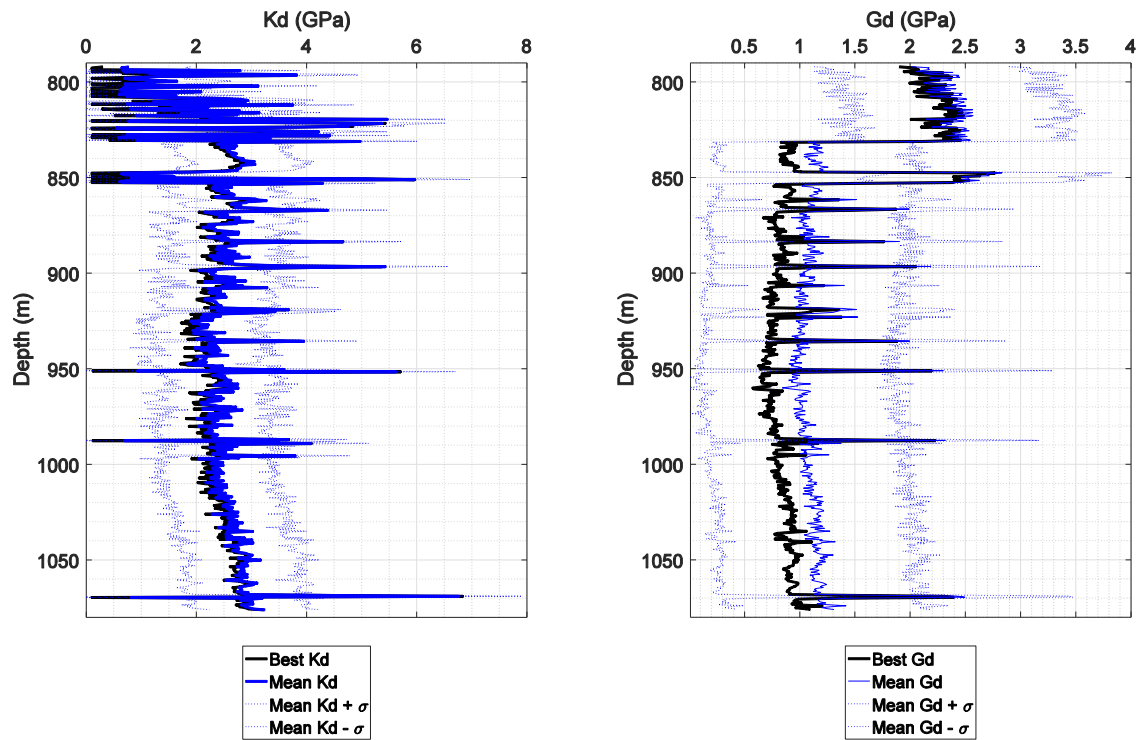
Figure A- 2. Estimation results of frame bulk modulus K_d (left) and frame shear modulus G_d (right) inverted by the inputs of P-wave velocity, S-wave velocity derived by Vernik's relation, and density log. The black lines correspond to the best estimation with lowest misfit. The blue lines correspond to the mean value of estimation with a maximum misfit of 10. The dotted lines correspond to the mean value of estimation plus/minus uncertainty.

Appendix B Supplementary notes of FWI synthetic model

I.   FWI process on the 2D FWI synthetic model

Table B- 1 shows the setting parameters for the FWI on the 2D synthetic data.

Table B- 1. The parameters used in the FWI tests.

Parameter	Value
Input files for FWI	P-wave velocity, quality factor, density
Sample number along Z direction	367
Sample number along X direction	1074
Grid size	3 m
pml thickness in grid points	2
pml coefficient	90
number of selected frequencies to be inverted	9
number of time steps	1250
time stepping	0.004 s
source wavelet file	fricker
maximum number of iteration per frequency	10
minimum velocity	1300

maximum velocity	2600
velocity above topography	1200
reference velocity	1700
compute diagonal terms of Hessian	Yes
model perturbation	2% for optimum step length

II.   Selection of iteration number

The iteration number is important for the accuracy of rock physics inversion. A proper iteration number can avoid unnecessary excessive computation. We compare the misfit variation versus different iteration number and conduct different tests with iteration number from 100 up to 1000 (Figure B- 1). The misfit values are tending to be stabilized when iteration number is 400 for all the rock physics models. Therefore, we decide to use an iteration number of 400 in our application of rock physics inversion.
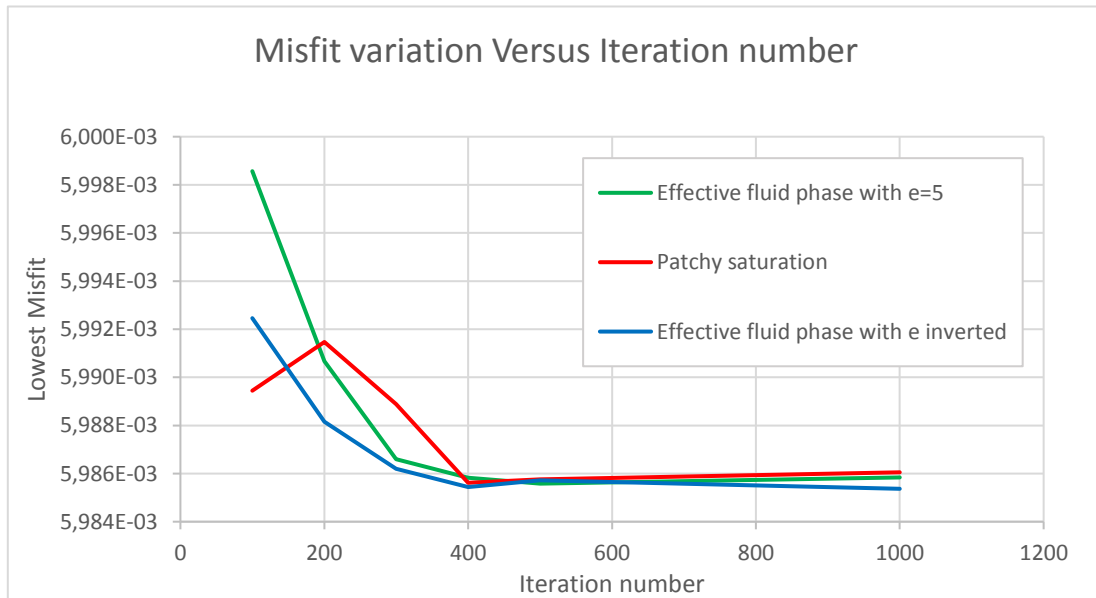
Figure B- 1.The misfit variation with various iteration numbers.

III.   Selection of FWI results

In this case, we use 1D derived frame properties from the Well 15/9-A16, which are smoothed and horizontally extended to 2D layered structure. We will show the rock physics inversion results using different P-wave velocity results using FWI test 1, 2 and 5. Here, we only show the results from uniform saturation with a Brie exponent e = 5.

Figure B- 2 shows estimation results of CO_2 saturation using the captured P-wave velocity model of FWI test 1 with a light smoothing along z direction. Figure B- 3 shows estimation results of CO_2 saturation using the captured P-wave velocity model of FWI test 2 with a strong smoothing along z direction. Figure B- 4 shows estimation results of CO_2 saturation using the captured P-wave velocity model of FWI test 5 with no smoothing applied. The estimation of CO_2 saturation from test 1 and 2 are similar (20% - 30%) within the CO_2 saturated layers. While CO_2 saturation from FWI test 5 gives higher CO_2 saturation and does not show the layer structure. All the estimations of CO_2 saturation from the tests have a similar uncertainty ranging from 0.1 to 0.15, and higher within the CO_2 saturated layers. In summary, the results of rock physics inversion are highly dependent on the quality of FWI results.
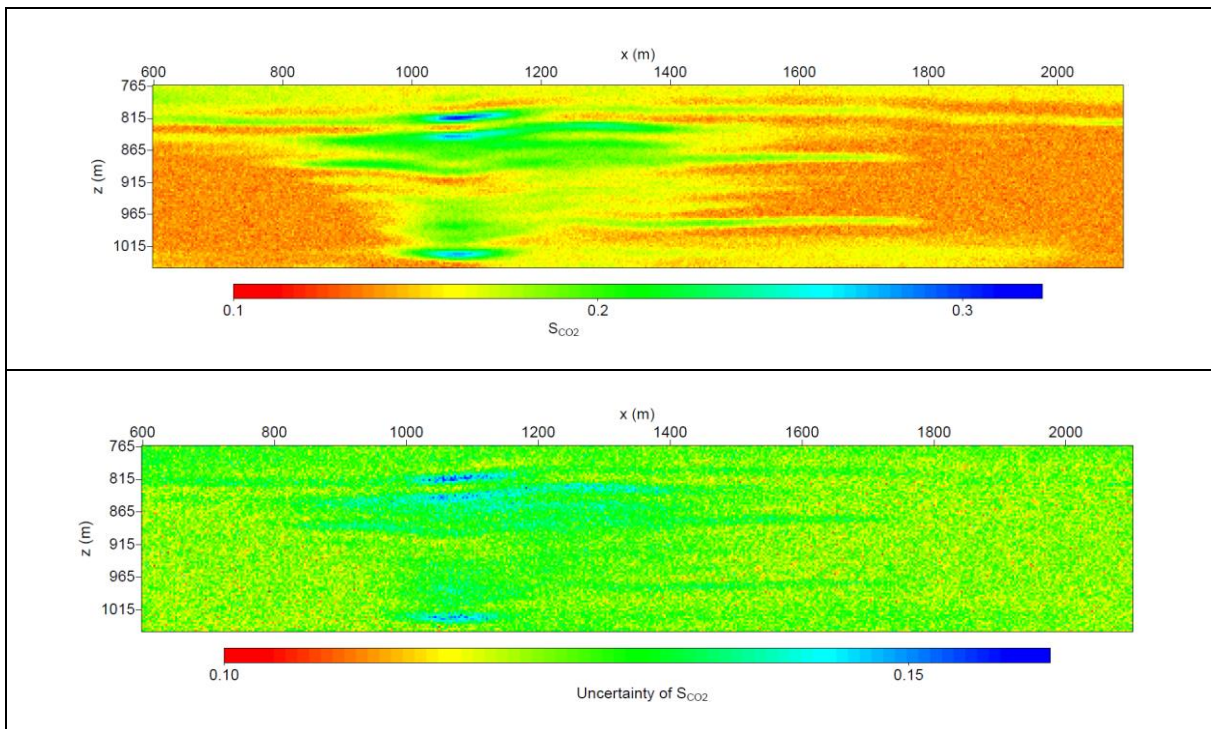
Figure B- 2. Estimation of CO_2 saturation (top panel) and uncertainty of CO_2 saturation (bottom panel) using Brie rock physics model with e = 5 and FWI result of test 1.
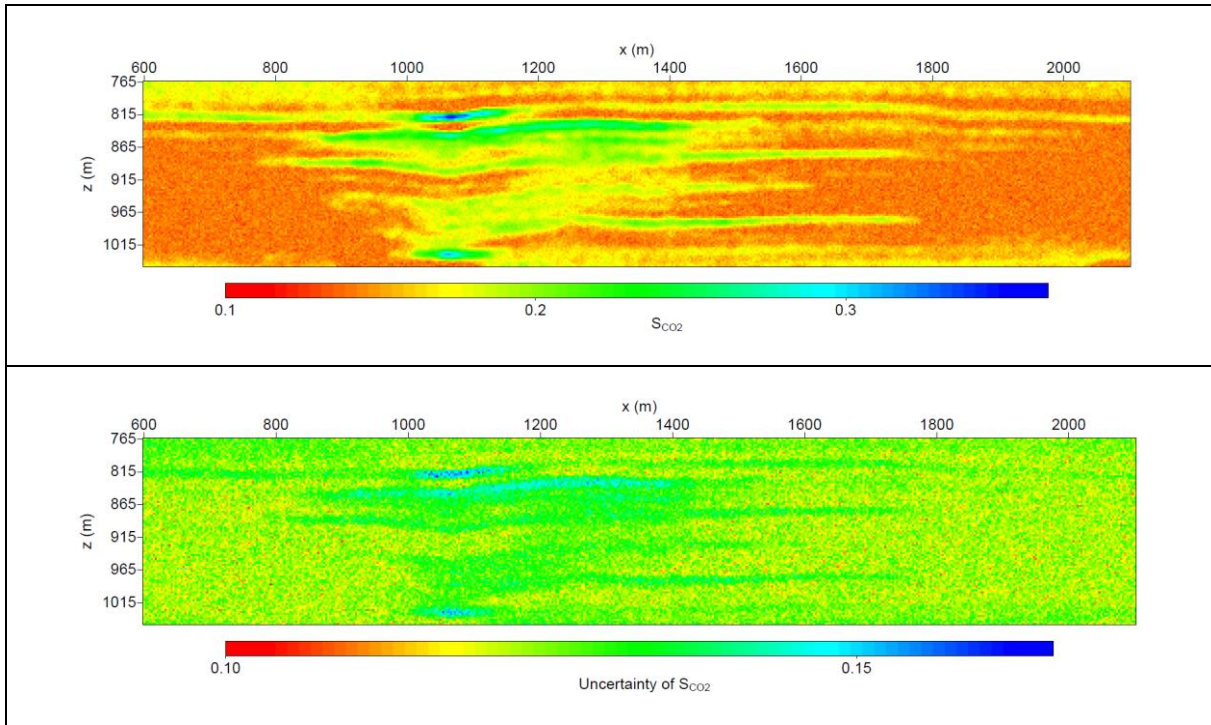
Figure B- 3. Estimation of CO₂ saturation (top panel) and uncertainty of CO₂ saturation (bottom panel) using Brie rock physics model with e = 5 and FWI result of test 2.
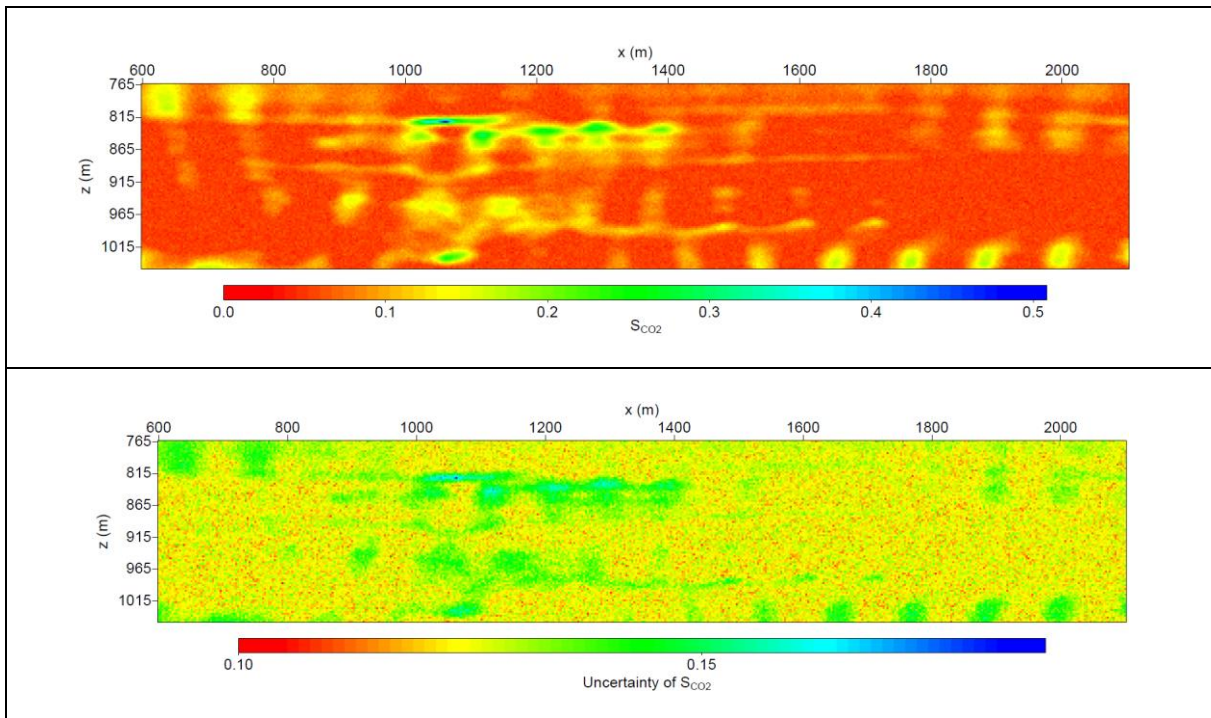
Figure B- 4. Estimation of CO₂ saturation (top panel) and uncertainty of CO₂ saturation (bottom panel) using Brie rock physics model with e = 5 and FWI result of test 5.

Appendix C Supplementary notes of real data (inline 1838, vintage 2008 and 1994).

This section is aimed at showing the processing steps and FWI tests of inline 1838.

I. Data processing procedure

Before the FWI, a basic processing procedure is applied using Seismic Unix on the raw data of inline 1838. We extract the data from 3D data set and try to rotate the data to a normal position in a 2D view. We outline the processing steps for inline 1838 of vintage 2008 in Table C- 1, including extracting guns, muting, rotating, transformation, and trace windowing, and so on. For inline 1838 of vintage 1994, we use similar processing steps.

Table C- 1. The processing steps applied prior to FWI.

Step	Processing workflow applied to the prestack dataset of inline 1838 of year 2008
1	Read the SEGY data
2	Extract the geometry information 'sx,sy,gx,gy' of the selected source No.1 and Receiver cable No.3
3	Mute the noises, sure as the first-arrival muting
4	Rotate the dataset with angle of 0.85 according the velocity cube
5	Translate the dataset and shift velocity cube to sy=0 and have smallest gx of data
6	Create the interval velocity from the RMS velocity data with the similar rotate, translation workflow
7	Resample the dataset (depth interval of 12.5 m) and apply the smooth factor in 3D (less smooth in the vertical direction)
8	Resample the sources and receivers corresponding to the velocity geometry, that the Y-axis ranges from 0 to 7 km

9	Do the amplitude corrections to the data (from 3D into 2D). Multiply the data by power of time (tpow=-2)
10	Apply Butterworth bandpass filtering
11	Top mute again to remove the filter induced noises
12	Scale the position unit from centimetre into meter by multiply 0.01
13	Offset selection with minimum offset equal to 420
14	Minimum to zero phase conversion
15	Data editing with reference to the given seismic source in the later FWI process
16	Create geometry profile (source depth of 6 m beneath the sea level, receiver depth of 8 m beneath the sea level)

The acquisition geometry of inline 1838 is given in Figure C- 1. Since the 2D inline data is extracted from a 3D dataset, the previous translation and rotation process of the data help to give a better 2D view. We can see that the 2D data is well processed with only smaller than 15 m crossline offset deviation.
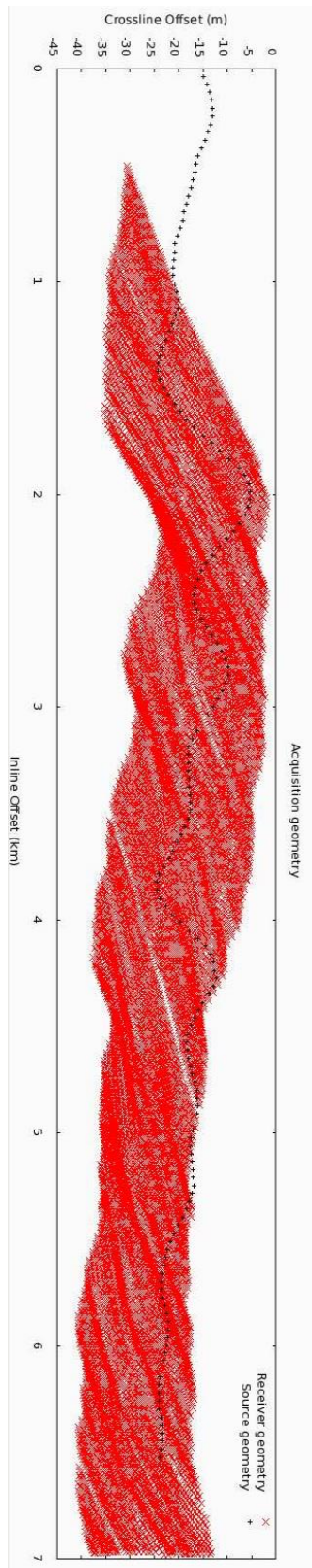
Figure C- 1. Acquisition geometry after the processing.

II. FWI tests

To prevent a large computation cost, we cut the deeper data and clip the interested region. The sources and the receiver at the boundary of the acquisition geometry are removed to minimise the boundary effects. The lateral variation of inline 1838 for vintage 2008 is from 0 m to 6980 m. The data is later shifted with adding a 30 m air layer to investigate the multiple created by the interface of air and water.

We generated the associated same size P-wave starting model, P-wave quality factor model, and density model. We consider a small attenuation. The quality factor is assumed with a constant number of 1000. We introduced the empirical density-velocity relations to derive the density information from P-wave velocity using Gardner relation for the reservoir section (Gardner et al., 1974). In addition, we add a constant water layer density which is equal to 1000 kg/m^3. We know that the air density is as low as 1.3 kg/m^3. However, for FWI, too low density will affect the inversion results. Therefore, we add an air layer with a constant density of 100 kg/m^3. Figure E- 1 shows the generated density file with the water and air layers. The smoothed velocity is derived by using a function of structure smoothing. We also add a water layer with a constant velocity of 1500 m/s and a 30 m air layer with a constant velocity of 330 m/s (see Figure 9-2).
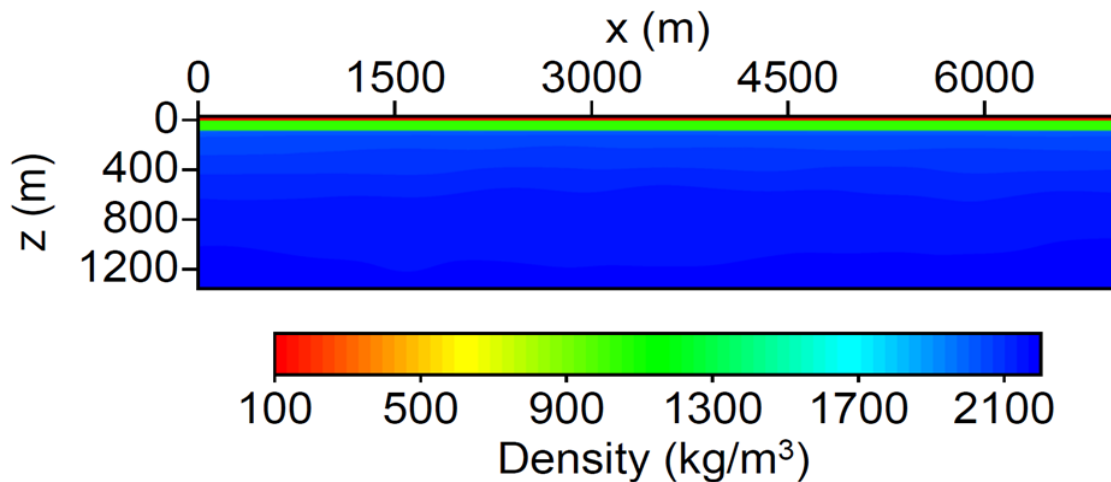
Figure E- 1. Density profile with a water layer and an air layer.

The FWI process performed from low to high frequencies. We use four tests with : 3 frequencies (10.0, 10.5, 11.0 Hz), 7 frequencies (11.5, 12.0, 12.5, 13.4, 15.2, 17.1, 19.6 Hz), 5 frequencies (22.0, 23.2, 24.4, 25.7, 26.9 Hz), and 5 frequencies (28.1, 29.3, 30.5, 31.8, 33.0 Hz), respectively. We use a smoothing factor equal to 0.3 for beginning three tests and a smaller smoothing

factor equal to 0.15 for the last test to minimize the misfit. Finally, we generate the final P-wave velocity model of 2008 vintage (inline 1838) as shown in Figure E- 2.
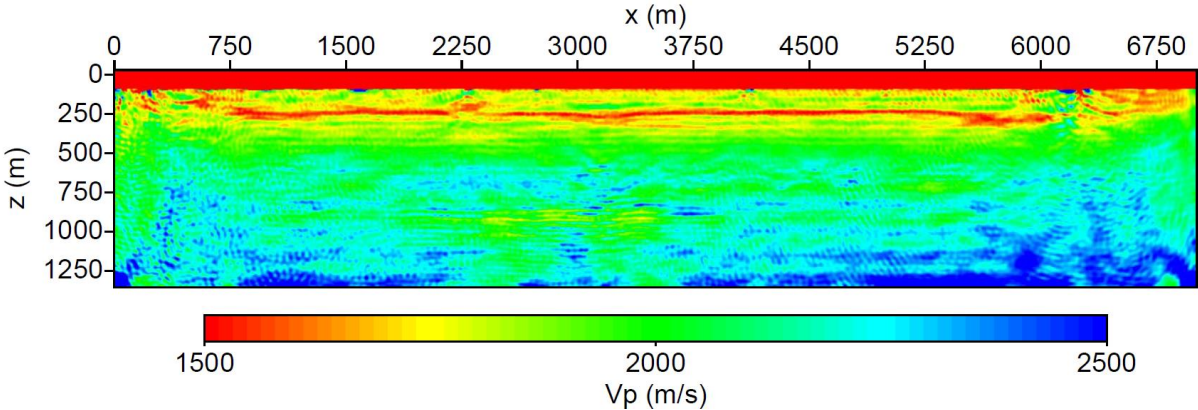
Figure E- 2. P-wave velocity model at last iteration of FWI (vintage 2008, inline 1838).

For real data of vintage 1994, we use a similar FWI procedure to derive the baseline P-wave velocity model as shown in Figure E- 3.
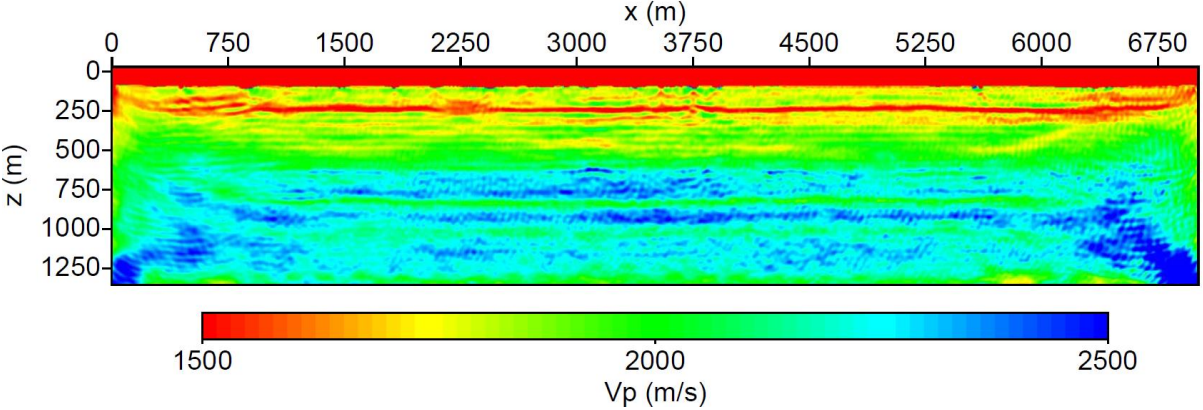
Figure E- 3. P-wave velocity model at last iteration of FWI (vintage 1994, inline 1838).

The FWI results are later smoothed to smear the oscillations before rock physics inversion (Figure 8-2, Figure 9-3).

Appendix D Grain bulk moduli and density computation for the Utsira sandstone

The sandstone properties are calculated with considering mineral compositions. The bulk modulus (K_S) and density (ρ_s) of each solid grain material are considered, as illustrated Table D- 1, Table D- 2, Table D- 3.

Table D- 1. Bulk modulus calculation illustration for the Utsira sandstone.

Minerals	K_S (GPa)		G_S (GPa)		Percentage
	Low bound	High bound	Low bound	High bound	
Quartz	36.5	37.9	44	45.6	75 %
Calcite	63.7	76.8	28.4	32	3 %
Feldspar	37.5	37.5	15	15	13 %
Albite	75.6	75.6	25.6	25.6	3 %
Aragonite	44.8	44.8	38.8	38.8	3 %
Mica (muscovite)	42.9	61.5	22.2	41.1	2 %
Mica (biotite)	41.1	59.7	12.4	42.3	2 %

This Hashin-Shtrikman bounds are illustrated by Hashin and Shtrikman (1963). K^{HS+} and G^{HS+} are corresponding to the upper bound with stiffer material forms the shell. K^{HS-} and G^{HS-} are corresponding to the lower bound with stiffer material forms the core. We use a more general form of the Hashin–Shtrikman–Walpole bounds, which can be applied to mixtures of more than two phases and is given by:

$$K^{HS+} = \Lambda(G_{max}), K^{HS-} = \Lambda(G_{min})$$
$$G^{HS+} = \Gamma(\zeta(K_{max}, G_{max})), \mu^{HS-} = \Gamma(\zeta(K_{min}, G_{min})).$$

(D-1)

Where K_{max} and G_{max} are the maximum bulk and shear moduli of the individual constituents. K_{min} and G_{min} are the minimum bulk and shear moduli of the constituents. $\Lambda(z)$, $\Gamma(z)$ and $\zeta(K,G)$ are given by:

$$\Lambda(z) = \left\langle \frac{1}{K(r) + \frac{4}{3}z} \right\rangle^{-1} - \frac{4}{3}z,$$

$$\Gamma(z) = \left\langle \frac{1}{G(r) + z} \right\rangle^{-1} - z,$$

(D-2)

$$\zeta(K,G) = \frac{G}{6}\left(\frac{9K + 8G}{K + 2G} \right).$$

Where the brackets $\langle . \rangle$ indicate an average over the medium, which is the same as an average over the constituents weighted by their volume fractions.

The K_S is obtained by averaging Hashin-Shtrikman bounds, as shown in Table D- 2.

Table D- 2. Ks is obtained by averaging Hashin-Shtrikman bounds.

K^{HS+} (GPa)	K^{HS-} (GPa)	K_S (GPa)
40.31	38.26	39.29

Table D- 3. The grain density of each constituent in the Utsira sandstone.

Minerals	$\rho_{s(i)}$ (g/cc)	Volume percentage (%)	ρ_s (g/cc)
Quartz	2.65	75 %	
Calcite	2.71	3 %	
Feldspar	2.62	13 %	
Albite	2.63	3 %	2.663
Aragonite	2.92	3 %	
Mica (muscovite)	2.79	2 %	
Mica (biotite)	3.05	2 %	

The grain density of the Utsira sandstone (ρ_s) is calculated by using volume-weighted density calculation method (Table D- 3).

Appendix E Supplementary table for the Nordland shale

In our studies, the mineralogy of the Nordland shale in volume percentage (as shown in Table E- 1) is exacted from the mineralogy in mass percentage by Gaus et al. (2005).

Table E- 1. Nordland shale rock mineralogy by Gaus et al. (2005).

Nordland shale composition	Mass percent
Plagioclase	12.3
Calcite	1.0
Quartz	21.5
Chlorite	4.1
Mica/Illite	24.7
Kaolinite	18.0
K-feldspar	2.1
Pyrite	2.8
Siderite	1.6
Smectite	8.8
Mixed layer clay	1.4
Total	98.3

Appendix F Analysis tables for sensitivity test results

In our sensitivity studies, the inversion estimation of fluid properties and saturation simultaneously can be concluded in the following tables. Since in geophysics, we always only obtain P-wave velocities for FWI results, we analysis the inversion tests especially for inversion from only V_P at first. Then, we analysis the other parameter effect for estimation of fluid properties.

Table F- 1. Results analysis for inversion for CO_2 properties at $S_W = 5\%$.

$S_W=5\%$, Patchy saturation	ρ_{fl2} Estimation	ρ_{fl2} Constrain misfit	K_{fl2} Estimation	K_{fl2} Constrain misfit	S_W Estimation	S_W Constrain misfit	η_2 Estimation	η_2 Constrain misfit	Comment
When estimated by only V_P	good		bad		very bad		very good		The best estimation of S_W is from V_P, V_S, ρ
ρ	+	+	+	+	\	\	\	\	
V_S	+	+	+	+	\	\	\	\ or +	
Q_P	\	\	\	\	\	\	\	\	
V_S, Q_S	\	\	\	\	\	\	\	\	

$S_W=5\%$, Uniform saturation	ρ_{fl2} Estimation	ρ_{fl2} Constrain misfit	K_{fl2} Estimation	K_{fl2} Constrain misfit	S_W Estimation	S_W Constrain misfit	η_2 Estimation	η_2 Constrain misfit	Comment
When estimated by only V_P	good		bad		very bad		good		Input group 3,7,8 give better estimation of S_W
ρ	+	+	+	+	+	\	\ or +	\	
V_S	+	+	+	+	\ or +	\	\	+	
Q_P	\	+	\ or +	+	+	\	\	+	
V_S, Q_S	\	\	\	\	\	\	+	\	

Table F- 2. Results analysis for inversion for CO_2 properties at $S_W = 20\%$.

$S_W=20\%$, Patchy saturation	ρ_{fl2} Estimation	ρ_{fl2} Constrain misfit	K_{fl2} Estimation	K_{fl2} Constrain misfit	S_W Estimation	S_W Constrain misfit	η_2 Estimation	η_2 Constrain misfit	Comment
When estimated by only V_P	good		bad		bad (relative error=21%)		bad		
ρ	+	+	+	+	\	\	+	\	
V_S	+	+	+	+	\	\	+	\	
Q_P	\	\	\	\	+	\	+	\	
V_S, Q_S	\	\	\	\	\	\	\	\	

$S_W=20\%$, Uniform saturation	ρ_{fl2} Estimation	ρ_{fl2} Constrain misfit	K_{fl2} Estimation	K_{fl2} Constrain misfit	S_W Estimation	S_W Constrain misfit	η_2 Estimation	η_2 Constrain misfit	Comment
When estimated by only V_P	good		bad (relative error=29%)		bad (relative error=37%)		bad		Input group 8 gives best estimation of S_W
ρ	+	+	+	+	\	\	\ or +	\	
V_S	+	+	+	+	\	\	\ or +	\	
Q_P	\ or +	\	\	\ or +	\	\	+	\	
V_S, Q_S	\	\	\	\	\ or +	\	+	\	

Table F- 3. Results analysis for inversion for CO_2 properties at $S_W = 85\%$.

$S_W=85\%$, Patchy saturation	ρ_{fl2}		K_{fl2}		S_W		η_2		Comment
	Estimation	Constrain misfit	Estimation	Constrain misfit	Estimation	Constrain misfit	Estimation	Constrain misfit	
When estimated by only V_P	good		bad (relative error=27.7%)		good		good		
ρ	\ or +	\	+	+	+	\	\	\	
V_S	\	\	\	+	\ or +	+	\	\	
Q_P	\	\	+	+	+	\	\	\	
V_S, Q_S	\	\	\	\	\	\	+	\	

$S_W=85\%$, Uniform saturation	ρ_{fl2}		K_{fl2}		S_W		η_2		Comment
	Estimation	Constrain misfit	Estimation	Constrain misfit	Estimation	Constrain misfit	Estimation	Constrain misfit	
When estimated by only VP	bad (relative error=20.6%)		bad		very good		good		All input groups give good estimation of S_W. Uniform saturation gives better estimation than that in Patchy saturation.
ρ	+	+	+	\	\ or +	\	\	+	
V_S	+	\ or +	+	\	\ or +	\	\	\	
Q_P	+	\	+	\	\ or +	+	\	\	
V_S, Q_S	\	\	\	\	\	\	+	\ or +	

Where:

\ is indicating that there is no obvious impact or relation.

+ is indicating a positive effect in estimation or constraining the misfit.

Good estimation is indicating the relative error < 20%.

Bad estimation is indicating the relative error > 20%.

And input groups are given as:

1. Only P-wave velocity (V_P);
2. P- and S-wave velocities (V_P, V_S);
3. P- wave velocity and density (V_P, ρ);
4. P- and S-wave velocities and density (V_P, V_S, ρ);
5. P- wave velocity and quality factor (V_P, Q_P);
6. P-wave velocity, quality factor, and density (V_P, Q_P, ρ);
7. P- and S-wave velocities and quality factors (V_P, V_S, Q_P, Q_S);
8. P- and S-wave velocities, quality factors, and density (V_P, Q_P, V_S, Q_S, ρ).

The misfit under the lower brine saturation (higher CO_2 saturation) condition is larger than that for high brine saturation (lower CO_2 saturation). We may conclude that for low brine saturation (high CO_2 saturation) it is more difficult to invert the CO_2 properties.

Rock Physics Inversion for CO_2 Saturation Estimation at Sleipner - Sensitivity Tests and Baseline Application

Tu P8 01

Rock Physics Inversion for CO2 Saturation Estimation at Sleipner - Sensitivity Tests and Baseline Application

H. Yan* (SINTEF Petroleum Research; NTNU), B. Dupuy (SINTEF Petroleum Research), A. Romdhane (SINTEF Petroleum Research), B. Arntsen (Norwegian University of Science & Technology)

Summary

We demonstrate the use of rock physics inversion for estimating CO2 saturation and rock frame properties at the Sleipner CO2 storage pilot in the North Sea. We investigate the relation between rock physics properties and elastic attributes for the Utsira unconsolidated sandstone. An effective fluid phase plugged into Biot theory is used together with the Brie mixing theory for the calculation of effective bulk modulus. We use the estimated viscoelastic properties under different brine and CO2 distributions to invert selected poroelastic parameters from various input data parametrizations. By analysis of the sensitivity tests, we can conclude that CO2 saturation can be well estimated from only VP input, especially for high brine saturation. The quality factors of both P-wave and S-wave velocities help better estimate CO2 saturation and reduce the uncertainties. In a second part, the method is applied to well log data acquired prior to CO2 injection. The S-wave velocities are derived using empirical relations from the P-wave velocities and density and used to estimate the rock frame moduli of the Utsira sand before CO2 injection. We found that the S-wave velocities are crucial to help the estimation of frame moduli.

Introduction

Nowadays, CO_2 Capture and Storage (CCS) is acknowledged as a potential mean of reducing the CO_2 emissions into the atmosphere and therefore mitigating global warming. Understanding the relationship between seismic velocities and the porous rocks is important to characterize the changes of the subsurface properties during the CO_2 injection process. In this work, we propose a methodology to study the changes of rock physics properties during the injection of CO_2 at the Sleipner storage site in the North Sea. 4D time-lapse seismic methods can estimate the changes in reservoir and saturating fluid properties. However, most of these methods are highly dependent on the repeatability of the seismic survey (Landrø, 2001, Arts et al., 2008, Arts et al., 2004). Amplitude versus offset (AVO) analysis can be more sensitive to changes in reservoir in particular when shear wave velocity information is considered (Castagna et al., 1985). Such information is however difficult to obtain accurately for most high-porosity, high-permeability rocks. To overcome the limitations of previous studies and obtain reliable reservoir properties, a two-step workflow based on a combination of Full Waveform Inversion (FWI) and rock physics inversion was developed and applied by Dupuy et al. (2016a). In this work, we focus on sensitivity tests to get accurate estimations of CO_2 saturation. We calculate seismic viscoelastic properties (density, quality factor, velocities) with rock physics forward modelling. Then, the rock physics inversion is performed under different saturation conditions. We also use the workflow to invert the drained reservoir frame properties before CO_2 injection by using well log data of the Utsira sand formation.

Rock physics model and inversion

We define effective fluid properties using Brie mixing equation for fluid bulk modulus (Brie et al., 1995), Teja and Rice (1981) relation for effective viscosity and weighted arithmetic average for effective fluid density. The effective fluid phase is then plugged in the extended Biot theory (Pride, 2005) to describe the poroelastic material partially saturated with brine and CO_2. The exponent e of the Brie equation ranges between 1 and 40 (Brie et al., 1995). Hereafter, we use a value of 5 (Carcione et al., 2006) for CO_2 and brine mixture. From the description of microscopic properties (mineral grains, fluid phases, rock frame), the rock physics model constitutes the forward model and allows to compute viscoelastic properties. The idea in the rock physics inversion process is to extract the poroelastic parameters from seismic attributes (velocity, quality factor, density) combinations. The forward problem can be formulated as:

$$\vec{d} = g(\vec{m}).\tag{1}$$

Where $\vec{d}$, $\vec{m}$ and g denote the data vector, the model vector and the nonlinear relation function linking the data and model (i.e. the rock physic model), respectively. The solution of associated problem requires the use of an optimization method. In our case, the Neighborhood Algorithm (NA) described in Sambridge (1999) is used to solve the inverse problem. The method is searching for the global minimum misfit over the model domain randomly. Only two control parameters are necessary to use the NA algorithm method, which are the number of models generated in each iterations and the resampling size of Voronoï cells. The discrepancy between the observed data (viscoelastic properties derived from input data) and calculated data (viscoelastic data computed from the rock physics properties by forward modelling) is described by a misfit function following the L2 norm. After each iteration, the resampling of the model space is done according to the misfit values of each model. In our sensitivity tests, 1000 iterations are used and a resampling factor of 10 is used. In the application on baseline log data, the iteration number is reduced to 500 with regard to computation cost and time.

Sensitivity Tests

The Sleipner storage pilot is located in the North Sea. The CO_2 separated from the produced gas is stored into the Utsira Sandstone at 800 m below the sea bottom (Carcione et al., 2006). Some a priori parameters for the Utsira Fm are partly provided in Lindeberg (2013), and others are extracted based on the existing papers on Sleipner field. We assume a central frequency of 30 Hz for the seismic data

with an initial temperature of 37°C (Furre et al., 2015, Furre and Eiken, 2014) for the sensitivity tests. We obtain the seismic attributes (velocity, density, quality factor) by forward modelling. For the inversion, we use different combinations of input data. **Figure 1** shows the inversion results of brine saturation S_W considering low CO_2 saturation ($S_W = 85\%$) and high CO_2 saturation ($S_W = 20\%$). If only V_P is provided, the estimation of S_W is poor with wide low misfit area for the low brine saturation case (**Figure 1** (b)). The estimation of S_W is better in case of high brine saturation (**Figure 1** (a)). S_W is better estimated when more than only V_P data is provided (**Figure 1** (c, d, e, f)). It can be seen that the combination of (V_P, V_S and ρ) input can make the estimated best model be well matched with the true model (**Figure 1** (f)). The low misfit area is better constrained when the parametrization includes quality factors (**Figure 1** (d)). We conclude that the estimation of CO_2 saturation is correct from V_P data but requires additional input if the brine saturation is low. In addition, other sensitivity tests have been carried out in less optimal cases (if the rock physics model describing is not perfectly known and if the CO_2 properties are not defined) and suggest that the use of additional input data, especially V_S and Q_P are required to get good estimation of CO_2 saturation.
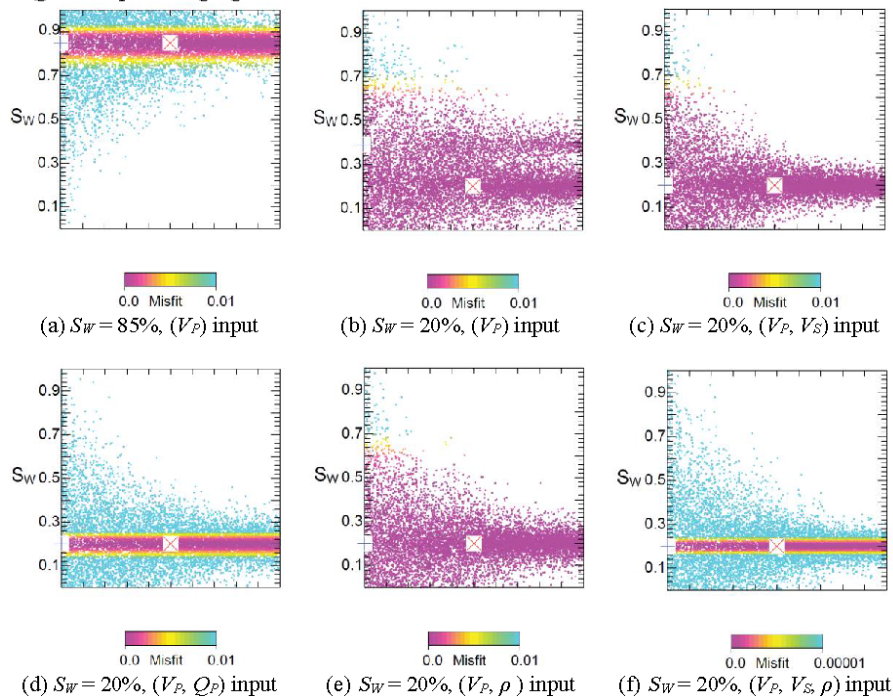

(a) $S_W = 85\%$, (V_P) input   (b) $S_W = 20\%$, (V_P) input   (c) $S_W = 20\%$, (V_P, V_S) input

(d) $S_W = 20\%$, (V_P, Q_P) input   (e) $S_W = 20\%$, (V_P, ρ) input   (f) $S_W = 20\%$, (V_P, V_S, ρ) input

Figure 1 *Estimation of brine saturation S_W using from input data: (a, b) V_P input, (c) V_P and V_S input, (d) V_P and Q_P input, (e) V_P and ρ input, (d) V_P, V_S and ρ input. Panel a is for brine saturation $S_W = 85\%$, while panels b, c, d, e and f are for brine saturation $S_W = 20\%$. The blue cross indicates the best model and the red cross indicates the true model. The colour of each dot represents the misfit value for each computed model (between 0 and 1% or 0.001%).*

Rock frame properties estimation using baseline log data

To extract the baseline properties of the Utsira sand rock frame before CO_2 injection, we apply our rock physics model for porous medium with only one fluid phase (brine) saturating the pore space. The data were recorded at Well 15/9-16 before the CO_2 injection started. Conventional petrophysics information is provided by this well data, for instance, gamma-ray, density, porosity and compressional sonic log data. The target area in our study corresponds to the depth range 770 m-1000

m. The 250 m thick Utsira sandstone is surrounded by the Nordland shale at the top and the Hordaland shale at the bottom. There are several thin shale layers imbeded in the Utsira sandstone (Zweigel, 2000).

Sensitivity tests show that S-wave velocity is crucial for the frame moduli estimation (Dupuy et al., 2016b). Consequently, we compute empirically S-wave sonic velocity using the empirical Vernik's relation (Mavko et al., 2009). We carry out the inversion with estimation of dry frame moduli (K_d and G_d) and the inversion is applied to the whole log data. P- and S-wave velocities and density of whole log depth are shown in **Figure 2** (a, b, c). The best estimated frame moduli for whole depth from (V_P, V_S, ρ) are given in **Figure 2** (d, e). It is worth to mention that when only invert (K_d, G_d), the (V_P, V_S, ρ) inputs provide the most stable estimation which reveal to be consistent with the estimated values from the geological study by Lindeberg (2013). In addition, the use of shear wave information is crucial for drained moduli inversion, especially for estimating the shear frame modulus. The estimation of these rock frame properties aims at forming the basis for CO_2 saturation estimation that will be done based on FWI results in a near future.
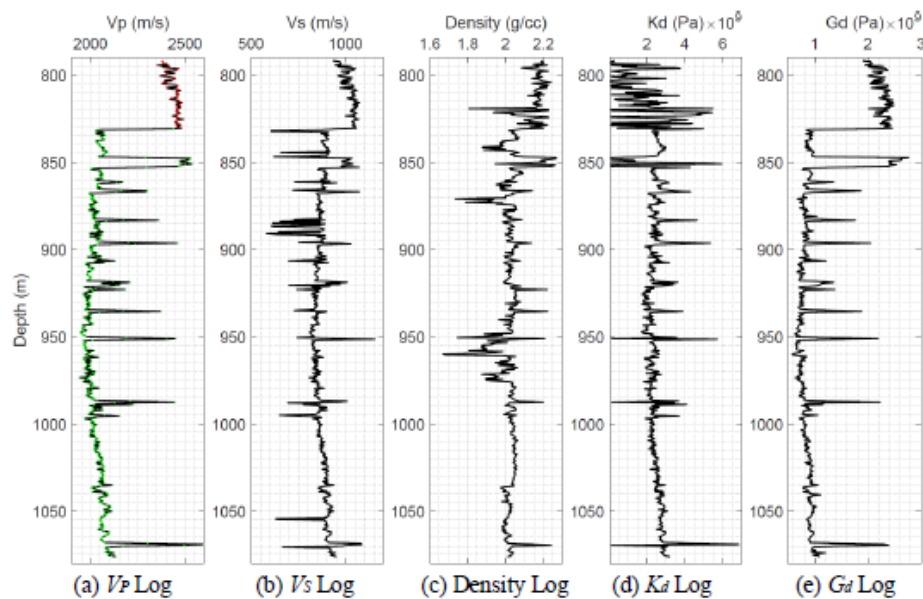

(a) V_P Log (b) V_S Log (c) Density Log (d) K_d Log (e) G_d Log

Figure 2 V_P, V_S and density responses from the Well 15/9-16 (left). The drained bulk and shear moduli (right), which are derived by V_P, V_S and density. V_S is derived using Vernik's relations.

Conclusions

We demonstrate the use of rock physics inversion for estimating CO_2 saturation and rock frame properties at Sleipner CO_2 storage site in the North Sea. We model the effect of various CO_2 saturations on viscoelastic properties of the Sleipner sediments based on the effective fluid phase plugged into the Biot theory. By analysis of the sensitivity tests, we can conclude that CO_2 saturation can be well estimated from only V_P input, especially for high brine saturation condition. The quality factor of P-wave or the S-wave velocity helps for the estimation of CO_2 saturation and for reducing the uncertainties. The CO_2 saturation can be well estimated when enough input data are provided to the inversion process. Using well log data, the S-wave velocities are coupled using empirical relations with the P-wave velocities and density from well log to estimate the rock frame moduli before CO_2 injection at the Utsira sand formation.

Acknowledgements

References

ARTS, R., CHADWICK, A., EIKEN, O., THIBEAU, S. & NOONER, S. 2008. Ten years' experience of monitoring CO2 injection in the Utsira Sand at Sleipner, offshore Norway. *First break,* 26.

ARTS, R., EIKEN, O., CHADWICK, A., ZWEIGEL, P., VAN DER MEER, L. & ZINSZNER, B. 2004. Monitoring of CO 2 injected at Sleipner using time-lapse seismic data. *Energy,* 29, 1383-1392.

BRIE, A., PAMPURI, F., MARSALA, A. & MEAZZA, O. Shear sonic interpretation in gas-bearing sands. SPE Annual Technical Conference and Exhibition, 1995. Society of Petroleum Engineers.

CARCIONE, J. M., PICOTTI, S., GEI, D. & ROSSI, G. 2006. Physics and seismic modeling for monitoring CO2 storage. *Pure and Applied Geophysics,* 163, 175-207.

CASTAGNA, J. P., BATZLE, M. L. & EASTWOOD, R. L. 1985. Relationships between compressional-wave and shear-wave velocities in clastic silicate rocks. *Geophysics,* 50, 571-581.

DUPUY, B., GARAMBOIS, S., ASNAASHARI, A., BALHARETH, H. M., LANDRØ, M., STOVAS, A. & VIRIEUX, J. 2016a. Estimation of rock physics properties from seismic attributes — Part 2: Applications. *GEOPHYSICS,* 81, M55-M69.

DUPUY, B., GARAMBOIS, S. & VIRIEUX, J. 2016b. Estimation of rock physics properties from seismic attributes — Part 1: Strategy and sensitivity analysis. *GEOPHYSICS,* 81, M35-M53.

FURRE, A. K., KIÆR, A. & EIKEN, O. 2015. CO2-induced seismic time shifts at Sleipner. *Interpretation,* 3, SS23-SS35.

FURRE, A. K. & EIKEN, O. 2014. Dual sensor streamer technology used in Sleipner CO2 injection monitoring. *Geophysical Prospecting,* 62, 1075-1088.

LANDRØ, M. 2001. Discrimination between pressure and fluid saturation changes from time-lapse seismic data. *Geophysics,* 66, 836-844.

LINDEBERG, E. 2013. *In:* CALCULATION OF THERMODYNAMIC PROPERTIES OF CO2, C., H2O AND THEIR MIXTURES ALSO INCLUDING SALT WITH THE EXCEL MACRO "CO2 THERMODYNAMICS". (ed.). Trondheim: SINTEF.

MAVKO, G., MUKERJI, T. & DVORKIN, J. 2009. *The rock physics handbook: Tools for seismic analysis of porous media,* Cambridge university press.

PRIDE, S. 2005. *Hydrogeophysics: Water Science and Technology Library: Springer.*

TEJA, A. & RICE, P. 1981. Generalized corresponding states method for the viscosities of liquid mixtures. *Industrial & Engineering Chemistry Fundamentals,* 20, 77-81.

ZWEIGEL, P. 2000. Reservoir geology of the storage unit in the Sleipner CO2-injection case. Trondheim, Norway: SINTEF.

Rock physics inversion for CO_2 injection at Sleipner

Rock physics inversion for CO_2 injection at Sleipner

Hong Yan [a,b], Bastien Dupuy [b], Anouar Romdhane [b], Børge Arntsen [a]

[a] *Department of Petroleum Engineering and Applied Geophysics, NTNU;* [b] *SINTEF Petroleum Research*
Contact email: hongy@stud.ntnu.no; bastien.dupuy@sintef.no

Introduction

Various geophysical techniques are used prior to and during the CO_2 injection process to characterize the changes in the subsurface properties. Several methods (for example, imaging and tomographic methods, amplitude versus offset analysis) are used to quantify the effect of CO_2 injection on seismic properties. In this context, the high-resolution results provided by full-wave inversion (FWI) (Virieux and Operto, 2009) can be very useful to derive rock physics properties. In our work, we use a rock physics tool with similar two-step workflow as described by Dupuy et al. (2016) to characterize selected rock physics properties of the Sleipner CO_2 storage pilot.

Methods

We use rock physics inversion based on Biot-Gassmann theory (Pride, 2005) for the Sleipner baseline well data. This extended Biot theory allows describing the porous sandstone saturated with brine (before injection) and partially saturated with brine and CO_2 (after injection). The rock physics tool allows computing viscoelastic properties from the poroelastic properties (rock and fluid phases). We use the Neighborhood Algorithm (Sambridge, 1999) to solve the inverse problem. This method is searching for the global minimum over the whole model space domain. The discrepancy between observed data (viscoelastic properties derived from input data) and calculated data (viscoelastic data computed from the rock physics properties by forward modeling) is described by a misfit function following the L2 norm.

Results

The log data from Well 15/9-16 before the CO_2 injection is used. We compute empirically S-wave sonic velocity using the empirical Vernik's relation (Mavko et al., 2009). We carry out the estimation of dry bulk and shear frame moduli (K_d and G_d) and the inversion is applied to the whole log data (Figure 1). The combination of P- and S- wave velocities and density (V_P, V_S, ρ) inputs provide the most stable estimation, which appears to be consistent with the estimated values from the geological study of Lindeberg (2013). Sensitivity tests under different CO_2 saturated conditions are performed in order to figure out how the CO_2 saturation and properties can be estimated from results provided from FWI. A priori parameters are defined based on existing studies on Sleipner. The sensitivity tests show that brine saturation S_W is better estimated when more than only P-wave velocity data is provided, but using only P-wave velocity is sufficient to get reliable results. The combination of V_P, V_S and ρ input make the

estimation more accurate. In addition, other sensitivity tests have been carried out in less optimal cases (if the rock physics model is not perfectly known and if the CO_2 properties are not defined) and suggest that the use of additional input data, especially S- wave velocity and P-wave quality factor are required to get a good estimation of CO_2 saturation.
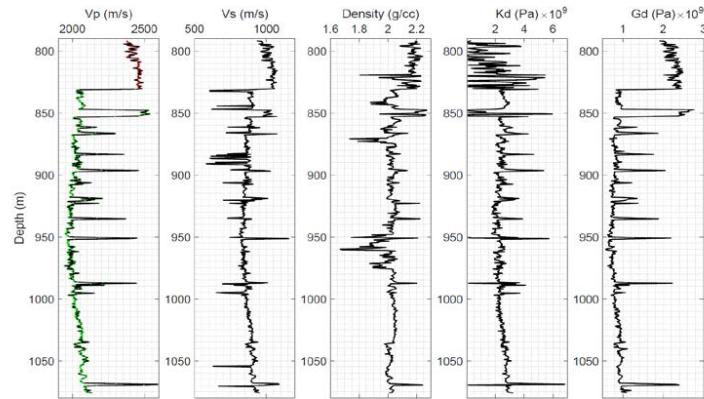

Figure 1: V_P, V_S and density responses from the Well 15/9-16 (3 left panels). Dry bulk and shear moduli (2 right panels), which are derived by rock physics inversion.

Conclusions

We demonstrate the use of rock physics inversion for estimating CO_2 saturation and rock frame properties at Sleipner CO_2 storage site in the North Sea. We model the effect of various CO_2 saturations on viscoelastic properties of the Sleipner sediments. The CO_2 saturation can be well estimated when enough input data is provided. Using well log data, the S-wave velocities are coupled using empirical relations with the P-wave velocities and density from well log to estimate the rock frame moduli before CO_2 injection at the Utsira sand formation.

Acknowledgements

References

Dupuy, B., Garambois, S., & Virieux, J. (2016). Estimation of rock physics properties from seismic attributes— Part 1: Strategy and sensitivity analysis. Geophysics, 81(3); pp. 35-53.
Pride, S. (2005). Hydrogeophysics: Water science and technology library.
Sambridge, M. (1999). Geophysical inversion with a neighbourhood algorithm—II. Appraising the ensemble. Geophysical Journal International, 138(3); pp. 727-746.
Virieux, J., & Operto, S. (2009). An overview of full-waveform inversion in exploration geophysics. Geophysics, 74(6); pp. 1-26.